國立臺灣大學工學院化學工程學系

碩士論文

Department of Chemical Engineering

College of Engineering

National Taiwan University

Master’s Thesis

有機長效及室溫磷光材料開發與浮閘式光電晶體元件應用

Development of the Organic Long-Persistent and Room-Temperature Phosphorescent Materials for Floating-Gate Phototransistor Devices.

黃品瑄

Pin-Hsuan Huang

指導教授：陳文章　博士

Advisor: Wen-Chang Chen, Ph.D.

中華民國 114 年 8 月

August, 2025

doi:10.6342/NTU202503178

國立臺灣大學碩士學位論文
口試委員會審定書
MASTER'S THESIS ACCEPTANCE CERTIFICATE
NATIONAL TAIWAN UNIVERSITY

有機長效室溫磷光材料開發與浮閘式光電晶體元件應用

Development of the Organic Long-Persistent and Room-Temperature Phosphorescent Materials for Floating-Gate Phototransistor Devices.

本論文係 黃品瑄 R12524070 在國立臺灣大學化學工程所完成之碩士學位論文，於民國 114 年 7 月 14 日承下列考試委員審查通過及口試及格，特此證明。

The undersigned, appointed by the Graduate Institute of Chemical Engineering, National Taiwan University on 14 July 2025, have examined a Master's Thesis entitled above presented by Pin-Hsuan Huang (R12524070) candidate and hereby certify that it is worthy of acceptance.

口試委員 Oral examination committee:

陳文章 劉振良

（指導教授 Advisor）

羅承慈

系（所、學位學程）主管 Director: 廖英志

誌謝

一眨眼，碩士兩年即將結束，第一天來到光電高分子研究室的畫面依舊歷歷在目。首先，感謝陳文章教授這兩年來在學術上的指導，並且提供我們一個良好的實驗環境，也謝謝劉振良教授每周在開會上的指導，使我收益良多。再來，感謝林彥丞教授的遠端指導，總是花很多時間及心力與我們討論研究上的問題。最後，感謝所有口試委員在我的口試上的指教。

還記得在尋找指導教授時，第一個與我面談的教授就是陳文章教授，由於我對陳文章教授實驗室的研究內容很感興趣，並且與教授的面談過程能夠感受到教授對實驗室及學生的用心，因此在面談完的當天晚上就立即寄信懇請進入陳文章教授的研究室。在這兩年的研究路程上，真的非常感謝所有光電高分子研究室的所有成員，尤其是翁逸勳學長在研究上的寶貴建議，並且教會我許多東西。謝謝子玥學姊在我剛進到實驗室時教導我實驗上的手法，也謝謝上一屆的子玥學姊、夢筑學姊、劉瑜學姊、亞璇學姊、志偉學長、奕捷學長、振甫學長及以撒學長帶我融入大家，在研究上遇到難關時也時常給予我鼓勵。謝謝博士班的大家長威丞學長一路上帶領實驗室，您辛苦了。謝謝柏毅學長、秉叡學長以及祈安學姊的照顧。謝謝很有趣的學弟妹們，感謝喜劇演員的泓安及尹嘉帶給大家許多歡樂，謝謝正煸、奕伶、景惟、湘棉、竣聖、渝凱及德恩都很可愛。最後，感謝同一屆的戰友們，感謝最貼心的玉瓊、最搞笑的昕豪、最熱情的乃文、最會拍照的永騰以及最耐斯的羿妏，感謝你們陪我走過碩士的這兩年。

正如布萊德彼特在《F1》中所說：「We can’t win if we don’t try.」與「We do what everybody does, we lose.」不隨波逐流，勇於嘗試，才能走出屬於自己的路。

中文摘要

本研究以有機場效電晶體為基礎，探討純有機長效室溫磷光與有機長延遲發光材料於浮閘式光記憶體與突觸元件中的應用潛力。有機場效電晶體具有結構可調性、可溶液製程與柔性基板相容等優勢，為新世代非揮發性光控記憶元件的理想平台。然而，傳統記憶材料多受限於瞬時激發與快速復合機制，難以達到長時間記憶保持與低功耗光寫入功能，因此本研究嘗試導入具延遲激發態特性的發光材料，以突破現有技術瓶頸。

於第二章中，我們選用兩種無添加金屬之室溫磷光分子，3,3',4,4'-二苯基磺醯四羧酸二酐與 3,3′,4,4′-苯酮四甲酸二酐，分別與聚苯乙烯共混製成浮閘介電層，並搭配 p 型半導體五苯製備成三端浮閘式光記憶元件。此結構展現良好的光輔助寫入行為，在 265 奈米紫外光與正閘極電壓條件下可有效儲存電子，並展現高達 10^6 的開關電流比與超過 10,000 秒之穩定性。此外，此元件同時具備優異的光突觸可塑性，包括成對脈衝促進、脈衝數目依賴性可塑性、脈衝時序依賴性可塑性、脈衝頻率依賴性可塑性與脈衝強度依賴性可塑性等突觸行為，進一步模擬類神經網路辨識手寫數字，顯示其於人工感知與學習系統中之應用潛力。

於第三章中，我們進一步探討以聚甲基丙烯酸甲酯為主體基質、並摻入四苯基聯苯胺、雙(1-萘基)-雙(苯基)聯苯胺或 2,7-雙(1-萘基苯胺)-9,9-二甲基芴作為客體之有機長延遲發光系統。藉由調控客體濃度與能階設計，達成可見長效餘暉與顯著的電荷儲存效應。結果顯示，5 重量百分比的 2,7-雙(1-萘基苯胺)-9,9-二甲基芴元件展現最佳表現，開關電流比高達 4.9×10^5，並具備 10,000 秒以上之穩定性。然而，其載子狀態高度穩定亦造成抹除效率下降，顯示有機長延遲發光機制在提供長效儲存優勢的同時，也需解決其電性可逆性之挑戰。

綜合而言，本研究首次系統性驗證純有機長效室溫磷光與有機長延遲發光材料於有機場效電晶體光記憶元件中的應用潛力，成功結合激子工程與元件架構，實現高效率、可光寫入且具環境穩定性之非揮發性記憶系統。此結果為未來開發有機記憶技術提供具體的材料選擇與設計策略。

關鍵字：場效電晶體、影像辨識系統、光突觸、室溫磷光、有機長餘輝發光。

ABSTRACT

This thesis explores the integration of purely organic room-temperature phosphorescent (RTP) and organic long-persistent luminescent (OLPL) materials into organic field-effect transistor (OFET) platforms for high-performance floating-gate photomemory and synaptic devices. Owing to their structural tunability, solution-processability, and compatibility with flexible substrates, OFETs have emerged as promising candidates for non-volatile memory technologies. However, conventional OFET memory architectures often face limitations in data retention and optical programming efficiency due to the rapid recombination dynamics of typical charge storage materials. To address this, we introduce metal-free organic luminophores with long-lived excited states to enable energy-efficient and optically controllable memory operations.

In Chapter 2, we employ two metal-free RTP molecules, 3,3′, 4,4′-Diphenyl sulfone tetracarboxylic dianhydride and 3,3′, 4,4′-Benzophenone tetracarboxylic dianhydride, which are blended with polystyrene to form the floating-gate dielectric layer. Integrated with the p-type semiconductor pentacene, the resulting OFET memory devices demonstrated robust photo-assisted electrical writing under 265 nm UV light, achieving a high $I_{\mathrm{ON}}/I_{\mathrm{OFF}}$ of ~10^6 and stable data retention exceeding 10,000 seconds. These RTP-based devices also exhibited excellent synaptic plasticity, including paired-pulse facilitation, pike-number-dependent plasticity, spike-timing-dependent plasticity, spike-rate-dependent plasticity, and spike-intensity-dependent plasticity, and were further validated in a neural network simulation for handwritten digit recognition, highlighting their potential for neuromorphic applications.

Chapter 3 extends the study to OLPL-based systems using poly(methyl methacrylate)

doi:10.6342/NTU202503178

as the host matrix and N,N, N′,N′-Tetraphenylbenzidine, N, N′-Bis(naphthalen-1-yl)-N, N'-bis(phenyl)-benzidine, or 2,7-Bis(N-(1-naphthyl)aniline)-9,9-dimethylfluorene (DMFL-NPB) as guest molecules. By optimizing energy level design and guest concentration, we achieved visible persistent luminescence and stable charge trapping behavior. Among all systems, the device incorporating 5 wt% DMFL-NPB showed the most pronounced performance, an $I_{\mathrm{ON}}/I_{\mathrm{OFF}}$ ratio of 4.9×10^5, and excellent retention over 10,000 seconds. However, due to the strong stabilization of trapped charges, the erase operation remained incomplete, revealing a trade-off between long-term retention and rewritability.

In summary, this work presents a systematic demonstration of RTP and OLPL materials in OFET-based memory architectures, offering new strategies for exciton engineering and optoelectronic device design. These findings establish a pathway toward the development of purely organic, light-controllable, and flexible memory technologies.

Keywords: field-effect transistors, image recognition systems, photosynapses, room-temperature phosphorescence, organic long-persistent luminescent.

CONTENTS

doi:10.6342/NTU202503178

doi:10.6342/NTU202503178

LIST OF TABLES

LIST OF FIGURES

doi:10.6342/NTU202503178

doi:10.6342/NTU202503178

Chapter 1 Introduction

1.1 Introduction of Organic Field-Effect Transistors (OFETs)

The remarkable tunability of molecular structures in organic optoelectronic materials has enabled the development of systems with diverse and highly desirable physical and electronic properties. These include efficient photoluminescence, adjustable charge carrier mobility, high photovoltaic conversion efficiency, thermoelectric performance, and even superconductivity under specific conditions.[1] In addition to these versatile functionalities, organic semiconductors offer significant processability advantages, particularly in their compatibility with low-temperature and low-cost solution-based techniques such as spin-coating and blade-coating. This makes them particularly suitable for integration onto flexible substrates and for large-area fabrication. As a result, organic optoelectronic materials have found widespread application in various device platforms. Representative applications of organic optoelectronic materials include organic light-emitting diodes (OLEDs), which have become a mainstream display technology in consumer electronics due to their high brightness, transparency, color saturation, and mechanical flexibility. The development of OLED displays has progressed through three generations of emissive materials—fluorescent, phosphorescent, and thermally activated delayed fluorescence (TADF)—each contributing to enhanced efficiency and performance.[1] Another notable application is organic solar cells (OSCs), which have attracted significant attention in the field of renewable energy due to their advantages such as low cost, lightweight nature and semi-transparency.[1] In addition, organic field-effect transistors (OFETs) exhibit considerable technological appeal as potential switching elements in a wide range of electronic and optoelectronic devices.

doi:10.6342/NTU202503178

Since their initial development in the 1980s, the performance of OFETs has seen substantial improvements owing to a deeper understanding of charge injection mechanisms, dielectric interfaces, and molecular packing structures. As a result, OFETs are emerging as promising next-generation three-terminal components, particularly in recent advances related to non-volatile memory and artificial synapse applications.[1] Structurally, OFETs comprise an organic semiconductor layer, insulating layer, and source/drain/gate electrodes, and can be categorized into four typical device configurations: bottom-gate bottom-contact (BGBC), bottom-gate top-contact (BGTC), top-gate bottom-contact (TGBC), and top-gate top-contact (TGTC), as shown in **Figure 1.1**.[1] Different OFET architectures exhibit distinct advantages depending on their structural configuration. The BGBC design facilitates rapid screening of novel semiconductor materials, as the gate, dielectric, and source/drain electrodes can be fabricated in advance, with the semiconductor deposited in the final step. This approach preserves a pristine semiconductor/dielectric interface; however, the exposed nature of the semiconductor renders it vulnerable to environmental degradation from moisture and oxygen. In contrast, top-gate configurations such as TGBC and top-gate top-contact TGTC offer improved environmental stability, as the top dielectric layer can serve as an encapsulation barrier. Nonetheless, careful optimization of dielectric deposition conditions is essential to avoid damaging the underlying organic layers.[1]

Owing to their tunable device architecture, OFETs have garnered increasing attention in a wide range of optoelectronic applications, particularly in the fields of non-volatile memory and artificial synapses. Non-volatile memory enables long-term data retention without the need for continuous power supply, and features advantages such as high on/off current ratios, excellent endurance, and nondestructive readout capability. Meanwhile, artificial synapses can emulate various biological neuronal behaviors, demonstrating great potential for the realization of neuromorphic vision systems and integrated optoelectronic processors, thereby offering forward-looking solutions for future neuromorphic computing platforms.

1.1.1 Working Principles of OFETs

The operation mechanism of an OFET can be divided into three distinct regions based on the relative magnitude of the drain voltage (V_d) and gate voltage (V_g). as illustrated in **Figure 1.2**. When $V_d \ll V_g - V_{th}$ (where V_g is the threshold voltage), the device operates in the linear region, where the carrier concentration exhibits a linear gradient along the channel and the drain current (I_d) increases linearly with V_d. As V_d approaches $V_g - V_{th}$, the conductive channel is pinched off at the drain end, marking the transition into the saturation region. In the saturation region ($V_d > V_g - V_{th}$), the effective channel length becomes constant, and I_d reaches a saturation value, primarily limited by carrier transport and trapping effects.[8]

OFETs can be classified as either p-type or n-type based on the dominant charge carrier. P-type devices operate by applying a negative gate voltage to induce a hole-conducting channel, exhibiting relatively stable conductivity and thus being widely adopted in practical applications. In contrast, n-type devices require a positive gate voltage to induce an electron-conducting channel; however, their operational stability is often compromised due to the susceptibility of electrons to trap states and degradation from environmental oxygen and moisture. Therefore, the development of n-type organic semiconductors must address both charge carrier mobility and long-term stability to ensure reliable device performance.[9]

The electrical performance of OFETs is usually analyzed through analysis of output and transfer characteristics. As shown in **Figure 1.3a**, the output characteristics illustrate the behavior of the I_d as a function of V_d under various V_g, showing a linear increase in I_d at low V_d (linear regime), followed by saturation at higher V_d for each given V_g. In contrast, the transfer characteristics are obtained under a fixed V_d in the saturation regime, and depict the dependence of I_d on V_g. As V_g increases, the field-induced carrier accumulation is enhanced, resulting in a higher I_d, as shown in **Figure 1.3b**. The transfer characteristics serve as a basis for analyzing key parameters such as field-effect mobility (μ), V_{th}, on/off current ratios (I_{ON}/I_{OFF}), and subthreshold swing (*SS*). Specifically, μ reflects the carrier transport efficiency within the channel and is commonly evaluated from the saturation regime using the corresponding current-voltage relationship. V_{th} represents the minimum gate voltage required to turn the device on. I_{ON}/I_{OFF} denote the current contrast between the on and off states, which is critical for memory and logic applications. *SS* characterizes the gate voltage range necessary to transition the device from the off to the on state, closely associated with the density of interface trap states.[10, 11]

1.1.2 Working Mechanism of Transistor Memory Devices

OFETs, as non-volatile memory devices, have been widely applied in electronic displays, sensors, and memory devices. The fundamental structure of an OFET-based memory device, as illustrated in **Figure 1.4a**, a polymer electret layer is introduced between the organic semiconductor and the control gate dielectric layer to enable charge storage functionality. When an OFET operates as a memory device, its memory performance—particularly the memory window (ΔV_{th})—is a critical parameter for evaluating its functionality. ΔV_{th} is defined as the shift in threshold voltage after programming (PGM) and erasing (ERS) operations, which is directly related to the charge trapping and release capabilities of the storage layer. **Figure 1.4b** illustrates the programming and erasing processes of a p-type OFET memory. During programming, a

doi:10.6342/NTU202503178

negative gate voltage induces hole injection from the source into the channel, where they are subsequently trapped in the charge storage layer, resulting in a positive shift in V_{th}. In this process, charge accumulation in the floating gate enhances the carrier concentration in the channel, leading to an increase in threshold voltage. Conversely, applying an erasing voltage releases the trapped holes, returning the device to its initial state and restoring V_{th} to its pre-programmed value.[12] This reversible programming and erasing mechanism makes OFETs promising candidates for memory applications. Furthermore, the magnitude of ΔV_{th} reflects not only the charge trapping efficiency of the storage layer but also the overall memory performance. A larger ΔV_{th} indicates higher charge retention capability and more stable memory behavior.

In addition to the ΔV_{th}, the practical performance of memory devices must be comprehensively evaluated through additional parameters, including the $I_{\mathrm{ON}}/I_{\mathrm{OFF}}$, retention, and endurance. The $I_{\mathrm{ON}}/I_{\mathrm{OFF}}$, defined as the ratio between the "on" state (high I_{d}) and "off" state (low I_{d}), reflects the current contrast between different memory states. For a high-performance non-volatile memory device, it is essential that the output current values remain stable over extended periods following the programming and erasing operations, as evaluated by retention tests, as illustrated in **Figure 1.4c**. This retention capability can be quantified through data preservation tests lasting over 10^4 seconds, demonstrating the device's ability to maintain its stored state over time. Endurance is typically assessed by repeatedly performing write–read–erase–read (WRER) cycles, as shown in **Figure 1.4d**, to verify the operational stability and fatigue resistance of the device under repeated use.[12, 13]

In summary, the electrical performance and stability of OFET memory devices must be comprehensively evaluated through multiple key parameters. A thorough understanding of these characteristics enables progressive refinement of device

doi:10.6342/NTU202503178

architecture and material composition, thereby establishing a robust platform for the development of high-performance, durable, and practically applicable organic memory technologies.

1.1.3 Operational Principles of Synaptic Transistors

In recent years, the explosive growth of data and the rapid advancement of artificial intelligence (AI) technologies have exposed the performance and energy-efficiency limitations of the traditional von Neumann architecture. To enable more efficient parallel computation and real-time learning capabilities, neuromorphic computing has emerged as a promising new paradigm by mimicking the signal transmission and plasticity mechanisms of biological synapses and neurons. Recent studies have demonstrated that organic synaptic transistors (OSTs), owing to their low-cost fabrication, excellent flexibility, and tunable material properties, hold great potential for integration into artificial neural networks (ANNs), thereby enabling the development of energy-efficient and adaptive neuromorphic computing platforms.[14]

Artificial synaptic transistors can generally be categorized into two-terminal and three-terminal architectures based on their structural configurations. Two-terminal synaptic devices, typically based on memristive or resistive switching mechanisms, offer advantages such as simple structure, small footprint, and ease of integration. They emulate synaptic plasticity through the modulation of conductance via applied voltage pulses. However, the shared read-write pathway in two-terminal devices often leads to signal interference and unintended programming, compromising device stability and accuracy. In contrast, three-terminal architectures allow for the decoupling of signal transmission and weight modulation, enabling concurrent learning and processing while minimizing crosstalk between pre- and post-synaptic signals. As a result, OSTs, which adopt a three-terminal structure, have increasingly replaced two-terminal devices in recent research.[14] In these systems, the gate terminal functions analogously to a pre-synaptic neuron, while the source and drain correspond to the post-synaptic neuron, facilitating simultaneous signal processing and transmission. In biological synapses, the arrival of an action potential at the pre-synaptic terminal triggers neurotransmitter release, which binds to receptors at the post-synaptic side and induces a change in current. Similarly, in OSTs, the conductivity of the channel is modulated by the gate voltage, resulting in a drain current that mimics excitatory post-synaptic current (EPSC) or inhibitory post-synaptic currents (IPSC).[15]

Moreover, such devices can replicate various forms of synaptic plasticity, including short-term plasticity (STP) and long-term plasticity (LTP). STP represents transient changes in synaptic strength on the millisecond to second timescale, often evaluated using paired-pulse facilitation (PPF), where two closely spaced voltage pulses induce an enhanced second response, simulating short-term memory behavior. In contrast, LTP involves persistent synaptic strengthening induced by prolonged or repetitive stimulation, corresponding to long-term memory formation. The transition between STP and LTP is highly dependent on parameters such as pulse frequency, amplitude, duration, and number. By precisely tuning these parameters, various pulse-dependent plasticity behaviors can be achieved, including spike-number-dependent plasticity (SNDP), spike-timing-dependent plasticity (STDP), spike-rate-dependent plasticity (SRDP), and spike-intensity-dependent plasticity (SIDP). These phenomena emulate the complex stimulus-response and memory modulation capabilities of biological neural systems, underscoring the potential of artificial synaptic devices for implementing learning and memory functions in neuromorphic computing systems.[16, 17] Building upon these capabilities, future applications may include the emulation of complex sensory neural networks such as those found in human visual and auditory systems, thereby expanding the scope of intelligent technologies in perception and cognition.

1.1.4 Development of Phototransistor Memory Materials

With the increasing demand for optically controlled nonvolatile memory, phototransistor memory devices have emerged as a promising next-generation memory technology due to their advantages of low power consumption, high addressability, and light-programmable capability. Their memory behavior mainly relies on the ability of the photoresponsive charge-trapping layer to absorb light energy, convert it into excitons or carriers, and stably store the resulting charges. Based on the different photoexcitation responses of the active materials, current research in phototransistor memory can be generally categorized into three major types: strongly light-absorbing organic dyes, highly emissive materials, and materials capable of generating long-lived photoexcited states. These materials exhibit distinct memory mechanisms and application potential.

Strongly absorbing organic dyes, due to their large optical cross-sections and reversible structural features, were among the earliest materials used in light-programmable memory devices. Representative examples include azobenzene, spiropyran, and conjugated molecules with donor–acceptor (D–A) structures. These molecules can undergo photoinduced isomerization or intramolecular charge transfer under ultraviolet or visible light, thereby modulating the threshold voltage of the semiconductor channel. However, dye-based materials tend to suffer from photobleaching under prolonged illumination and show poor environmental stability in the presence of oxygen and moisture, which limits their data retention and cycling endurance.

To overcome the stability limitations of organic dyes, many researchers have turned

doi:10.6342/NTU202503178

to highly emissive materials with efficient photoelectric conversion. Among them, hybrid organic–inorganic perovskites have attracted significant attention due to their high absorption coefficients, long carrier diffusion lengths, and excellent photoluminescence properties. In recent years, they have been widely used in optoelectronic sensors and memory devices. However, perovskite materials are highly sensitive to humidity and heat, and the presence of toxic lead compounds raises environmental and health concerns for practical applications.

In recent years, photoactive materials with long exciton lifetimes have emerged as another research focus for phototransistor memory development. These materials can effectively extend the lifetime of the excited state and improve charge separation and trapping efficiency, leading to more stable optical programming. Triplet–triplet annihilation upconversion (TTA-UC) is one such mechanism, in which two triplet excitons combine to produce delayed fluorescence, which can further trigger charge trapping or channel conductivity modulation. Another long-lived exciton generation mechanism is singlet fission (SF), which splits a high-energy singlet exciton into two triplet excitons, effectively increasing the number of photogenerated carriers and enhancing writing efficiency. Additionally, room-temperature phosphorescence (RTP) materials can generate long-lived excited states through intramolecular spin–orbit coupling and proper energy-level alignment, thereby improving the photoresponse and operational stability of the memory device.

In summary, organic dye materials offer diverse structures and tunable molecular design, but suffer from limited stability and data retention. Perovskite materials provide excellent photoelectric conversion and low programming voltage, yet still face challenges in long-term stability and toxicity. In contrast, materials capable of generating long-lived excitons can achieve both memory stability and high light-writing sensitivity, offering

doi:10.6342/NTU202503178

greater potential for the future development of phototransistor memory technologies.

1.2 Advancing Charge Trapping Materials for Transistor Memory Devices

Memory devices play a critical role in modern electronic systems, supporting information storage and processing in a wide range of applications—from personal devices such as smartphones and laptops to cloud servers and large-scale data storage systems. As storage technologies continue to evolve toward higher density, lower power consumption, faster read/write speeds, and long-term data retention, non-volatile memories have gained increasing attention and become a key focus in the development of advanced memory components. Among various emerging non-volatile memory technologies, transistor-based memories that utilize electric field control and charge storage mechanisms have demonstrated advantages such as mechanical flexibility, low operating voltage, and high integration potential. In particular, with the rapid advancement of organic electronics, OFET memory has attracted significant interest due to its simple structure, ease of fabrication, and excellent rewritability.[18] Based on the physical characteristics and charge trapping mechanisms of the charge storage layer, OFET memories can generally be categorized into three main types: polymer electret, ferroelectric, and floating gate systems.

1.2.1 Polymer Electret

Polymer electrets have recently emerged as promising charge storage materials for OFET memory devices. These materials are insulating dielectrics capable of maintaining quasi-permanent charges over extended periods and have been widely applied in sensors and memory components. The charge storage behavior of polymer electrets is generally attributed to two primary mechanisms: the orientation of permanent dipoles in polar materials and charge trapping at structural defects or interfacial trap sites.[19] Among various electret candidates, styrene-based polymers have attracted considerable attention due to their favorable tunability in both physical and chemical properties. Kim et al. systematically investigated three categories of styrene-derived polymer electrets, including non-polar and hydrophobic materials such as polystyrene (PS), poly(2-vinyl naphthalene) (PVN), poly(α-methylstyrene) (PαMS), and poly(4-methylstyrene) (P4MS); moderately polar and hydrophilic materials such as poly(4-vinylphenol) (PVP) and poly(2-vinylpyridine) (PVPyr); and highly polar and hydrophilic polyvinyl alcohol (PVA). The study revealed that memory devices employing non-polar, hydrophobic polymer electrets exhibited more pronounced V_{th} shifts and superior charge retention, outperforming devices with polar and hydrophilic counterparts. This improvement is attributed to the ability of hydrophobic electret layers to effectively retain charges injected from the pentacene semiconductor under gate bias, while minimizing charge dissipation through dipole relaxation, moisture absorption, and ion conduction pathways.[20]

In recent years, polymer electret devices with ambipolar memory capability have also been developed, allowing the storage of both electrons and holes simultaneously. This expands the memory window and enables multi-level data storage. For example, introducing triphenylamine (TPA) functional groups into polymer matrices such as polyimide (PI), polyester (PET), or polyether (PE) can effectively tune the trap energy levels to achieve either ambipolar or unipolar charge storage behavior. However, most polymer electret memory devices still suffer from the issue of high operating voltage, mainly due to the relatively thick dielectric layers. Therefore, one of the key directions for future research is the development of thinner and more efficient electret materials to enable low-power and highly stable OFET memory technologies.[21]

1.2.2 Ferroelectric

With data storage technologies approaching the physical limitations of Moore's law, the development of low-power, high-density, and non-volatile memory devices has become a key challenge in modern electronics. In this context**,** Ferroelectric Organic Field-Effect Transistors (FeOFETs) have emerged as a promising memory architecture in organic electronics due to their low operating voltage, fast switching speed, non-destructive readout, and excellent data retention. FeOFETs are three-terminal devices characterized by a gate insulator composed of ferroelectric materials with spontaneous polarization. By applying a gate voltage, the polarization direction within the ferroelectric film can be switched between two stable states, thereby modulating the charge carrier density in the channel to represent logic states "0" and "1." Unlike traditional floating gate memories that require high voltages to inject charges, FeOFETs can achieve data writing and erasing through polarization switching, and read operations can be performed non-destructively via the drain current. This greatly enhances device efficiency and extends operational lifetime.[21]

The study of ferroelectricity dates back to the discovery of Rochelle salt in 1921, which demonstrated early potential for memory applications.[22] With advances in materials engineering and device design, researchers have incorporated ferroelectric materials into field-effect transistor structures to enable non-volatile memory functions.[23] For instance, the use of organic ferroelectric polymers such as polyvinylidene fluoride (PVDF) and its copolymer P(VDF-TrFE) enables the integration of ferroelectric properties with flexible, low-cost, and large-area processing.[18] More recently, research has explored ferroelectric terpolymers such as P(VDF-TrFE-CTFE), which provide bistable polarization suitable for multi-level storage. Wang et al. combined this material with the organic semiconductor pentacene to develop a multi-level FeOFET device featuring four distinct conductance states. By adjusting the gate pulse voltages (e.g., 40, −20, −30, −40 V), different storage states (00, 01, 10, 11) can be achieved, demonstrating the potential of FeOFETs for analog and multi-bit storage in neuromorphic computing and high-density memory applications.[24]

Despite the advantages of ferroelectric materials in terms of fast switching and stable polarization, scaling down the ferroelectric film thickness introduces significant challenges. One of the major issues is the depolarization effect, which reduces the memory window and data retention capability. Additionally, the polarization stability is often affected by interface defects between the ferroelectric and semiconductor layers, or by charge trapping within the material, leading to degraded switching ratios and weaker non-volatile performance. To address these challenges, several strategies have been proposed. For example blending ferroelectric polymers with non-ferroelectric materials such as poly(methyl methacrylate) (PMMA) to create flat, dense films that retain polarization functionality.[23] Such approaches help improve retention time and enhance device stability.

In summary, FeOFET memory devices integrate the reversible polarization of ferroelectric materials with the flexibility and low cost of organic semiconductors, offering promising non-volatile storage capabilities. However, to enable practical applications, further improvements are needed to address interfacial stability and the reliability of multi-level data storage.

doi:10.6342/NTU202503178

1.2.3 Floating Gate

Floating-gate memory is a type of nonvolatile memory structure commonly used in OFETs. Its memory function is based on the ability of the floating gate layer to trap charges. Compared to conventional transistors, floating-gate transistors include a suspended conductive layer located between the gate electrode and the channel. During programming or erasing operations, charge carriers (electrons or holes) are injected into the floating gate through tunneling across a thin dielectric layer and become trapped. These stored charges shift the threshold voltage required to turn on the channel, allowing the device to maintain different conductive states even without an external power supply, thereby achieving nonvolatile memory behavior.[18, 21]

In traditional fabrication processes, the floating gate and tunnel dielectric layers are usually prepared in two separate steps, which involve the deposition of metal nanoparticles or nanocrystals followed by spin-coating or vapor deposition of an insulating layer. This method is not only complex but also requires the use of orthogonal solvents to avoid damaging the floating gate layer. As a result, it often causes inconsistent device performance and interfacial defects, making it unsuitable for large-area manufacturing and industrial applications. To address these issues, recent studies have introduced the concept of a "floating-gate electret," where the floating gate material is blended with a polymer dielectric and deposited using a single spin-coating step, greatly simplifying the fabrication process. This hybrid electret approach eliminates the need for a separate tunnel layer and removes the requirement for orthogonal solvents. Furthermore, its compatibility with solution processing makes it highly promising for use in emerging areas such as flexible electronics and neuromorphic computing.[25]

Based on the properties of the floating-gate materials and their memory behavior, organic floating-gate memory devices can be roughly classified into the following

doi:10.6342/NTU202503178

categories: (1) Metal nanoparticle-based: Materials such as Au, Ag, and Pt are commonly used as floating gates due to their stable conductivity and ability to provide a wide memory window.[19] (2) Polymer-based floating gates: Conductive polymers like poly(3-hexylthiophene) (P3HT) and poly(N-vinylcarbazole) (PVK) are often used. These materials are solution-processable and can form compatible structures with polymer insulators.[19, 25] (3) Nanocrystal-based floating gates: Nanomaterials such as CdSe or ZnO are employed as charge-trapping layers, offering excellent bipolar charge trapping capability and high memory density.[21, 26] (4) Hybrid electret structures: These are formed by blending nanoparticles or conductive polymers with insulating polymers, combining good processability with improved stability. The memory layer can be fabricated in a single spin-coating step.[25] (5) Ferroelectric polymer-based floating gates: Materials like poly(vinylidene fluoride-co-trifluoroethylene) (PVDF-TrFE) provide spontaneous polarization fields that help stabilize stored charges.[19, 27]

In the future, floating-gate electret systems demonstrate exceptional potential for realizing multi-level charge storage. Their development is rapidly advancing toward high integration and mechanical flexibility. Owing to their simplified fabrication and remarkable stability, these systems are poised to occupy a pivotal position in next-generation portable storage technologies, memory architectures for the Internet of Things (IoT), and high-performance smart sensing platforms. As such, they are expected to serve as a foundational framework driving the commercialization of flexible electronics and neuromorphic computing.

1.3 Introduction to Organic Delayed Exciton Emission

In the field of organic optoelectronic materials, the regulation of excited states plays

doi:10.6342/NTU202503178

a pivotal role in enhancing device performance. Beyond conventional fluorescence and phosphorescence, organic delayed exciton emission encompasses a class of photophysical processes in which photon emission occurs with a measurable delay following photoexcitation. Instead of emitting light immediately, excitons undergo additional energy conversion steps before radiative decay. Prompt fluorescence typically occurs within tens of nanoseconds, while delayed emission may last from microseconds to several hours, depending on the underlying mechanism. This delayed luminescence generally originates from long-lived excited states, most commonly triplet excitons, and has attracted considerable interest due to its potential to achieve high internal quantum efficiency (IQE).[28] In organic materials, however, the utilization of triplet excitons is intrinsically limited by spin-forbidden transitions, which restrict their direct contribution to light emission. Therefore, exploiting various delayed emission mechanisms to harness triplet exciton energy provides a promising strategy to overcome the Stokes efficiency limit and to develop high-performance, metal-free luminescent devices.

In recent years, various mechanisms of delayed exciton emission have been extensively investigated in purely organic systems, including thermally activated delayed fluorescence (TADF), triplet–triplet annihilation upconversion (TTA-UC), room-temperature phosphorescence (RTP), and organic long-persistent luminescence (OLPL). These mechanisms have not only deepened our understanding of exciton dynamics in organic materials but have also inspired new design strategies for the development of efficient, metal-free luminescent materials.

Organic delayed exciton emission materials, which are characterized by their metal-free composition, tunable emission lifetimes, and versatile exciton behaviors, have emerged as promising candidates for applications beyond traditional optoelectronics. In particular, they show considerable potential for integration into next-generation OFET

doi:10.6342/NTU202503178

memory devices and neuromorphic electronic systems. These emerging technologies rely on multi-level charge or exciton states to enable memory storage and signal processing. The intrinsic photophysical features of delayed emission, such as long-lived excited states and controllable energy-level transitions, provide a robust platform for dynamic information retention and neuromorphic functionality.[29] Unlike conventional phosphorescent materials that utilize heavy-metal atoms to enhance intersystem crossing (ISC), organic systems achieve delayed emission through tailored molecular design. Strategies such as donor–acceptor architectures and π-conjugated frameworks are commonly employed to modulate singlet–triplet interconversion efficiency and exciton lifetimes. This structural tunability significantly broadens their potential for application in light-responsive memory elements and neuromorphic circuitries.[30] Foundational theoretical and experimental insights into mechanisms such as TADF and RTP have been provided by key review articles, including those by Uoyama et al. in *Nature* (2012) [28] and Penfold et al. in *Chemical Reviews* (2018).[31] These studies have laid the scientific groundwork for the rational design and functional deployment of organic delayed emission materials in future electronic and optoelectronic technologies.

1.3.1 Thermally Activated Delayed Fluorescence (TADF)

TADF has emerged as a pivotal photophysical mechanism in the development of high-performance organic optoelectronic materials. Unlike conventional phosphorescence, which requires heavy-metal complexes to facilitate spin-orbit coupling for triplet exciton utilization, TADF enables the harvesting of both singlet and triplet excitons through purely organic molecular architectures. As shown in **Figure 1.5**, this is achieved via a thermally driven reverse intersystem crossing (RISC) process, in which the small energy gap (ΔE_{ST}) between the lowest excited singlet state (S_1) and triplet state

doi:10.6342/NTU202503178

(T_1) allows triplet excitons to be upconverted into emissive singlet states at room temperature, leading to delayed fluorescence. The theoretical IQE of TADF emitters can approach 100%, positioning them as key alternatives to metal-based phosphorescent materials in light-emitting applications.[32, 33]

TADF has fundamentally reshaped the field of OLEDs, enabling metal-free systems with near-unity IQE. The integration of TADF into OLEDs has significantly mitigated reliance on scarce and expensive heavy metals such as iridium and platinum, promoting more sustainable and environmentally friendly device architectures.[28, 33] Beyond OLEDs, TADF materials have recently attracted increasing attention for their potential use in OFETs, particularly in nonvolatile memory and light-emitting transistor applications. In OFET-based memory devices, TADF materials serve dual roles, functioning as both light emitters and charge modulation layers. Their unique exciton dynamics, characterized by long-lived triplet states and efficient RISC processes, enable optical programming and improved charge trapping behavior. TADF polymers embedded in the active layer or floating gate can enhance memory performance by expanding the memory window, prolonging retention time, and reducing operational voltage.[34, 35] For instance, π-conjugated heptazine derivatives and diphenylanthracene copolymers have demonstrated optically programmable switching and stable electrical bistability in transistor platforms.[35]

Moreover, the structural tunability of TADF emitters allows the optimization of highest occupied molecular orbital (HOMO)/lowest unoccupied molecular orbital (LUMO) separation and suppression of non-radiative decay, contributing to device stability and charge retention. Recent studies have also highlighted the benefits of integrating TADF materials in optoelectronic transistors, such as OLETs, where they support both charge transport and efficient emission.[34, 36] The ability to control exciton lifetimes and recombination pathways makes TADF materials particularly suitable for multifunctional OFETs that operate under low power and with high optical sensitivity.

Overall, TADF not only represents an efficient luminescence mechanism but also provides new strategies for designing multifunctional organic transistors. Its expanding application in OFET-based platforms demonstrates the versatility of TADF materials in bridging the gap between light emission and charge manipulation, which is essential for the advancement of next-generation optoelectronic systems.[35-37]

1.3.2 Triplet-Triplet Upconversion Annihilation (TTA-UC)

TTA-UC has emerged as a promising triplet management strategy in the field of organic photophysics and optoelectronic devices. This mechanism enables the conversion of two low-energy photons into a single higher-energy emission through a triplet fusion process, allowing efficient upconversion under low excitation intensities.[38] Most luminescent materials exhibit Stokes-shifted emission, in which a higher-energy photon is absorbed and subsequently re-emitted at a lower energy. In contrast, photon upconversion (UC) represents an anti-Stokes process, whereby two or more low-energy photons are converted into a single photon of higher energy. This energy-gaining mechanism allows upconverted emission to surpass the excitation photon energy, which is particularly advantageous in biological imaging, optoelectronics, and energy harvesting applications. In TTA-UC systems, this anti-Stokes shift is achieved through the cooperative interaction of triplet excitons within purely organic frameworks.[39] The process relies on two primary molecular components: a photosensitizer and an emitter. As shown in **Figure 1.6**, upon photoexcitation, the sensitizer absorbs a low-energy photon and transitions to its singlet excited state ($^1S^*$), followed by ISC to form a triplet state ($^3S^*$). This triplet energy is then transferred to the emitter through triplet–triplet energy

doi:10.6342/NTU202503178

transfer (TTET), exciting it to a triplet state ($^3E^*$). When two triplet-excited emitters encounter one another, they undergo triplet–triplet annihilation (TTA), resulting in one emitter returning to the ground state and the other being promoted to the singlet excited state ($^1E^*$), from which it radiatively decays to the ground state, releasing an upconverted photon (hv').[40] This mechanism enables TTA-UC to function under ambient conditions with relatively low excitation power, making it a metal-free, energy-efficient alternative to traditional upconversion techniques. The process has shown strong potential in various applications, including bioimaging, light harvesting, sensors, and more recently, organic optoelectronics.[38] A key advantage of TTA-UC is its compatibility with organic semiconductors and polymers, which has facilitated its integration into flexible and solution-processable device architectures. However, performance remains sensitive to factors such as triplet lifetime, oxygen quenching, and exciton diffusion, necessitating careful molecular and device engineering.[39]

In the context of OFETs, TTA-UC has opened new avenues for multifunctional device design. Particularly in memory devices, TTA-UC systems embedded in active layers or dielectric interfaces have been shown to improve photoresponse and charge storage capabilities. By exploiting the delayed exciton recombination dynamics intrinsic to TTA-UC, researchers have developed optically programmable OFET memory platforms with enhanced memory windows, prolonged retention time, and improved I_{on}/I_{off}.[41, 42] When upconverted singlet excitons are generated near the semiconductor–dielectric interface, they effectively modulate the channel conductivity, functioning as a photon-driven charge control layer. For example, Huang et al. demonstrated that a diphenylanthracene (DPA)-based TTA-UC copolymer integrated into a transistor memory significantly enhanced device performance under visible light. The upconverted emission from the DPA annihilator improved photogating effects, leading to faster

doi:10.6342/NTU202503178

programming speeds and improved data retention characteristics.[41] Similarly, Huang et al. showed that TTA-UC in the poly(1-pyrenemethyl methacrylate) [PPyMA]/tris(2-phenylpyridine)iridium(III) [Ir(ppy)$_3$] system prolongs exciton lifetime and enables delayed fluorescence to be reabsorbed by 2,7-dioctylbenzo[*lmn*][3,8]phenanthroline-1,3,6,8(2*H*,7*H*)-tetraone (C8-NDI), enhancing photogating and improving memory performance. This highlights delayed fluorescence as a viable strategy to boost photoresponsive transistor memory. [42] This indicates that delayed fluorescence is a viable strategy for enhancing the performance of photoresponsive transistor memory devices.

In addition to individual experimental studies, recent research and review articles have increasingly emphasized the potential of TTA-UC for managing triplet excitons in the field of organic optoelectronics. The TTA-UC mechanism enables the fusion of two low-energy triplet excitons into a single high-energy singlet exciton, effectively bridging photon emission and charge manipulation—an advantage particularly suited to the design of hybrid optoelectronic devices. [43] One of the most significant advantages of TTA-UC is its ability to operate without relying on heavy-metal-based phosphors, thereby contributing to the development of environmentally friendly and sustainable device strategies. Recent studies have reported the design of air-stable TTA-UC systems using block copolymer micelles, which not only enhance triplet energy transfer efficiency but also substantially reduce the impact of oxygen quenching, making them more practical for operation under ambient conditions. [44]

In conclusion, the excellent compatibility of TTA-UC systems with flexible substrates and solution-based processing renders them highly suitable for future applications in wearable and large-area optoelectronic devices.[45] These advances demonstrate that TTA-UC functions not only as a luminescence mechanism but also as a strategic approach for enhancing the performance and sustainability of organic electronic components.

1.3.3 Room-Temperature phosphorescent (RTP)

RTP has emerged as a promising frontier in the field of organic luminescent materials, enabling unique functionalities across a range of optoelectronic applications. RTP is characterized by a radiative transition from the lowest T_1 to the ground state (S_0), a spin-forbidden process under quantum mechanical selection rules. Due to this spin prohibition, the rate of phosphorescent decay is significantly slower than that of fluorescence, leading to emission lifetimes ranging from milliseconds to several seconds. As shown in **Figure 1.7**, the generation of RTP involves three key photophysical processes: (1) photoexcitation of the molecule into a S_1, (2) ISC from S_1 to T_1, and (3) radiative decay from T_1 to S_0. The efficiency of RTP thus depends critically on the ISC rate and the suppression of nonradiative decay pathways from T_1.[46] In organic systems, ISC is typically inefficient due to the weak SOC inherent to light elements such as carbon, hydrogen, nitrogen, and oxygen. Consequently, achieving observable RTP at room temperature requires strategic molecular design and environmental engineering to promote ISC and protect the triplet state from quenching by molecular motion, heat, or oxygen.

To enhance ISC, several strategies have been employed, such as incorporating n–π* transitions, introducing halogen atoms to invoke the heavy-atom effect, forming charge-transfer states, and utilizing photoinduced conformational changes that increase SOC. In addition, matrix engineering approaches, including the incorporation of phosphors into rigid polymers or crystalline lattices, can effectively restrict molecular vibrations and reduce oxygen permeability, thereby minimizing nonradiative decay from the T_1.

Historically, efficient RTP has been largely associated with inorganic and organometallic compounds that rely on heavy-metal elements like iridium or platinum to achieve strong SOC and facilitate ISC. However, due to concerns over cost, toxicity, and limited availability, there has been a growing interest in metal-free organic alternatives, leading to the development of purely organic room-temperature phosphorescence (ORTP) materials. [46, 47] Recent studies have demonstrated that specific molecular packing, including H-aggregation and clustering-induced emission, plays a pivotal role in prolonging RTP lifetimes under ambient conditions.[48] For example, polymer-based ORTP materials have gained attention for their dual function: serving as both phosphorescent hosts and protective matrices. PVA and PMMA are frequently employed due to their ability to restrict intramolecular vibrations and act as oxygen barriers. [46, 47]

Although RTP has demonstrated considerable promise in fields such as sensing, encryption, and imaging, its practical implementation in OFETs for nonvolatile memory and neuromorphic applications remains largely unexplored. Nevertheless, the unique photophysical characteristics of RTP materials position them as promising candidates for these emerging technologies. One of the most compelling advantages of RTP is its intrinsic long-lived triplet state, which allows optical non-volatile memory retention without the need for continuous power input. In addition, RTP materials exhibit remarkable sensitivity to external stimuli such as light, heat, mechanical stress, and oxygen concentration. This stimulus-responsiveness provides a versatile platform for designing rewritable and optically controllable memory devices. Data states can be reversibly toggled by localized heating or photoactivation, allowing for dynamic manipulation of logic and memory functions in optoelectronic systems.[46, 47, 49] Moreover, RTP materials exhibit efficient performance in amorphous and polymeric matrices, ensuring compatibility with flexible electronics and solution-based processing techniques.

doi:10.6342/NTU202503178

Their photostability and compatibility with organic semiconductors enable seamless incorporation into OFET architectures without compromising charge transport properties.

In summary, RTP in purely organic and metal-free systems holds strong potential for next-generation OFET-based memory and neuromorphic applications. Its key properties include persistent luminescence, spin multiplicity, and responsiveness to external stimuli. However, its application in these areas remains limited. Future research should focus on utilizing these features to develop optically addressable and reconfigurable nonvolatile memory systems.

1.3.4 Organic Long Persistent Luminescence (OLPL)

Persistent luminescence (LPL) refers to the continued emission of light from a material after the cessation of external excitation. In organic systems, organic long persistent luminescence (OLPL) specifically denotes the ability of organic compounds to sustain visible afterglow for durations ranging from several seconds to hours at room temperature. This behavior sharply contrasts with conventional phosphorescence, which typically decays exponentially within microseconds to milliseconds. Despite growing research interest in OLPL, the definition of “long” remains ambiguous. As Xu and Tanabe have observed, afterglow durations are often reported in arbitrary units and measured under differing instrumental sensitivities, making cross-study comparisons problematic. Further complicating this issue is the absence of standardized terminology. The literature features a wide variety of descriptors referring to similar phenomena, combining adjectives such as “long”, “long-lasting”, “persistent”, and “delayed” with terms like “afterglow”, “phosphorescence,” and “luminescence.” These appear in various forms, including but not limited to “long-lasting phosphorescence (LLP)”, “long persistent phosphorescence (LPP)”, “long persistent luminescence (LPL)”, “delayed phosphorescence", and "long afterglow".[50] This inconsistency in nomenclature reflects the evolving understanding of OLPL but also underscores the need for a unified terminology to enable precise comparison and systematic classification across different OLPL systems.

Mechanistically, OLPL in host–guest organic systems is governed by a photo-induced charge transfer mechanism. As illustrated in **Figure 1.8**, upon light excitation, electrons are transferred from donor (guest) molecules to acceptor (host) molecules, leading to the formation of an intermolecular charge-transfer (CT) state at the donor–acceptor interface. This CT state is subsequently stabilized by local traps within the host matrix, resulting in a long-lived charge-separated (CS) state. This process ultimately leads to charge recombination (CR), releasing stored optical energy as delayed fluorescence or phosphorescence, depending on the spin dynamics of recombination. [51] Unlike phosphorescence, which follows first-order kinetics and decays exponentially, OLPL decay follows a power-law function (Intensity $\propto t^{-m}$, where m ranges from 0.1 to 2), indicating a second-order kinetic process. This prolonged emission results from the slow recombination of spatially separated charge carriers.[52]

Furthermore, both emission characteristics and afterglow duration can be finely tuned by modulating the energy level alignment and molecular packing through careful host–guest material design.[51] In recent years, various strategies have been developed to enhance the performance of OLPL systems. For instance, Lin et al. reported a flexible, transparent polymer-based OLPL system using *N,N,N′,N′*-tetramethylbenzidine (TMB) as the donor and poly(arylene ether phosphine oxide) [PBPO] as the acceptor. This system exhibited OLPL lasting over 7 minutes under ambient conditions after low-power excitation, without requiring strong photoirradiation or cryogenic temperature.[53] Zhang et al. realized narrowband OLPL emission by promoting energy transfer from the host to a multiresonance TADF emitter, which subsequently emitted from its locally excited singlet state with high spectral purity.[54] Moreover, Liu et al. developed a crystalline host–guest OLPL system designed for in situ anti-counterfeiting applications. Their approach involved *N*,*N*′-diphenyl-*N*,*N*′-bis(4-methylphenyl)-4,4′-biphenyldiamine (*p*-TPD) guest molecules doped into various easily crystallizable hosts, producing afterglow durations of 2.0 to 4.5 seconds, and enabling water-stable paper–ink encryption strategies. [55]

Although OLPL materials have demonstrated promising applications in fields such as anti-counterfeiting, bioimaging, and optical encryption, their integration into electronic devices, particularly OFETs and nonvolatile memory, remains largely unexplored. Nevertheless, the intrinsic properties of OLPL indicate strong potential for these applications. A key advantage is their ability to maintain visible luminescence without continuous power input, providing an energy-efficient approach to optically addressable nonvolatile memory. The persistent afterglow can serve as a physical indicator of stored information and enables long-term memory retention. From the perspective of materials integration, polymer-based OLPL systems using host matrices such as PMMA or PVA offer excellent film-forming properties and are compatible with solution-based fabrication methods. This makes them suitable for incorporation into OFET architectures. Despite these advantages, OLPL has not yet been practically applied in OFET-based memory devices, which presents a significant opportunity for future research. In addition, the photophysical stability of OLPL materials under ambient conditions further supports their potential for real-world electronic applications.

In conclusion, OLPL materials, especially their purely organic and metal-free forms, represent a promising yet underexplored approach for the development of multifunctional optoelectronic systems. Their persistent luminescence, environmental responsiveness, and compatibility with solution-based processing make them strong candidates for next-

doi:10.6342/NTU202503178

generation nonvolatile memory technologies.

1.4 Research Objectives

As the development of wearable electronics, neuromorphic systems, and edge devices continues to progress, there is a growing demand for next-generation memory technologies that are nonvolatile, optically controllable, and energy-efficient. OFET-based photomemory devices are regarded as promising candidates due to their structural tunability, low fabrication cost, and compatibility with flexible substrates. However, current systems often face challenges in achieving both long-term data retention and rapid, stimulus-responsive performance under ambient conditions. Traditional charge storage materials typically rely on instantaneous photoexcitation and fast recombination dynamics, which limit the operational timescale and stability of the memory states.

To overcome these limitations, emerging photophysical mechanisms involving organic delayed exciton emission have attracted increasing attention, particularly those based on RTP and OLPL. These systems rely on long-lived triplet excitons or stabilized charge-separated states to maintain luminescence and retain signals after the cessation of external excitation. Although interest in these mechanisms has grown significantly, their application in transistor-based memory platforms remains largely unexplored. In particular, the relationship between extended excited-state dynamics and charge-trapping behavior in OFET memory devices requires systematic investigation.

Therefore, this thesis aims to integrate RTP and OLPL materials into the architecture of OFET memory devices, in order to explore the potential of delayed luminescence mechanisms in photomemory applications. These purely organic and metal-free luminescent materials, characterized by long exciton lifetimes and excellent stability, are expected to enhance the memory window, charge retention capability, and photoresponsiveness of the devices. The results may provide new directions for the material and structural design of optically programmable nonvolatile memory systems. The specific research objectives are as follows:

1. <u>In Chapter 2, Application of Organic Room-Temperature Phosphorescent Materials in High-Efficiency Photomemory and Synaptic Phototransistors:</u> we investigate the application of metal-free RTP materials in OFET-based floating-gate photomemory and photosynaptic devices. Two electron-deficient dianhydride compounds, 3,3′, 4,4′-diphenyl sulfone tetracarboxylic dianhydride (DPS) and 3,3′, 4,4′-benzophenone tetracarboxylic dianhydride (BTDA), are employed as RTP emitters and blended with PS to form the floating-gate electret layer. These materials exhibit long-lived triplet excitons, which effectively prolong charge separation and retention within the device, thereby enhancing memory performance. We examine their photo-assisted programming behavior, memory window, and operational stability. Furthermore, we evaluate their synaptic plasticity under optical stimulation by varying key pulse parameters, including PPF, SNDP, STDP, SRDP, and SIDP. Finally, a handwritten digit image recognition task is simulated to validate the practical potential of these RTP-based devices in artificial neural network applications.

2. <u>In Chapter 3, Organic Long Persistent Luminescence Materials Based on Host–Guest Systems for Phototransistor Memory Applications:</u> we extend our study to OLPL systems for OFET-based photomemory applications to further explore delayed luminescence mechanisms beyond triplet emission. We design host–guest architectures using PMMA as the host matrix, incorporating N,N, N′,N′-tetraphenylbenzidine (TPB), N, N′-

doi:10.6342/NTU202503178

bis(naphthalen-1-yl)-N, N'-bis(phenyl)-benzidine (NPB), and 2,7-bis(N-(1-naphthyl)aniline)-9,9-dimethylfluorene (DMFL-NPB) as guest emitters. Through energy level design between host and guest, combined with optimization of guest concentration, we aim to achieve persistent afterglow emission and enhanced charge trapping upon photoexcitation. The effects of various host–guest combinations on emission lifetime, memory window, and device stability are systematically investigated. Unlike conventional fluorescent materials, OLPL systems can maintain luminescence long after excitation has ceased, enabling extended signal retention without continuous power input. Their prolonged exciton behavior, along with their metal-free composition and compatibility with solution processing, underscores their promise as next-generation materials for nonvolatile optoelectronic memory with enhanced retention performance and environmental stability.

By simultaneously exploring both RTP- and OLPL-based charge trapping mechanisms, this study provides comparative insights into how delayed emission mechanisms influence device performance from both excitonic and charge-separated state perspectives. Unlike previous RTP-based or OLPL-based memory demonstrations that rely on hybrid or metal-containing systems, this thesis proposes a fully organic, metal-free strategy with direct integration into OFET architectures.

1.5 Tables and Figures

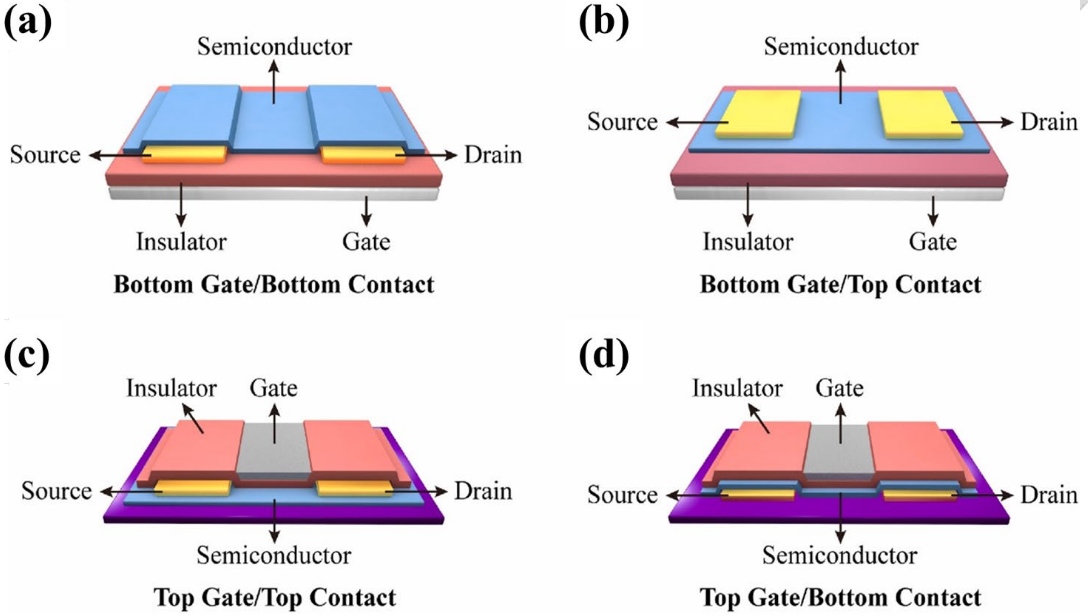

Figure 1.1 The four commonly utilized configurations of OFETs include: (a) bottom-gate/bottom-contact, (b) bottom-gate/top-contact, (c) top-gate/bottom-contact, and (d) top-gate/top-contact.[7]

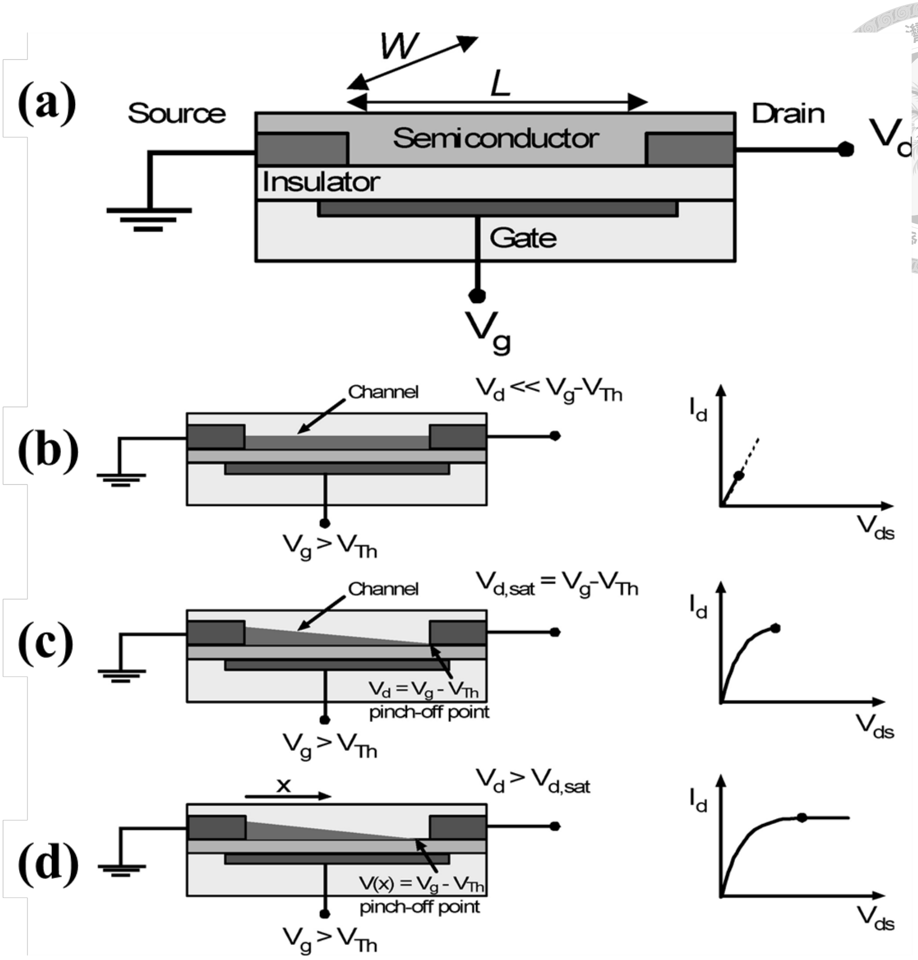

Figure 1.2 (a) Device structure of a OFET. (b–d) Operational regimes of the transistor: (b) linear region, (c) pinch-off point, and (d) saturation region with corresponding output behavior.[8]

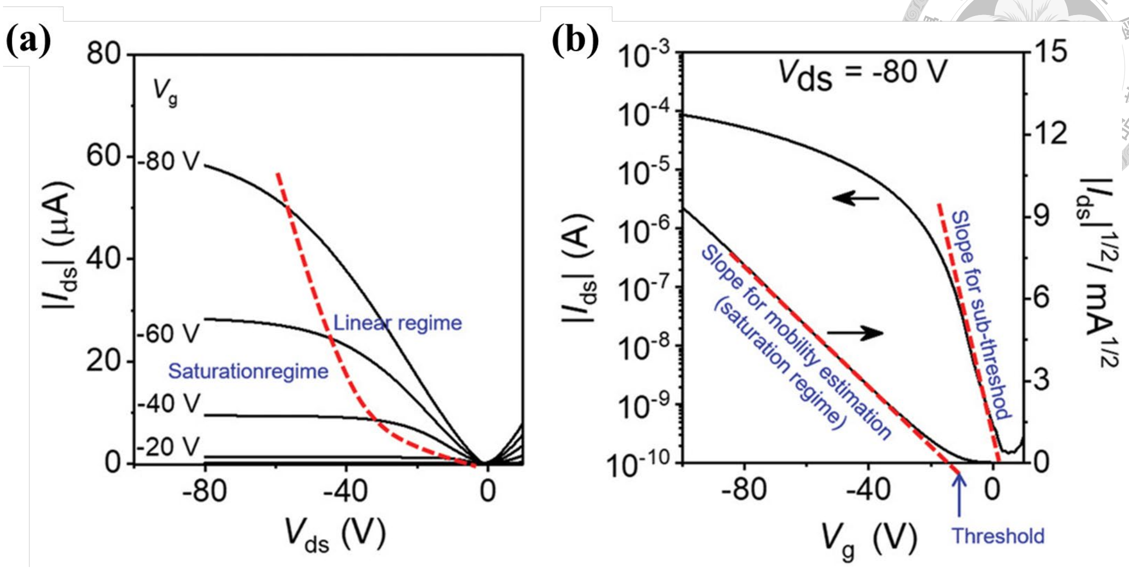

Figure 1.3 (a) Output and (b) Transfer characteristics of p-type OFETs.[11]

doi:10.6342/NTU202503178

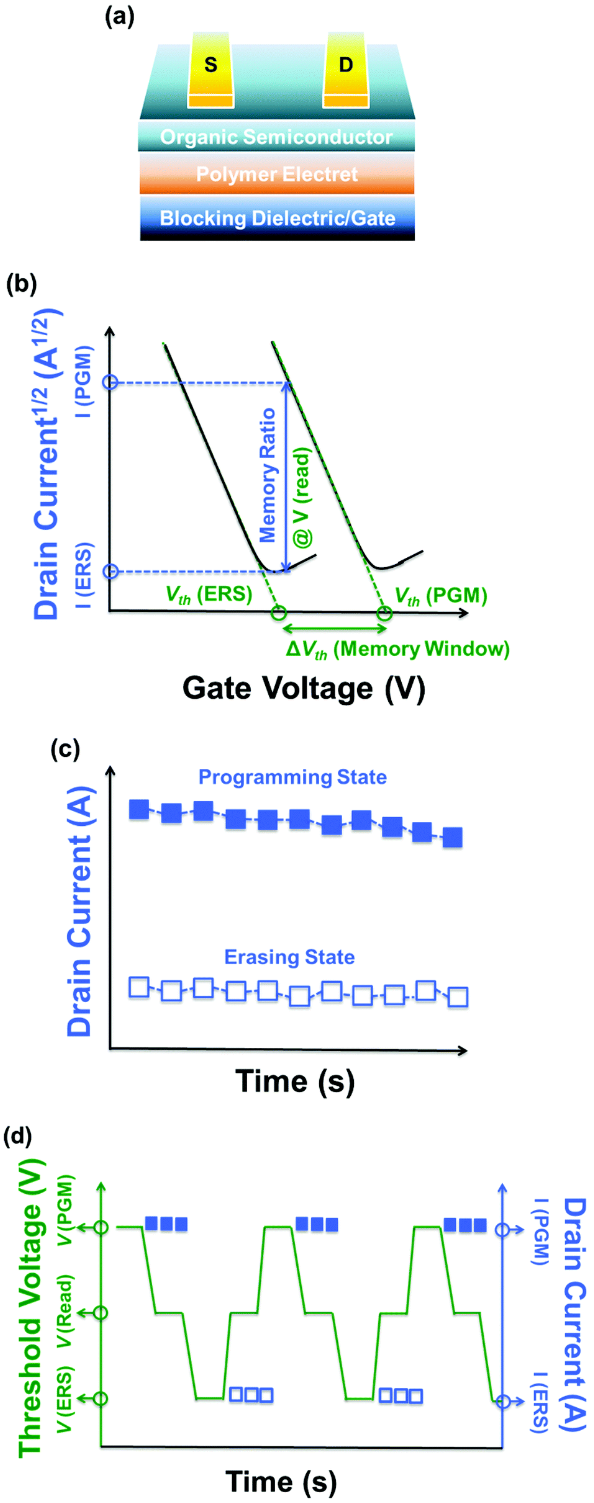

Figure 1.4 (a) Structural illustration of an OFET-based memory device. (b) Plot of √Id vs. V_g under specific bias conditions, used to extract the ΔV_{th} and calculate the I_{ON}/I_{OFF}. ((c) Charge retention over time. (d) Endurance under repeated WRER cycles.[12]

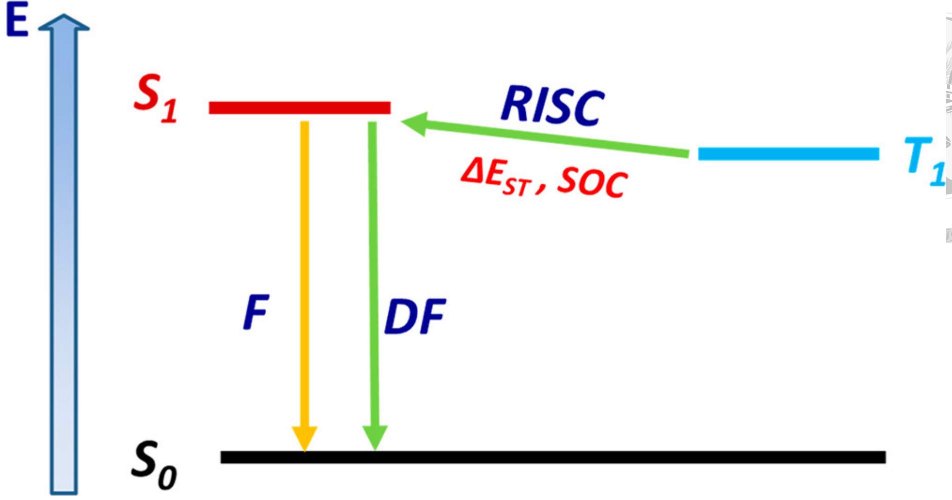

Figure 1.5 Energy level diagram illustrating the TADF mechanism via thermally activated RISC from T_1 to S_1.[33]

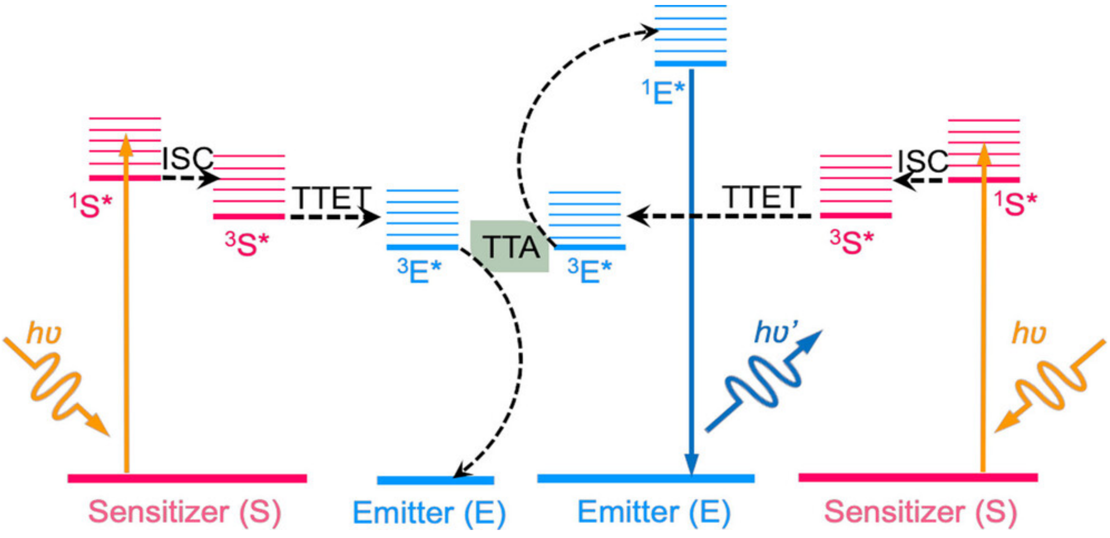

Figure 1.6 Schematic energy level representation of the TTA-UC process.[40]

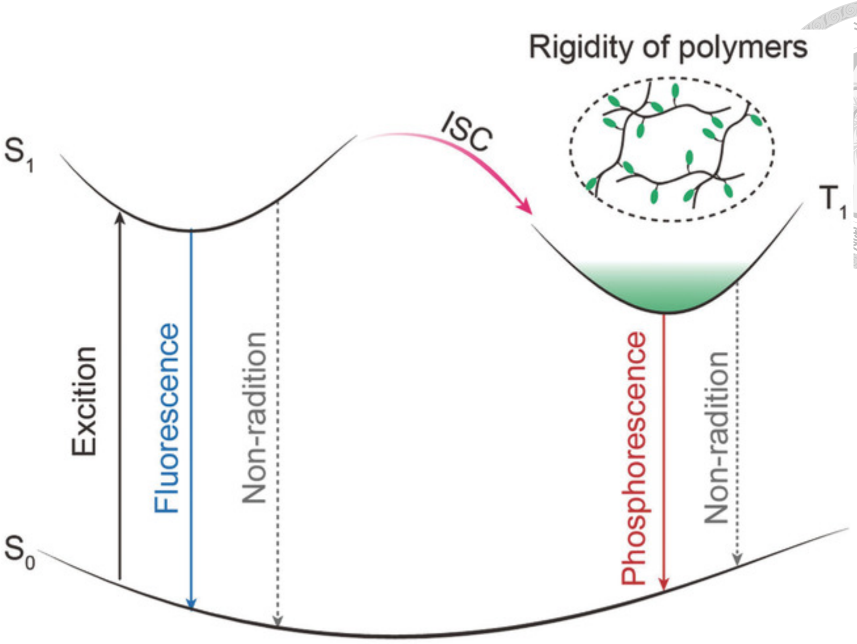

Figure 1.7 Jablonski diagram showing excitation, ISC, fluorescence and phosphorescence pathways relevant to RTP in polymer-based materials.[46]

doi:10.6342/NTU202503178

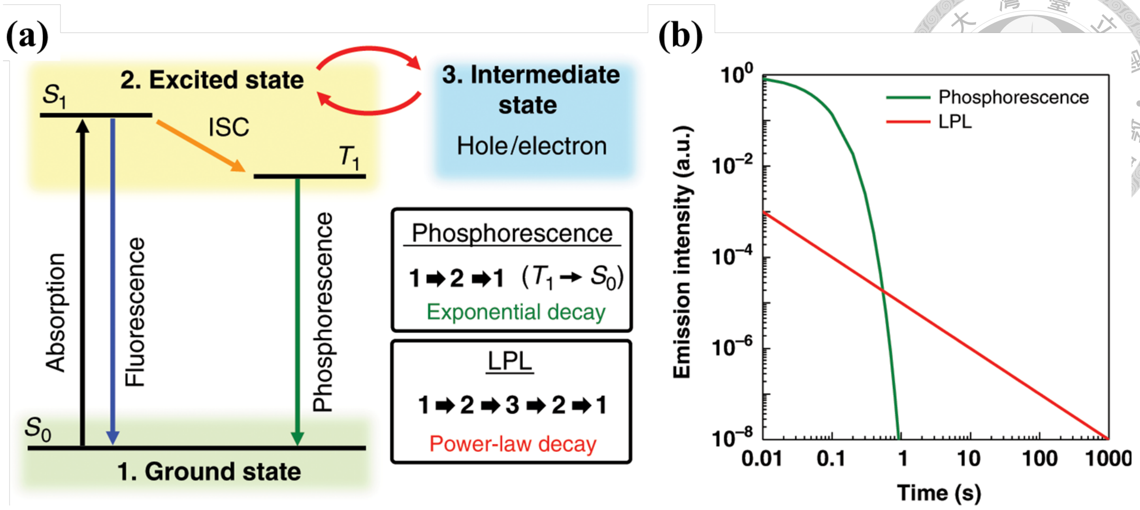

Figure 1.8 (a) Simplified energy diagram showing fluorescence, phosphorescence, and LPL. In LPL, emission occurs via an intermediate state such as a CT state, a CS state, and CR, leading to prolonged afterglow beyond typical triplet decay. (b) Representative comparison of emission decay behaviors: phosphorescence exhibits a rapid exponential decay, whereas LPL shows a much slower, power-law decay over time.[52]

Chapter 2 Application of Organic Room-Temperature Phosphorescent Materials in High-Efficiency Photomemory and Synaptic Phototransistors

Our findings have been published in *Advanced Intelligent Discovery* **2025**, *1*, 2500008, under the title *"Organic Room-Temperature Phosphorescent Materials for High-Performance Floating Gate Photomemory and Synaptic Phototransistor Applications"* (DOI: 10.1002/aidi.202500008).

2.1 Introduction

As modern computational demands grow, traditional computing systems based on the Von Neumann architecture are encountering significant challenges, including high energy consumption and pronounced performance bottlenecks. This architecture physically separates computational units from memory units, resulting in frequent data transfers that exacerbate these limitations, particularly when handling unstructured data and striving for parallel processing. Moreover, it cannot learn or process complex information like biological neural systems.[56-58] Neuromorphic computing is emerging as a transformative approach for next-generation computational technologies, with artificial synapses playing a foundational role in brain-inspired computation. These synapses replicate the behavior of biological counterparts, particularly short-term plasticity (STP) and long-term plasticity (LTP). LTP is essential for memory formation, enabling the transition from short-term to long-term memory. This process can be modeled by adjusting pulse number, width, and frequency, reflecting how repetition and extended recall strengthen memory retention. These functions provide an essential foundation for the learning and memory processes in artificial neural networks (ANNs).[59-61] Unlike traditional "0/1" binary storage systems, ANN mimics the interaction between neurons and synapses in biological neural networks to achieve brain-like decision-making and learning abilities, significantly improving data processing efficiency.[62] Its applications cover brain-like computing and artificial sensory systems. Human beings can distinguish pitches, recognize images, and identify faces due to the ability to learn sensory. Sensory stimuli are first captured by specialized receptors located on sensory neurons. These signals travel through incoming axons to synaptic connections, where postsynaptic neurons receive and interpret the information for further processing.[63, 64]

Synaptic devices can be categorized into two-terminal, three-terminal, and multi-terminal structures, each designed for specific functions and applications. Two-terminal devices, such as resistive random-access memory (RRAM) and phase-change memory (PCM), are characterized by their simple structure and low manufacturing cost, making them suitable for miniaturized and high-density memory arrays. However, these devices cannot simultaneously perform signal transmission and learning processes, which limits their ability to emulate natural synapses.[65-67] In contrast, three-terminal and multi-terminal synaptic transistors, including floating-gate field-effect transistors (FGFETs), ferroelectric field-effect transistors (FeFETs), and optoelectronic field-effect transistors (OFETs), incorporate additional gate terminals, enabling a more comprehensive simulation of synaptic behaviors. These transistors support simultaneous signal processing and self-learning while offering enhanced operational stability and tunability.[65, 68-70] Memory devices can also be categorized into two-terminal and three-terminal structures. Two-terminal memory devices typically consist of two electrodes and feature a simple structure where data is read with a voltage.[71, 72] However, this reading process may interfere with the memory state, resulting in lower stability. In contrast, three-terminal memory devices utilize a gate for non-contact reading, preventing interference with the stored state and enabling faster read and write speeds. Additionally, the three-terminal structure supports independent optoelectronic operations. It is particularly suitable for multi-functional memory applications, especially in optoelectronic memory devices, and it offers excellent stability and long-term operability.[73, 74]

Light, as a controllable external stimulus, has demonstrated the capability to enhance the stability of non-volatile memory while replicating the learning and memory behaviors of biological neural synapses. With the continuous advancement of technology, increasing attention has been directed toward the interaction between photonic and electronic behaviors, particularly the role of charge trapping, charge transfer, and energy transfer mechanisms in shaping optoelectronic devices' overall performance and stability.[75] For memory applications, key materials must exhibit an energy barrier that prevents the recombination of positive and negative charges after removing the electric field, ensuring stable, non-volatile storage. Charge trapping occurs when charge carriers become localized in traps at interfaces, defects, or dielectric layers, enabling charge retention without a continuous power supply.[76, 77] The fast response time of switching processes, driven by field-induced charge transfer, determines the device's switching speed.[78, 79] Energy transfer is a process where excitation energy is transferred without altering chemical bonds, typically via electronic excitation, and can occur through radiative or nonradiative mechanisms. This phenomenon is commonly observed in molecular, atomic, or solid-state systems. The timescales of energy transfer vary depending on the nature of the excited state: singlet-state energy transfer typically occurs on the scale of picoseconds

doi:10.6342/NTU202503178

to nanoseconds, while triplet-state energy transfer, with its longer lifetimes, can take place over milliseconds or even seconds. Moreover, energy transfer is crucial in converting energy between singlet and triplet states, which is essential for maintaining stable excited states. This process is vital for supporting long-term energy storage and charge transport, directly influencing the stability and performance of devices.[80, 81]

Organic materials, due to the diversity and flexibility of their excited-state structures, exhibit a wide range of luminescent phenomena, including conventional fluorescence and phosphorescence, as well as other delayed emission mechanisms.[82, 83] In recent years, studies have shown that organic afterglow effects have significant application potential in enhancing the photoresponse and speed of optoelectronic devices. The mechanisms of delayed luminescence can be categorized into two main types: TADF and phosphorescence. TADF operates through reverse intersystem crossing (rISC), converting triplet excitons to singlet excitons for subsequent emission.[84, 85] In contrast, phosphorescence is achieved via radiative transitions that are quantum mechanically forbidden, occurring between the excited triplet state and the ground state, relying on intersystem crossing (ISC) to utilize triplet state emission directly. Room-temperature phosphorescence (RTP) materials have attracted considerable interest for their ability to produce stable and long-lived triplet-state emissions under ambient conditions. These materials have become a key focus in luminescence research with their extended lifetimes and unique excited-state properties.[86, 87] Traditionally, RTP materials rely on precious metal complexes, such as iridium and platinum, to enhance spin-orbit coupling, which is essential for phosphorescence.[88] While these metals effectively facilitate phosphorescence, their high cost and biological toxicity limit widespread application.

Recent research has shifted towards developing metal-free RTP materials to overcome these challenges, which can achieve efficient phosphorescence without heavy metals. By introducing heteroatoms like halogens, nitrogen, phosphorus, or sulfur and optimizing molecular structures, researchers have been able to significantly enhance spin-orbit coupling and reduce nonradiative decay, thereby improving the performance of these materials. Additionally, incorporating polymer matrices and leveraging weak intermolecular forces, including hydrogen bonding and π–π stacking, further boosts the materials' luminescence efficiency and stability. The successful development of metal-free RTP materials addresses heavy metal-based materials' cost and safety concerns and expands their potential for real-world applications.[89-91] Chen et al. utilized the triplet excitons in RTP organic-inorganic hybrid perovskites to enhance the performance of non-volatile photomemory devices, demonstrating the potential of RTP materials in optoelectronic transistor applications.[92] A long exciton lifetime is essential for efficient charge separation and high optoelectronic performance. In RTP materials, long-lived triplet excitons provide a longer time window for charge separation, reducing recombination and improving exciton-to-charge conversion under an external electric field. This extended lifetime ensures charge carriers remain available for transport, enhancing the photoresponse of the memory device. Furthermore, the significantly long timescale of electron–hole recombination in RTP-based materials enables the sustained retention of charge carriers, which is particularly beneficial for optoelectronic memory applications. This characteristic is essential for photonic synaptic behavior, where persistent photogenerated carriers mimic the biological process of memory retention and gradual synaptic weight modulation. The extended exciton lifetime facilitates charge accumulation and transport, leading to an enhanced and prolonged photoinduced conductance change, a fundamental requirement for synaptic operations.[92-94] RTP materials currently used in optoelectronic transistor devices are typically based on organometallic complexes or organic-inorganic hybrids. However, applying pure organic

doi:10.6342/NTU202503178

molecules with RTP remains an unexplored area. Therefore, using metal-free RTP organic molecules to enhance memory devices' fast read-write capabilities or improve optoelectronic synaptic devices' visual recognition capabilities holds significant potential.

This research utilizes 3,3′, 4,4′-Diphenyl sulfone tetracarboxylic dianhydride (DPS) and 3,3′, 4,4′-Benzophenone tetracarboxylic dianhydride (BTDA) as RTP materials, with polystyrene (PS) as an insulating polymer to form a floating gate dielectric, and pentacene as the semiconductor channel. This system demonstrates the new applications of organic RTP molecules in optoelectronic memory and synaptic devices. For comparison, DPS and BTDA were separately reacted with methylamine hydrochloride to synthesize *N*, *N*′-dimethyl-3,3′, 4,4′-diphenyl sulfone tetracarboxylic diimide (DPS-C) and *N*, *N*′-dimethyl-3,3′,4,4′-benzophenone tetracarboxylic diimide (BTDA-C), which do not exhibit RTP properties, followed by purification via sublimation. The film morphology was observed using atomic force microscopy (AFM), while UV–vis absorption spectroscopy and photoluminescence (PL) phosphorescence spectroscopy were employed for optical performance analysis. Additionally, phosphorescence decay systems were used to measure the phosphorescence lifetime of the RTP materials. The results show that the BTDA/PS system exhibited the best light response performance as the electron trapping layer. Furthermore, the study explored light-paired-pulse facilitation (PPF). It investigated the plasticity of short-term plasticity (STP) to long-term plasticity (LTP) via spike-number dependent plasticity (SNDP), spike-time dependent plasticity (STDP), spike-rate dependent plasticity (SRDP), and spike-intensity dependent plasticity (SIDP) by altering pulse number, time, rate, and intensity. Finally, the study employed a human brain-like recognition system to simulate learning processes and efficiently distinguish the handwritten digits.

doi:10.6342/NTU202503178

2.2 Experimental Section

2.2.1 Materials

3,3′, 4,4′-Diphenylsulfone tetracarboxylic dianhydride (DPS, >99.0%) and 3,3′, 4,4′-Benzophenone tetracarboxylic dianhydride (BTDA, >96.0%) were purchased from Tokyo Chemical Industry, BTDA was further purified before use. Polystyrene (PS, M_w = 192,000 g/mol), pentacene (99%), and *N*, *N*-Dimethylacetamide (DMAc, anhydrous, 99.8%) were purchased from Sigma-Aldrich and used without further purification.

2.2.2 Fabrication of the Devices

The dianhydride molecules (DPS and BTDA) and diimide molecules (DPS-C and BTDA-C) were dissolved in *N*, *N*-dimethylacetamide (DMAc) at 5 mg mL^{-1}, respectively, while PS was dissolved in DMAc at 20 mg mL^{-1}. The source and synthesis of these materials are described in the Supporting Information. The solutions were stirred overnight, followed by filtration with a 0.22 μm polytetrafluoroethylene syringe filter. Then, the dianhydride and diimide solutions were mixed with the PS solution in a volume ratio of 1/2 to form the DPS/PS, BTDA/PS, DPS-C/PS, and BTDA-C/PS solutions, respectively, which were stirred overnight to ensure uniform mixing. The highly n-doped silicon wafers with a 100 nm-thick SiO_2 layer were first pretreated by exposure to a UV–ozone cleaner for 30 min to remove surface impurities and increase hydrophilicity. Afterward, the solutions were spin-coated to the wafers at 2000 rpm for 60 s under a nitrogen atmosphere to form the thin films. The samples were vacuumed for 30 min to remove residual solvents and ensure the formation of high-quality dielectric layers. A 50 nm pentacene semiconductor layer was thermally evaporated onto the dielectric layer at a controlled rate of 0.2–0.3 Å s^{-1}, followed by the deposition of a 70-nm-thick Au layer through a patterned shallow mask with the channel dimensions of 1000 μm in width (W) and 50 μm in length (L) to create the source and drain electrodes. The thermal deposition process was conducted within a vacuum chamber at 10^{-7} Torr pressure.

2.2.3 Characterization

The X-ray diffraction (XRD) spectra were acquired using a Rigaku MiniFlex. Fourier-transform infrared (FTIR) spectra were obtained using Attenuated Total Reflectance (ATR) with a DIGILAB FTS-3500GX spectrophotometer. The UV–vis absorption spectra were acquired using a Hitachi U-4100 spectrophotometer. The HOMO levels of the molecules were obtained through the ultraviolet photoelectron spectroscopy (UPS) measurements conducted with a Thermo Scientific Nexsa G2 system. At the same time, the bandgap was estimated from the absorption onset observed in the UV–vis spectra. The film morphologies were analyzed using AFM (Hitachi 5100N). The lifetime decay profiles of phosphorescence emission and PL and phosphorescence emission spectra were measured using a Jobin Yvon Fluorolog-3 spectrofluorometer. The electrical performance of the transistor memory devices was characterized using a Keithley 4200-SCS semiconductor parameter analyzer under a nitrogen atmosphere in a glove box. The devices' transfer curves were analyzed by sweeping the V_g from 30 to −60 V with the V_d fixed at −40 V. The electrical erasing process was achieved by applying $V_g = -50$ V for 1 s. In contrast, a photo-assisted electrical writing process was carried out using 265 nm light (285 mW cm^{-2}) and $V_g = 0$, 10, 20, and 30 V for 10 s, respectively. The photosynaptic transistors were measured using a Keithley 2634B (Keithley Instruments Inc.) inside a nitrogen-filled glovebox. A 265-nm UV light source from Titan Electro-Optics Co., Ltd. was employed, with its intensity verified using a laser power sensor (Ophir pd300-UV-193). The PPF ratio and SNDP, STDP, SRDP, and SIDP measurements were conducted under a V_d of −10 V.

2.2.4 Simulation of Image Recognition System

The simulation was conducted using MATLAB. Initial digital images (28 × 28 pixels) were sourced from the MNIST database. Random noise with a maximum intensity of 100% was added to the pixels to generate noisy images, followed by normalizing the brightness values of the noisy images to a range of 0–255. Subsequently, a denoising array, in which the digit contours were composed of PPF ratios, was applied to the noisy images, and the pixel values were further converted to gray values for preprocessing. Finally, the denoised digital images were input into a 784 × 256 × 128 × 10 neural network to simulate the image recognition capability of the human brain.

2.3 Results and Discussion

2.3.1 Synthesis and Characterization of DPS-C and BTDA-C

Following the synthetic scheme shown in **Figure 2.1a**, a mixture of DPS (1363 mg, 3.8 mmol) and methylamine hydrochloride (641.4 mg, 9.5 mmol) in glacial acetic acid (38 mL) was refluxed at 120 °C for 24 hr under a nitrogen atmosphere. Water was added after cooling to room temperature, and the resulting precipitate was filtered and washed with methanol to obtain the white solid (1265.4 mg, 86.5%). ^{1}H NMR (500 MHz, *d*-DMF, **Figure 2.1b**), δ (ppm): 8.68–8.65 (d, 2H), 8.57–8.56 (d, 2H), 8.18–8.15 (d, 2H), 3.15–3.12 (s, 6H). Next, following the synthetic scheme shown in **Figure 2.2a**, a mixture of BTDA (1263.2 mg, 3.9 mmol) and methylamine hydrochloride (661.5 mg, 9.8 mmol) in glacial acetic acid (39 mL) was refluxed at 120 °C for 24 hr under a nitrogen atmosphere. Water was added after cooling to room temperature, and the resulting precipitate was filtered and washed with methanol to obtain the white solid (1164.1 mg, 85.2%). ^{1}H NMR (500 MHz, *d*-DMF, **Figure 2.2b**), δ (ppm): 8.31–8.28 (d, 2H), 8.20–8.18 (d, 2H), 8.13–8.10 (d, 2H), 3.18–3.16 (s, 6H).

2.3.2 Device Structure and Morphology Analysis

The device structure used in this study is illustrated in **Figure 2.3a**. DPS and BTDA contain dianhydride compounds and are used as RTP materials. In contrast, DPS-C and BTDA-C, synthesized by reacting DPS and BTDA with methylamine hydrochloride to form diimide compounds, serve as control materials without RTP effects. The synthesis methods follow previously reported procedures[95] including 1H NMR are detailed in **Figures 2.1** and **Figures 2.2**, and X-ray diffraction (XRD) measurements are shown in **Figure 2.4**. In this study, XRD analysis was conducted to investigate the structural characteristics of four organic small molecules—DPS, DPS-C, BTDA, and BTDA-C—within the PS matrix. The XRD spectra indicate that, although these organic materials exhibit good crystallinity in their pure form, the spin-coated film samples primarily exist in an amorphous dispersed state within the PS matrix, likely due to the processing conditions, which results in a less ordered molecular arrangement. The RTP capabilities of dianhydride-based compounds arise primarily from strong intermolecular forces, such as hydrogen bonding and π–π stacking, in their molecular structures. These interactions enhance molecular rigidity, suppress nonradiative decay, and promote spin-orbit coupling (SOC) and ISC. However, when dianhydride-based compounds undergo chemical transformation into diimide-based compounds, these intermolecular interactions are weakened, leading to reduced molecular rigidity and ISC efficiency, ultimately eliminating RTP effects. To investigate the behavior of this system, PS is selected as the polymer matrix to improve molecular dispersion and construct floating gate dielectrics.

doi:10.6342/NTU202503178

Pentacene is employed as the semiconductor material, and a bottom-gate/top-contact device configuration is used for the study.

Figure 2.3b presents the floating gate thin films' UV–vis absorption spectra, showing absorption ranges primarily within the ultraviolet region. After methylation with methylamine hydrochloride, DPS transforms into DPS-C, where molecular aggregation leads to a redshift in the absorption band. In contrast, the methylation of BTDA has minimal impact on its molecular aggregation and absorption behavior. To preliminarily understand the properties of the materials studied and explore their potential in device applications, the UV-visible absorption spectra shown in **Figure 2.5a** and ultraviolet photoelectron spectroscopy (UPS) shown in **Figure 2.5b** were measured to obtain the energy level structures of the materials, as shown in **Figure 2.3c**. The absorption onset in the UV-visible absorption spectra helps determine the materials' band gap (E_g). At the same time, UPS measurements allow for the determination of the highest occupied molecular orbital (HOMO) energy levels, achieved through secondary electron cutoff and minimum kinetic energy cutoff. Furthermore, the lowest unoccupied molecular orbital (LUMO) was calculated using the formula LUMO = HOMO + E_g. Specifically, the HOMO/LUMO values for DPS, DPS-C, BTDA, and BTDA-C are (−7.18, −3.15) eV, (−7.57, −3.99) eV, (−7.21, −3.46) eV, and (−7.71, −4.00) eV, respectively. It can be observed that the E_g of BTDA is smaller compared to DPS. Moreover, the reaction between dianhydride and methylamine forms diimide, which adopts a donor-acceptor-like structure, thereby altering its energy levels and leading to a decrease in the HOMO energy level of the diimide derivatives. For pentacene and PS, the values are (−5.00, −2.70) eV and (−7.00, −0.45) eV, respectively, based on relevant literature references.[96]

AFM was employed to investigate the floating gate thin films' surface morphology, as shown in **Figure 2.3d**. The results reveal that the dianhydride-based molecules exhibit slight aggregation, while the diimide-based molecules present a relatively smooth surface. The differences in aggregation levels arise from the intrinsic intermolecular forces between the molecules. However, regardless of the aggregation extent, all the films display very smooth surfaces with roughness values less than 1 nm, providing an exceptionally flat surface for forming the pentacene semiconductor, as shown in **Figure 2.6**.

2.3.3 Optical Analysis of the RTP Materials

After confirming the morphological analysis of the materials, the investigation proceeds to examine the characteristics of RTP. **Figure 2.7a** and **Figure 2.7b** present the room-temperature photoluminescence and phosphorescence emission spectra of dianhydride and diimide molecules, respectively. It is observed that the fluorescence emission wavelengths of both dianhydride and diimide molecules are located between 350 and 500 nm. Notably, dianhydride molecules exhibit RTP characteristics, while the phosphorescence signal of diimide molecules is nearly absent, confirming the lack of RTP features in these molecules. The transformation from the dianhydride to diimide structures significantly affects the RTP properties, whereas fluorescence remains relatively unaffected.

To further understand the exciton lifetimes of RTP, the RTP lifetime decay profiles of the powdered materials are shown in **Figure 2.7c** and summarized in **Table 2.1**. Lifetime decay profiles were fitted with a bi-exponential equation:

$$F(t) = \sum_{i=1}^{n} A_i e^{\frac{t}{\tau_i}} \ (\mathrm{n} = 2) \tag{1}$$

$$\tau_{\mathrm{avg}} = \frac{\sum_{i=1}^{n} A_i \tau_i}{\sum_{i=1}^{n} A_i \tau_i} \ (\mathrm{n} = 2) \tag{2}$$

where F(t) represents the time-dependent phosphorescence intensity, A_i denotes the weighting factors, and τ_1 and τ_2 correspond to the nonradiative and radiative components of the phosphorescence decay lifetimes, respectively. Dianhydride molecules exhibit remarkably long lifetimes, with DPS reaching 2.622 ms and BTDA extending to 2.870 ms. This demonstrates that DPS and BTDA are excellent RTP materials. The DPS molecule exhibits various intermolecular interactions, such as van der Waals forces and π–π stacking interactions between C=O⋯C(C=O), which help stabilize the crystal structure and restrict the free movement of the molecules, thereby enhancing molecular rigidity. The increased rigidity effectively suppresses molecular vibrations and rotations, reducing nonradiative decay pathways and promoting the radiative decay processes. Furthermore, the C=O⋯C(Ph) interaction in DPS involves dipole–π interactions, where the carbonyl group acts as a dipole, and the π–electron system of the phenyl ring contributes to the interaction, further enhancing intermolecular alignment and stability. Atoms with n–π orbital characteristics, such as oxygen and sulfur, present in the DPS molecule can alter the electronic structure of the excited state, enhancing the SOC between the singlet state (S_1) and triplet state (T_1), thus facilitating ISC. This allows more electrons to transition into the triplet excited state, providing the basis for phosphorescence generation. Additionally, hydrogen bonding interactions, such as S=O⋯H and C=O⋯H, are present in the DPS structure, further enhancing molecular rigidity, suppressing nonradiative decay, and improving phosphorescence efficiency and stability.[93] Similar to DPS, the rigid structure of BTDA also effectively reduces molecular vibrations and rotations, thereby suppressing nonradiative decay and allowing the triplet excited state energy to be released radiatively, resulting in RTP. Furthermore, BTDA contains a benzophenone group, and its carbonyl group may play a more significant role in the RTP process. Compared to the sulfonyl group in DPS, the n–π*

doi:10.6342/NTU202503178

transition efficiency of the benzophenone carbonyl group is higher, which may lead to slightly different spin-orbit coupling characteristics in BTDA compared to DPS. Upon converting DPS and BTDA to DPS-C and BTDA-C, the dianhydride groups are replaced by diimide groups, increasing the molecules' flexibility while decreasing their rigidity and intramolecular conjugation. This structural change leads to an increase in nonradiative decay and a reduction in SOC effects within and between the molecules. As a result, the modified molecules primarily display fluorescence emission and do not exhibit the characteristic long-lived phosphorescence of DPS and BTDA.

2.3.4 Optical Analysis of the RTP Layers Stacked with the Semiconductor

To investigate the interaction between the RTP effect and the pentacene semiconductor layer and the device characteristics, the RTP lifetime histograms of the DPS and BTDA films were analyzed. The charge transfer efficiency (CTE) after layering DPS and BTDA with pentacene was calculated, as shown in **Figure 2.7d**, with measurement data detailed in **Figure 2.8a** and **Table 2.2**. The following formula can obtain CTE:

$$\mathrm{CTE} = \frac{\tau_{\mathrm{RTP\ layer}} - \tau_{\mathrm{Bilayers}}}{\tau_{\mathrm{RTP\ layers}}} \times 100\% \tag{3}$$

where τ_{avg} refers to the average lifetime of DPS and BTDA ($\tau_{\mathrm{RTP\ layer}}$) and DPS/pentacene and BTDA/pentacene (τ_{Bilayers}). Compared to the powder samples, the thin film samples exhibit shorter phosphorescence lifetimes, with DPS having a lifetime of 0.026 ms and BTDA having a longer lifetime of 0.081 ms. After layering with pentacene, the lifetime of DPS/pentacene decreased to 0.017 ms, and the lifetime of BTDA/pentacene decreased to 0.010 ms. This indicates that after pentacene layering, the lifetime of the thin films significantly shortened, which is a typical result of the Dexter energy transfer (DET) phenomenon. In addition to energy transfer, the charge transfer mechanism may also contribute to the differences in device performance between DPS and BTDA, with the CTE of DPS being 34.6%. In comparison, BTDA's CTE reaches 87.7%, indicating that BTDA exhibits a more efficient charge transfer effect, whereas this effect is weaker in DPS.

To verify the RTP behavior of the materials, phosphorescence decay experiments were conducted at 70 °C, and the phosphorescence lifetime histograms are shown in **Figure 2.7e**, with measurement data presented in **Figure 2.8b** and **Table 2.3**. Typically, the lifetime of RTP materials shortens significantly at high temperatures, primarily due to the enhanced nonradiative decay processes at elevated temperatures. As the temperature increases, molecular vibrations and internal motions increase, causing the molecular energy to be rapidly released as thermal energy, leading to a reduction in phosphorescence lifetime. Additionally, intermolecular interactions become unstable at high temperatures, affecting energy transfer efficiency.[97] DPS and BTDA exhibit a significant decrease in lifetime at high temperatures, with the RTP effect substantially weakened, confirming typical RTP material behavior.

The materials' excited state energy levels, including the S_1 and T_1, were summarized and considered to explore the mechanism between RTP materials and the semiconductor layer. The excited state energy levels of DPS and BTDA are determined from their fluorescence and phosphorescence emission spectra. In contrast, the energy levels of pentacene are obtained from relevant literature[98, 99], as shown in **Figure 2.7f**. As shown in the figure, compared to DPS, BTDA has a lower T_1 energy level and a larger ΔE_{st} (S_1−T_1), which is consistent with the smaller bandgap of BTDA. BTDA’s T_1 energy level is closer to that of pentacene than DPS, suggesting that more efficient DET or charge

doi:10.6342/NTU202503178

transfer behavior could occur between BTDA and pentacene. DET is a short-range energy transfer mechanism driven by strong intermolecular exchange interactions, facilitating energy transfer between triplet excitons. When the acceptor materials, DPS or BTDA, are close to the donor material, pentacene, with a distance of approximately 1–2 nm, energy transfer becomes more efficient, allowing triplet excitons to transfer to pentacene via intermolecular exchange[100], thereby increasing the triplet exciton density within pentacene. However, due to the singlet fission effect with the $2T_1 < S_1$ energy relationship in pentacene, the efficiency of triplet fusion remains low despite generating many triplet excitons[101, 102]. Consequently, the triplet excitons are more likely to convert into charges under an applied voltage, enhancing the photoresponsive capability. This effect will be further elucidated in the subsequent device characteristics section.

2.3.5 Device Performance of the Transistor Memory

After analyzing the optical properties, bottom-gate/top-contact (BG/TC) transistor memory devices based on these materials were fabricated to investigate their memory effects. The device structure is illustrated in **Figure 2.3a**. The transfer characteristics of the devices measured at room temperature are presented in **Figure 2.9**. The devices were characterized by sweeping the gate voltage (V_g) from 30 to −60 V under a fixed drain voltage (V_d) of −40 V. The average hole mobilities (μ_{avg}) and threshold voltages (V_{th}) in the saturation regime were determined by using the following equation

$$I_d = \mu_{avg} \frac{W}{2L} C_{areal} (V_g - V_{th})^2 \tag{4}$$

where C_{areal} represents the areal capacitance of the 100 nm SiO_2 dielectric layer of 31.5 nF cm^{-2}. The μ_{avg} of DPS/PS, DPS-C/PS, BTDA/PS, and BTDA-C/PS devices were 0.012, 0.011, 0.021, and 0.010 cm^2 V^{-1}s^{-1}, respectively. When a bias of $V_g = -50$ V was applied

doi:10.6342/NTU202503178

for 1 s during the electrical erasing process, the threshold voltages ($V_{\mathrm{th,\ erase}}$) presented a negative shift, switching the device to the OFF state. For photo-assisted electrical writing, a 265 nm light (285 mW cm^{-2}) was used, and the V_{g} was set to 0, 10, 20, and 30 V for 10 s, respectively, under a V_{d} of −40V. The result shows that the threshold voltages ($V_{\mathrm{th,\ write}}$) shifted positively, suggesting the electron-trapping capability and switching the device to the ON state. Furthermore, the memory windows (ΔV_{th}) are defined as $\Delta V_{\mathrm{th}} = V_{\mathrm{th,\ write}} - V_{\mathrm{th,\ erase}}$. When 265 nm-light illuminates along with $V_{\mathrm{g}} = 30$ V, the device exhibits a maximum ΔV_{th}. For DPS/PS, DPS-C/PS, BTDA/PS, and BTDA-C/PS, the values of ($V_{\mathrm{th,\ erase}}$, $V_{\mathrm{th,\ write}}$, ΔV_{th}) under $V_{\mathrm{g}} = 30$ V are (−15, 24, 39) V, (−12, −12, 0) V, (−14, 27, 41) V, and (−11, −3, 8) V, respectively. The values of ΔV_{th} are summarized in **Table 2.4**. As shown in **Table 2.4** and **Figure 2.9**, DPS/PS and BTDA/PS exhibit larger threshold voltage shifts, indicating a significantly expanded memory window after writing. This indicates their enhanced ability to capture and retain charge, leading to more effective memory behavior. Furthermore, subthreshold swing (SS) is a critical parameter for evaluating the power consumption and material properties of thin-film transistors (TFTs). A lower SS value indicates a more rapid and sensitive response of the drain current to V_{g} variations in the subthreshold region. This low SS behavior can be attributed to a fully depleted channel and minimal interface defects, enabling faster and more efficient device operation. [25, 103] The lower *SS* values observed in DPS/PS and BTDA/PS suggest faster device switching and higher charge transport efficiency. These characteristics not only enhance memory performance but also contribute to the overall stability of the device.

Additionally, it is worth noting that the illumination conditions at 265 nm light do not cause severe bond cleavage or changes in the chemical structure of the organic materials. As shown in the Fourier-transform infrared spectrometer (FTIR) results in **Figure 2.10**, there are no significant differences in the FTIR spectra of the organic materials between the original samples and those exposed to 265-nm light for a time duration of 60 seconds under air. In addition, all device measurements were conducted in a nitrogen environment to preclude the potential oxidization during light exposure. Next, the measurement of hysteresis characteristics are shown in **Figure 2.11**. The DPS/PS and BTDA/PS exhibit a significant hysteresis effect during the forward and reverse scanning process. Specifically, there is a notable difference in the drain current during the forward and reverse scans, indicating that these two transistor memory devices possess a strong memory effect. In contrast, the forward and reverse scanning curves of the DPS-C/PS and BTDA-C/PS are very close, showing a less pronounced hysteresis effect, suggesting a weaker memory effect in these two transistor memories. The gate leakage current, as shown in **Figure 2.12**, remains at approximately 10^{-12} to 10^{-13} A for DPS/PS, DPS-C/PS, BTDA/PS, and BTDA-C/PS across the entire gate voltage range. The minimal gate leakage current indicates that these organic transistors exhibit excellent insulation properties, ensuring that the stability of the devices is not significantly affected by leakage currents.

After investigating the typical p-type transfer performance, the photoresponse and memory stability were characterized using transient curves, shown in **Figure 2.13a–d**. Among them, the DPS/PS and BTDA/PS devices, which exhibit RTP effects, demonstrated exceptional memory ratios ($I_{\mathrm{ON}}/I_{\mathrm{OFF}}$) under photo-assisted electrical writing at 265 nm (285 mW cm^{-2}) and $V_{\mathrm{g}} = 30$ V. The DPS/PS device achieved a memory ratio of approximately 10^5, while the BTDA/PS device reached a superior value of approximately 10^6. The parameters of the transfer and transient curves of the devices are summarized in **Table 2.4**. In correlation with the previously discussed optical behavior, devices based on dianhydride molecules with RTP properties exhibited outstanding memory performance owing to the long exciton lifetime and their DET interaction with

doi:10.6342/NTU202503178

pentacene. To verify the substantial reduction of the RTP effect under high-temperature conditions, transfer and transient curves of the DPS/PS and BTDA/PS devices, which exhibit a decline in memory behavior, were measured at 70°C. The results are shown in **Figure 2.14** and coincide with the time-resolved optical analysis at 70 ºC.

Given that the BTDA/PS device demonstrated the highest memory stability, the device was utilized to gain further insight into the charge-trapping capability against varying device operations for optimization. **Figure 2.15a** presents the same photo-assisted electrical writing mode as those mentioned above, but varying V_d from −5 to −40 V. At $V_\mathrm{d} = -10$ V, the $I_\mathrm{ON}/I_\mathrm{OFF}$ reaches approximately 10^6. Additionally, **Figure 2.15b** illustrates the effect of different illumination times from 1 to 100 s on current stability in the photo-assisted electrical writing process, with an $I_\mathrm{ON}/I_\mathrm{OFF}$ close to 10^6 after 5 s of illumination. The results indicate that the device based on BTDA presents superior memory behavior even under lower operating voltage and shorter illumination periods, underscoring the energy efficiency of the RTP property. The long-term stability and durability are crucial factors for modern optoelectronic devices. Therefore, the retention test of the BTDA/PS device is shown in **Figure 2.15c**. The ON state was measured after photo-assisted electrical writing (265 nm; 285 mW cm^{-2}; $V_\mathrm{g} = 30$ V) for 10 s, and the OFF state was conducted after electrical erasing at $V_\mathrm{g} = -50$ V for 1 s. Over a 10,000 s stability test, the $I_\mathrm{ON}/I_\mathrm{OFF}$ remained at approximately 10^6. The write−read−erase−read (WRER) measurement was carried out to evaluate the endurance of the RTP transistor memory (**Figure 2.15d)**. The "write" step corresponds to the ON state achieved by photo-assisted electrical writing (265 nm; 285 mW cm^{-2}; $V_\mathrm{g} = 30$ V) for 10 s at $V_\mathrm{d} = -40$ V, the "read" step involves measurement of the state at $V_\mathrm{d} = -40$ V and $V_\mathrm{g} = 0$ V, and the "erase" step is the OFF state after electrical erasing at $V_\mathrm{g} = -50$ V for 5 s. The BTDA/PS device maintains an $I_\mathrm{ON}/I_\mathrm{OFF}$ of 10^6 after 20 cycles of the WRER test. As can be seen, BTDA/PS

doi:10.6342/NTU202503178

is a highly stable and durable memory device, ensuring reliable performance over time. The long-term stability and durability tests of the DPS/PS device are presented in **Figure 2.16**, respectively. The results suggest that the device with RTP property in the DPS/PS system also presents an outstanding $I_{\mathrm{ON}}/I_{\mathrm{OFF}}$ of 10^5 and remarkable durability after 20 cycles, highlighting the feasibility and potential of RTP materials in optoelectronic applications.

To further clarify the impact of DET phenomenon and singlet fission on memory characteristics, a comparative experiment was conducted by replacing the semiconductor layer from pentacene to dinaphtho[2,3-b:2',3'-f]thieno[3,2-b]thiophene (DNTT), as shown in **Figure 2.17**. DNTT is a well-known p-type channel in TFTs. However, a significant decline in memory performance was observed when DNTT was used as the semiconductor layer. This can be attributed to the fact that, compared to pentacene, DNTT exhibits a much weaker singlet fission effect, thereby reducing the probability of triplet excitons transferring to the semiconductor layer via DET. This result further confirms that when pentacene is employed as the semiconductor channel, triplet excitons effectively enhance memory performance and photoresponse capability through intermolecular energy transfer and the singlet fission mechanism. This finding highlights the superior suitability of pentacene over DNTT as the active layer material in this study.

To better illustrate the differences among various types of memory devices, **Table 2.5** provides a comparative analysis of their writing mechanisms, erasing processes, and performance metrics.[93,96,104,105] This comparison highlights the distinct advantages of room-temperature phosphorescence-based transistor memories, particularly the photo-assisted electrical writing technique demonstrated in this study. Compared to purely electrically written resistive memory devices, this approach achieves a higher $I_{\mathrm{ON}}/I_{\mathrm{OFF}}$ and enhanced operational stability, offering a promising direction for next-generation memory applications.

2.3.6 Synaptic Characteristics of RTP-Based Device

In the human brain, memory storage and processing are structured hierarchically, consisting of sensory memory, short-term memory (STM), and long-term memory (LTM). Sensory memory temporarily retains sensory input for durations ranging from milliseconds to seconds, and the information is easily lost if not further processed. However, once brought into human consciousness, sensory memory can be converted into STM, which persists for several seconds to minutes. In addition, with rehearsal and repeated learning, STM can be consolidated into LTM, ensuring stable retention[106, 107], as depicted in **Figure 2.18a**. It is worth noting that around 80% of external information is processed through the visual perception system.[108] Thus, the connection between the human brain and the visual system is essential for developing neural networks. Here, the BTDA/PS system with RTP effects simulates the learning behavior in the human brain and provides a foundation for the development of artificial neural systems. In a photosynaptic transistor, the PPF ratio is used to quantify the enhancement of synaptic strength caused by applying two consecutive pulses with an interval (Δt) in between. The amplitude of excitatory postsynaptic current (EPSC) induced by the first optical pulse stimulation is denoted as A_1, and A_2 represents the amplitude caused by the second optical pulse under identical conditions after some time of Δt, as illustrated in **Figure 2.18b**. As an essential indicator of STP, PPF is defined by the following equation:

$$\mathrm{PPF} = \frac{A_2}{A_1} \times 100\% \tag{5}$$

The relationship between the PPF ratio of the BTDA/PS photosynaptic transistor and Δt is shown in **Figure 2.18c**. Measurements are conducted at pulse intervals ranging from

50 ms to 2 s under 265-nm light illumination (1.7 mW cm^{-2}) with $V_d = -10$ V and $V_g = 0$ V. As Δt increases, the PPF ratio exhibits an exponential decay. Notably, BTDA/PS achieves a high PPF ratio of 1.92 at $\Delta t = 50$ ms. The PPF ratios of DPS/PS, DPS-C/PS, and BTDA-C/PS are presented in **Figure 2.19**, where DPS/PS and BTDA/PS exhibit significantly higher PPF ratios compared to DPS-C/PS and BTDA-C/PS. This observation suggests that the RTP effect and DET phenomenon enable DPS/PS and BTDA/PS to respond more rapidly. Among them, BTDA/PS demonstrates the strongest photoresponse, corresponding to its highest PPF ratio, highlighting its excellent photosynaptic performance. The effects of varying key parameters were systematically investigated to elucidate the transition from STP to LTP further. Specifically, the influence of pulse numbers (50 to 200 pulses, SNDP), pulse width (100 ms to 30 s, STDP), pulse rate (4 to 6.7 Hz, SRDP), and pulse intensity (160 to 230 mW cm^{-2}, SIDP) are demonstrated in **Figures 2.18d−g**, respectively. The results demonstrate that the BTDA/PS photosynaptic transistor exhibits good synaptic plasticity. For instance, as the pulse number increases, the EPSC gradually increases, indicating the transition from STP to LTP, with repeated stimulation leading to memory enhancement from STM to LTM. The DPS/PS and BTDA/PS memory devices exhibit excellent performance due to their intrinsic RTP effect and DET phenomenon, which enable efficient charge trapping and release. Notably, the BTDA/PS system demonstrates the highest PPF ratio due to the optimized structure for charge modulation. This improvement can be attributed to better charge modulation. A high external quantum efficiency (EQE) and a short exciton lifetime benefit high photocurrent and photoresponse in phototransistors.[109] However, the transformation of photoexcitation to the trapped charges contributes to the current modulation in synaptic phototransistors and memory.[110] This effect will give rise to different *SS* and V_{th} values, as shown in **Table 2.4**, and eventually give rise to tunable

doi:10.6342/NTU202503178

short-term to long-term memory behaviors. Therefore, the BTDA/PS system demonstrates the best stability and charge modulation capability by exploiting its long exciton lifetime.

2.3.7 Application of Artificial Photosynapses for Image Recognition System

Based on synaptic devices, ANNs can simultaneously perform data processing and storage, and the increase in the number of hidden layers significantly improves classification accuracy.[111, 112] To further explore the application of BTDA/PS materials in neuromorphic computing, this study simulates image denoising and recognition using handwritten digit images from the Modified National Institute of Standards and Technology (MNIST) database, with all simulations conducted in MATLAB. First, random noise was added to the initial images, with the maximum noise value set to 100%, and the image brightness values were normalized to a range of 0 to 255. Subsequently, a 28 × 28 pixel denoising array was applied, in which the pixel values of the digit contours were composed of the PPF ratios (Δt = 50 ms) based on the BTDA/PS device. This process enhanced the contrast between the digit contours and random noise, improving image clarity and facilitating preprocessing. After denoising, the resulting images were converted to grayscale images as a preprocessed input. To further investigate the noise-reduction ability of the denoising array, a NN with a size of 784 × 256 × 128 × 10 layers is constructed for image recognition. The 784 input neurons correspond to the 28 × 28 pixels from the preprocessed images, and the output neurons correspond to the 10 digits from "0" to "9". The schematic of the NN architecture is shown in **Figure 2.20a**. In this study, 80% of the dataset was used for training, and the remaining 20% was used for

doi:10.6342/NTU202503178

testing to evaluate the recognition performance. The images without denoising (n = 0) and the two-time denoised images (n = 2) are presented in **Figure 2.20b**. The images processed through one denoising array (n = 1) are presented in **Figure 2.21**. It can be observed that the noise in the images was reduced, and the denoised images have restored the general contours of the original numbers. Additionally, as the number of learning epochs increases, the accuracy gradually improves and stabilizes, as shown in **Figure 2.20c**. The curve for n = 0 shows an accuracy of only 60% after 100 learning epochs, indicating poor image recognition capability. In contrast, the curve for n = 1 demonstrates a significant improvement, achieving an accuracy of 81%. Notably, the curve for n = 2 ultimately reaches the highest accuracy of ~90% after 100 learning epochs, showcasing its excellent denoising capability.

2.4 Summary

This study leverages the exceptional RTP performance of DPS and BTDA, combined with PS, to investigate their structural characteristics and realize high-performance memory and photosynaptic devices. Structurally, the superior RTP properties of DPS and BTDA arise from multiple intermolecular interactions, including n C=O···C(C=O) Van der Waals forces, π–π stacking, and dipole–π interactions. These interactions suppress molecular rotation and vibration effectively, enhancing molecular rigidity and contributing to extended triplet exciton lifetimes. Upon structural transformation into diimide groups (DPS-C and BTDA-C), molecular rigidity is reduced, and RTP characteristics are lost, highlighting the critical role of dianhydride groups in RTP performance. Regarding device performance, under ultraviolet light-assisted programming at 265 nm, DPS and BTDA achieved memory ratios of approximately 10^5

and 10^6, respectively, demonstrating stable memory retention for up to 10,000 seconds and durability over 20 operational cycles. For photosynaptic applications, BTDA exhibited an outstanding PPF ratio of 1.92 under a Δt = 50 ms, indicating excellent photoresponse capabilities and persistent memory behavior. Additionally, after 100 learning epochs and processing through two denoising arrays, BTDA achieved a significantly improved image recognition accuracy of 88.3%, further underscoring its potential for ANN applications. In summary, this study elucidates the structural advantages and RTP properties of DPS and BTDA while validating their application potential in memory and artificial photosynapses. These findings provide valuable insights for the development of next-generation high-performance optoelectronic devices.

doi:10.6342/NTU202503178

2.5 Tables and Figures

Table 2.1 The RTP lifetime decay profiles of the powdered materials are analyzed using a bi-exponential fitting model.

	A_1 (%)	τ_1 (ms)	A_2 (%)	τ_2 (ms)	τ_{avg} (ms)
DPS	0.604	0.271	0.396	2.951	2.622
DPS-C	0.854	0.199	0.146	2.012	1.350
BTDA	0.528	3.378	0.472	1.058	2.870
BTDA-C	0.689	0.426	0.311	1.749	1.285

Table 2.2 The RTP lifetime decay profiles of the DPS and BTDA films and their respective bilayers with pentacene are analyzed using a bi-exponential fitting model.

	A_1 (%)	τ_1 (ms)	A_2 (%)	τ_2 (ms)	τ_{avg} (ms)
DPS	0.950	0.001	0.050	0.042	0.026
DPS/pentacene	0.945	0.001	0.055	0.029	0.017
BTDA	0.939	0.002	0.061	0.101	0.081
BTDA/pentacene	0.942	0.001	0.058	0.020	0.010

doi:10.6342/NTU202503178

Table 2.3 The phosphorescence lifetime decay profiles of the DPS and BTDA films and their respective bilayers with pentacene were analyzed at 70°C using a bi-exponential fitting model.

Item	A_1 **(%)**	τ_1 **(ms)**	A_2 **(%)**	τ_2 **(ms)**	τ_{avg} **(ms)**
DPS	0.501	0.002	0.499	0.002	0.002
DPS/pentacene	0.500	0.001	0.500	0.001	0.001
BTDA	0.504	0.002	0.496	0.002	0.002
BTDA/pentacene	0.500	0.001	0.500	0.001	0.001

doi:10.6342/NTU202503178

Table 2.4 Summary of the transistor memory performance parameters focusing on the memory window and ratio at different biases during the photo-assisted writing.

Item	V_g (V)	$V_{th,\ write}$[a] (V)	$V_{th,\ erase}$[a] (V)	ΔV_{th}[b] (V)	I_{ON}/I_{OFF}[c]
DPS/PS	0	3	−15	18	1.5×10^3
	10	10		25	5.2×10^4
	20	18		33	3.4×10^5
	30	24		39	7.1×10^5
DPS-C/PS	0	−12	−12	0	−
	10	−12		0	−
	20	−12		0	−
	30	−12		0	−
BTDA/PS	0	5	−14	19	2.8×10^3
	10	12		26	1.5×10^5
	20	22		36	2.0×10^6
	30	27		41	2.9×10^6
BTDA-C/PS	0	−5	−11	6	4.4
	10	−4		7	5.2
	20	−3		8	9.3
	30	−3		8	23.0

[a] Threshold voltage in the write (ON) or erase (OFF) states of a memory device.

[b] Memory windows (ΔV_{th}) are defined as $\Delta V_{th} = V_{th,\ write} - V_{th,\ erase}$.

[c] The memory ratio refers to the current difference between the ON and OFF states at $V_d = -40$ V

Table 2.5 Comparison of different memory devices based on their writing and erasing processes, excitation wavelength, light intensity, and I_{ON}/I_{OFF}. The devices include phosphorescent-type photomemory, electrical-type transistor memory, and organic memristors.

Devices structure	**Writing process**	**Erasing process**	**λ (nm)**	**Light Intensity ($mWcm^{-2}$)**	**I_{ON}/I_{OFF}**	**Ref.**
Si/SiO_2/BTDA/PS/ pentacene/Au [a)]	Photo-assisted electrical writing (10 s, V_g = 30 V)	Electrical erasing (1 s, V_g = -50 V)	265	285	~ 10^6	This study
Si/SiO_2/PS-b-P4VP/ $Ir(bt)_2(acac)$/ pentacene/Au [b)]	Photo writing (10 s)	Electrical erasing (5 s, V_g = -60 V)	525	742.58	~ 10^3	[93]
Si/SiO_2/TIPS-3/PS/ pentacene/Au [c)]	Photo writing (10 s)	Electrical erasing (1 s, V_g = -60 V)	450	5	~ 10^5	[96]
Si/SiO_2/Al/AlO_x/ 12DA9ND10-PA/ pentacene/Au [d)]	Electrical writing (18 s, V_g = –5 V)	Electrical erasing (18 s, V_g = +5 V)	–	–	~ 10^3	[109]
ITO/MH-*b*-PI /Al [e)]: WORM (Vertical Cylinders)	V_{ser} = –1.4 V	–	–	–	~ 10^5	[110]
ITO/MH-*b*-PI /Al [e)]: Flash Memory (Horizontal Cylinders)	V_{ser} = –1.7 V	V_{reser} = 3 V	–	–	~ 10^2	

DRAM (Spherical Nanostructure)	$V_{\mathrm{ser}} = -1.5$ V	Power-off dependent	–	–	~ 10^5

[a] This study presents an RTP transistor memory that utilizes photo-assisted electrical writing.

[b] A room-temperature phosphorescence-based transistor memory that employs pure photo writing. $Ir(bt)_2(acac)$: bis(2-benzo[b]thiophen-2-ylpyridine)(acetylacetonate)iridium(III), and PS-*b*-P4VP: polystyrene-*b*-poly(4-vinylpyridine).

[c] A photo writing transistor memory that does not exhibit RTP. TIPS-3: 9,10-bis[(triisopropylsilyl)ethynyl]anthracene.

[d] A purely electrical writing transistor memory that does not exhibit RTP. DA: diacetylenic, ND: naphthalenetetracarboxyldiimide, and PA: phosphonic acids.

[e] Purely electrical writing resistive memory devices that do not exhibit RTP. MH-*b*-PI: carbohydrate-*block*-polyisoprene, WORM: write-once-read-many-times, and DRAM: dynamic-random-access-memory.

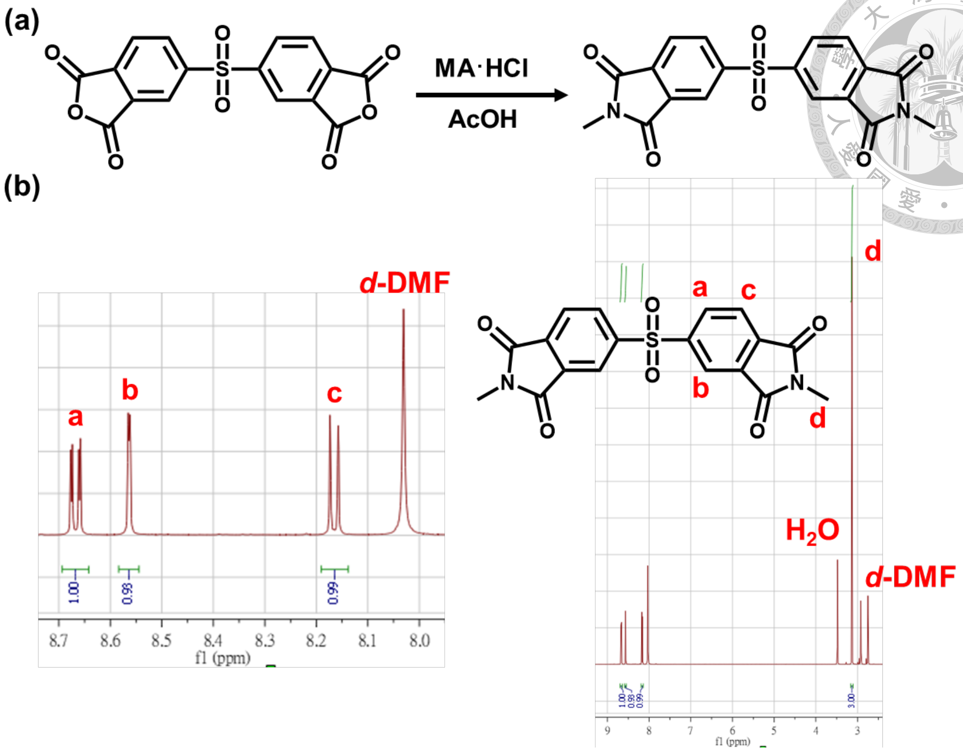

Figure 2.1 (a) The synthetic route for DPS-C. (b) 1H NMR spectrum of DPS-C in d-DMF.

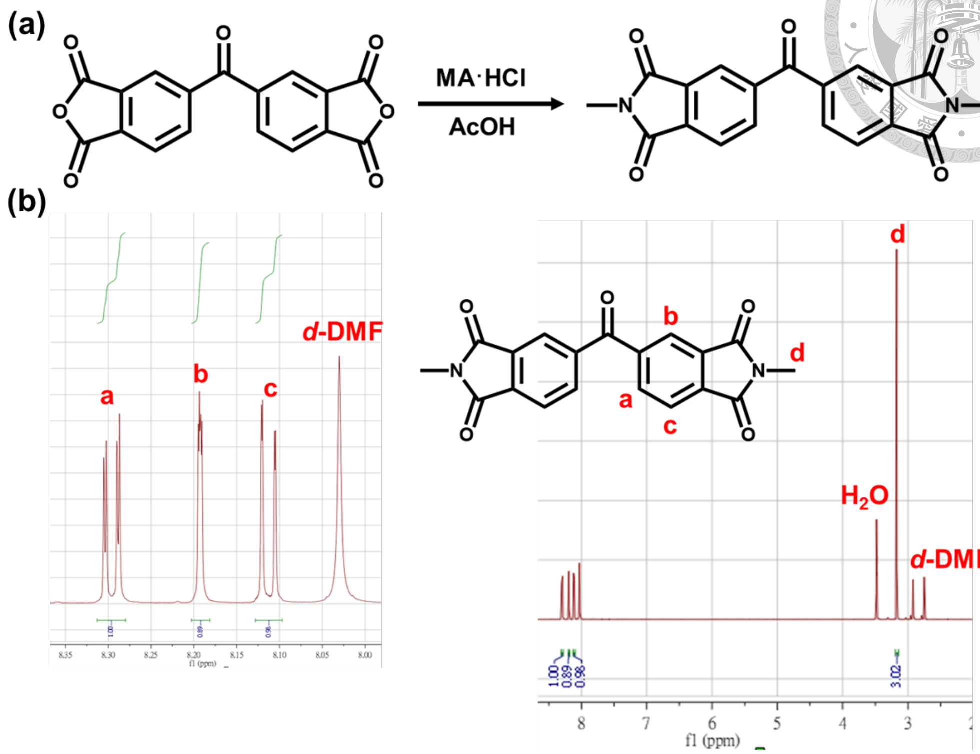

Figure 2.2 (a) The synthetic route for BTDA-C. (b) ^{1}H NMR spectrum of BTDA-C in *d*-DMF.

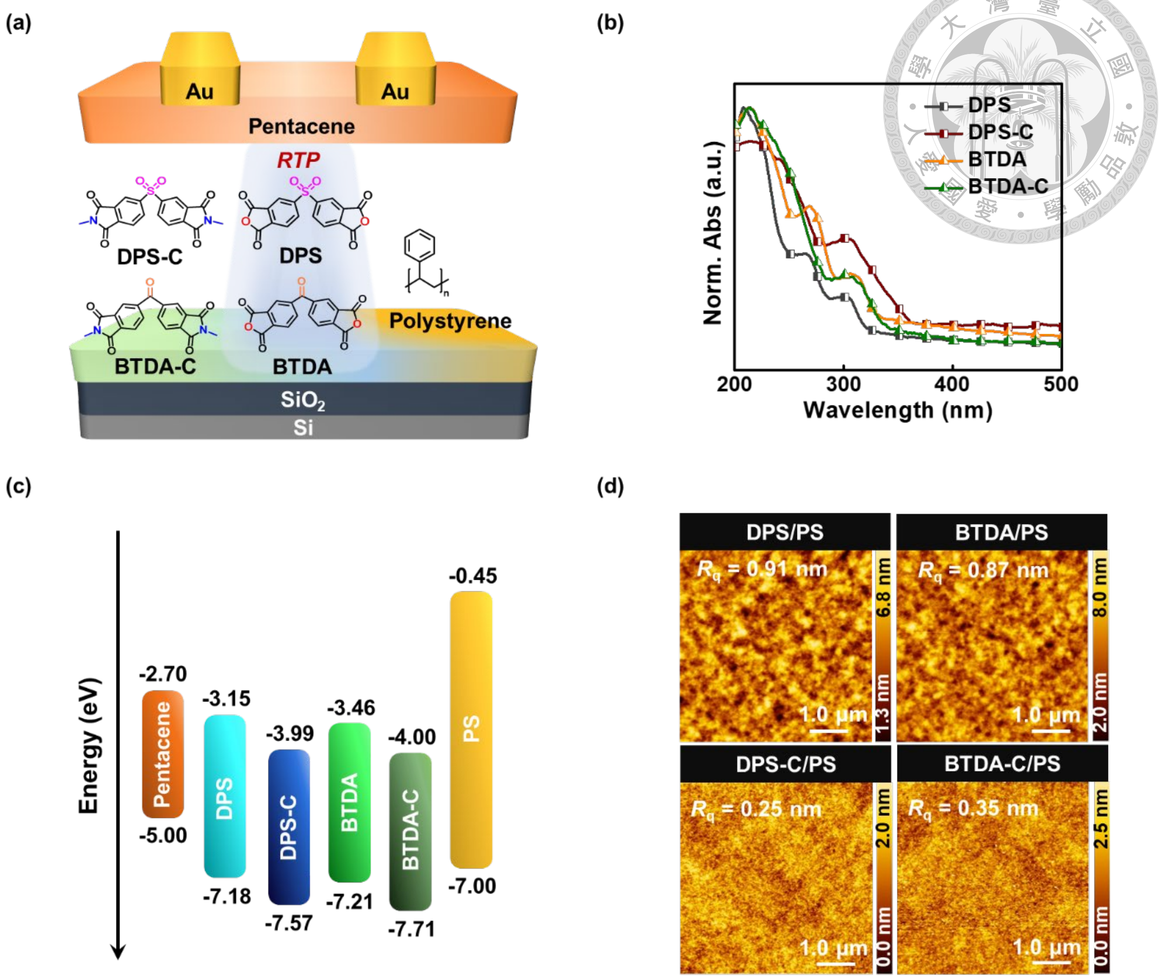

Figure 2.3 (a) Device configuration of the photomemory and photosynaptic transistors and the chemical structures of the organic RTP materials and their imide-structured references. (b) UV-vis absorption spectrum of DPS, DPS-C, BTDA, and BTDA-C films. (c) Energy levels diagram of the studied materials. (d) AFM height images of the floating gate DPS/PS, DPS-C/PS, BTDA/PS, and BTDA-C/PS thin films.

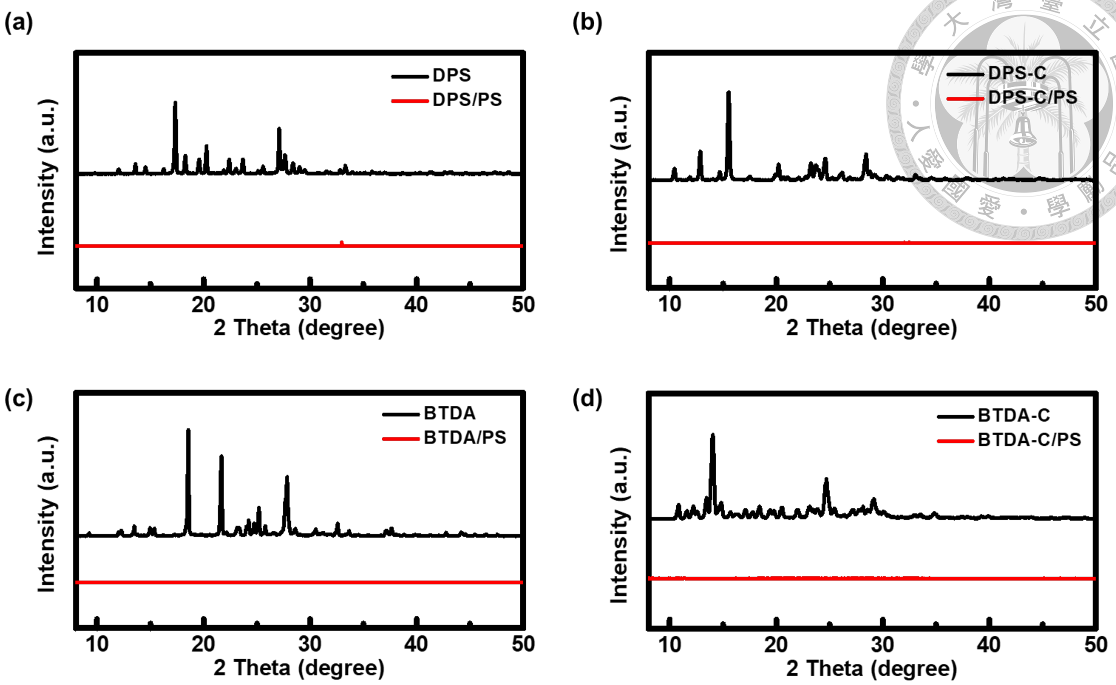

Figure 2.4 XRD measurements of the bulk organic material powders and their mixture with PS in the drop-cast films.

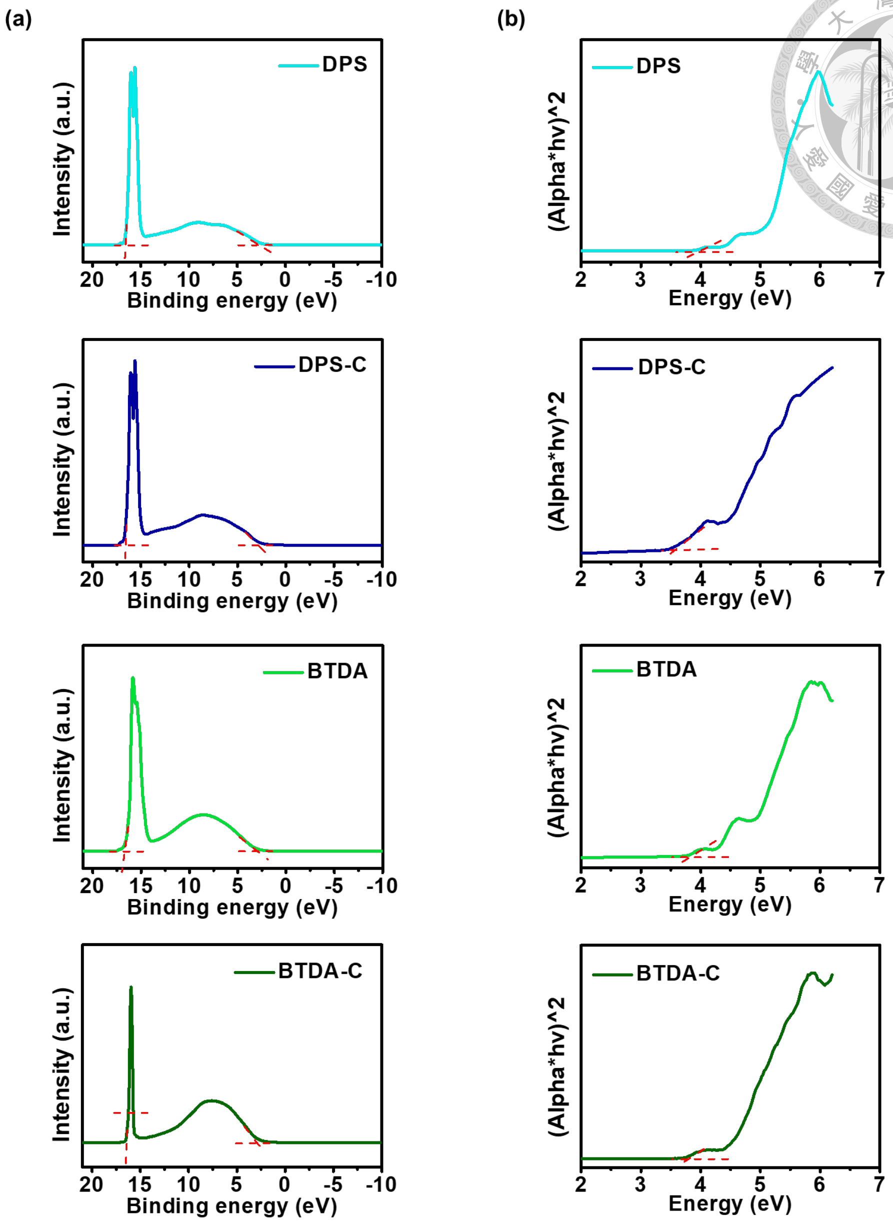

Figure 2.5 (a) UPS and (b) tau plot of the UV-vis absorption spectra of DPS, DPS-C, BTDA, and BTDA-C. The red dashed lines indicate the fitting onset values for calculating the energy levels of these materials.

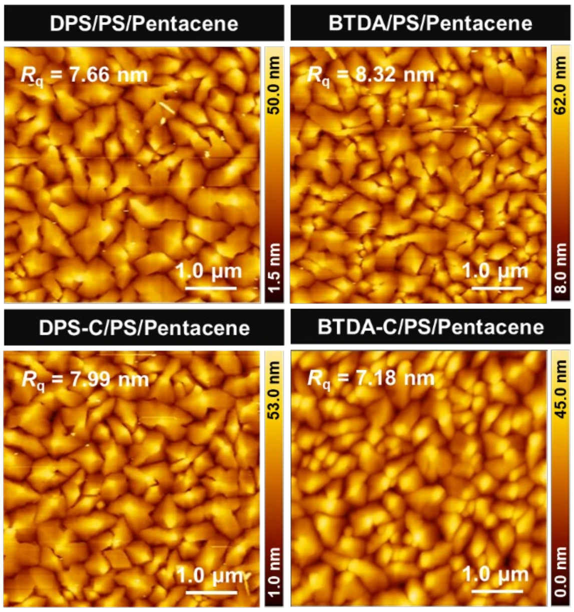

Figure 2.6 AFM height images of the floating gate with pentacene semiconductor DPS/PS/pentacene, DPS-C/PS/pentacene, BTDA/PS/pentacene, and BTDA-C/PS/pentacene.

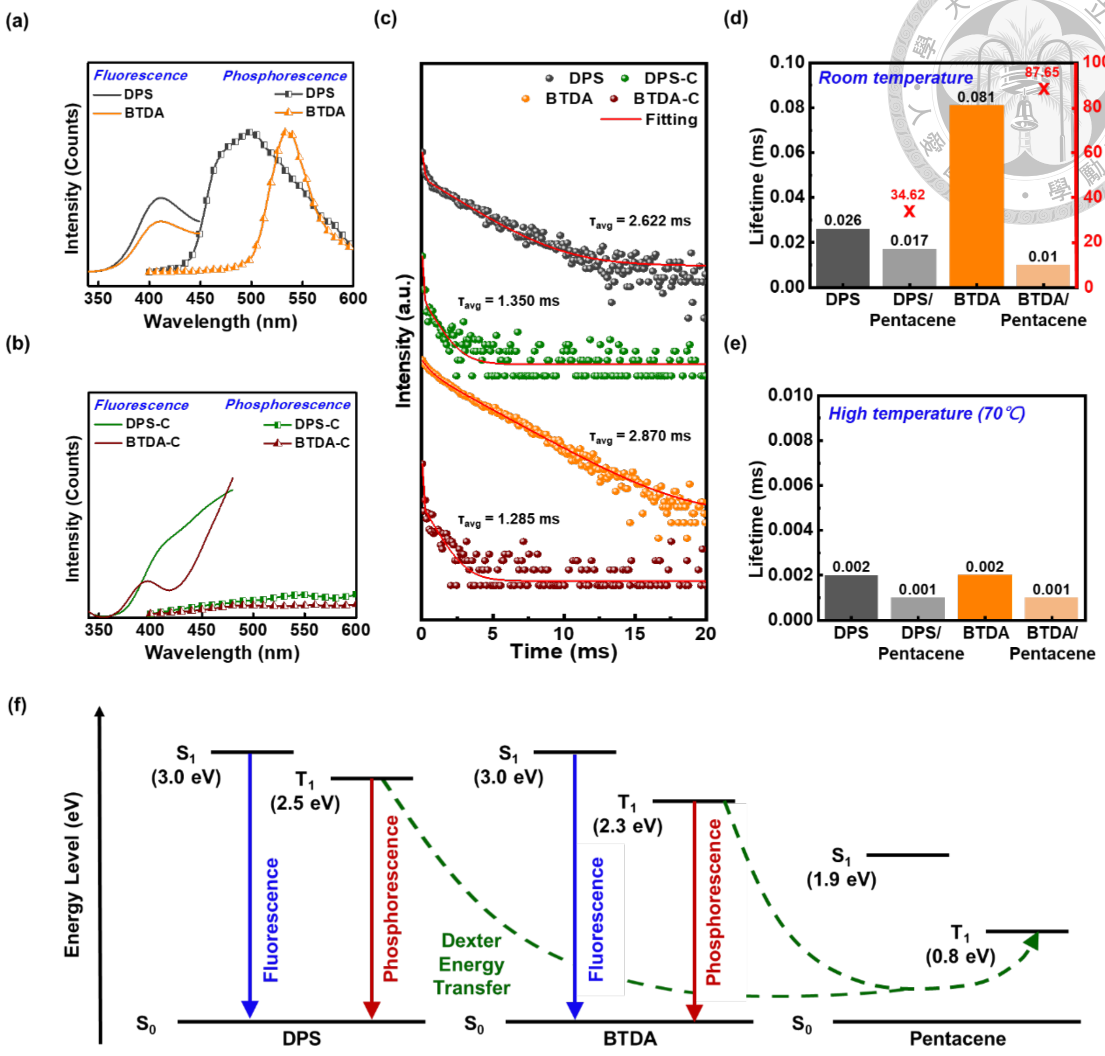

Figure 2.7 Photoluminescence and phosphorescence emission spectra of (a) dianhydride derivatives (DPS, BTDA) and (b) diimide derivatives (DPS-C, BTDA-C) excited at 290 nm at room temperature. (c) Lifetime decay profiles of phosphorescence emission for powder samples excited at 290 nm at room temperature. (d) Phosphorescence lifetime bar chart and CTE for thin film samples, including the DPS and BTDA films and their respective bilayers with pentacene, excited at 290 nm at 25 °C. (e) Phosphorescence lifetime bar chart for thin film samples, the DPS and BTDA films, and their respective bilayers with pentacene, excited at 290 nm at 70 °C. (f) Schematic illustration of the fluorescence, phosphorescence, and DET mechanism of the RTP materials DPS and BTDA with pentacene.

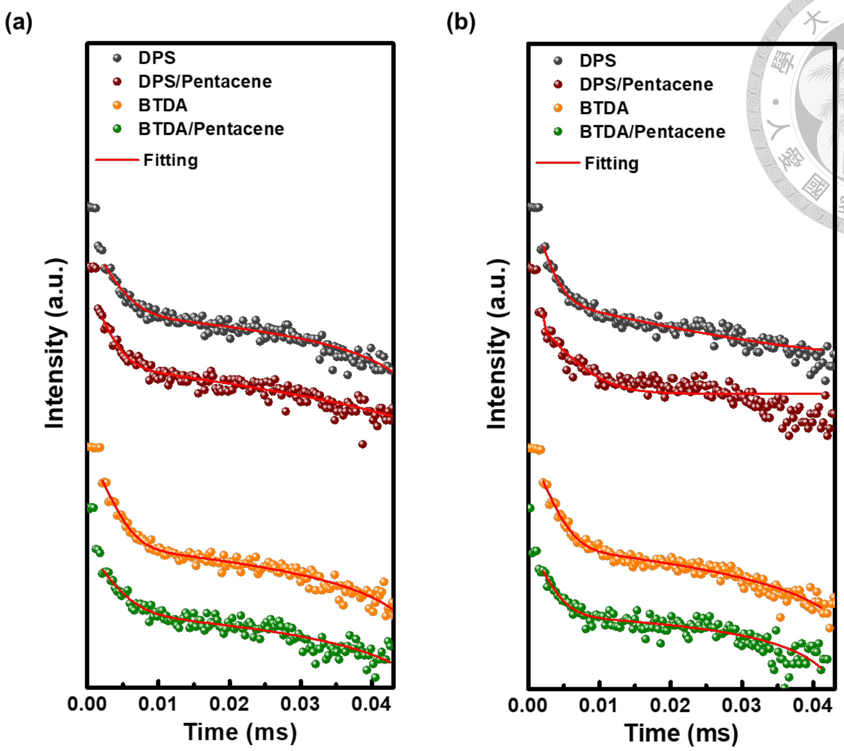

Figure 2.8 Lifetime decay profiles of phosphorescence emission of the DPS and BTDA films and their respective bilayers with pentacene excited at 290 nm (a) at room temperature and (b) at 70°C.

doi:10.6342/NTU202503178

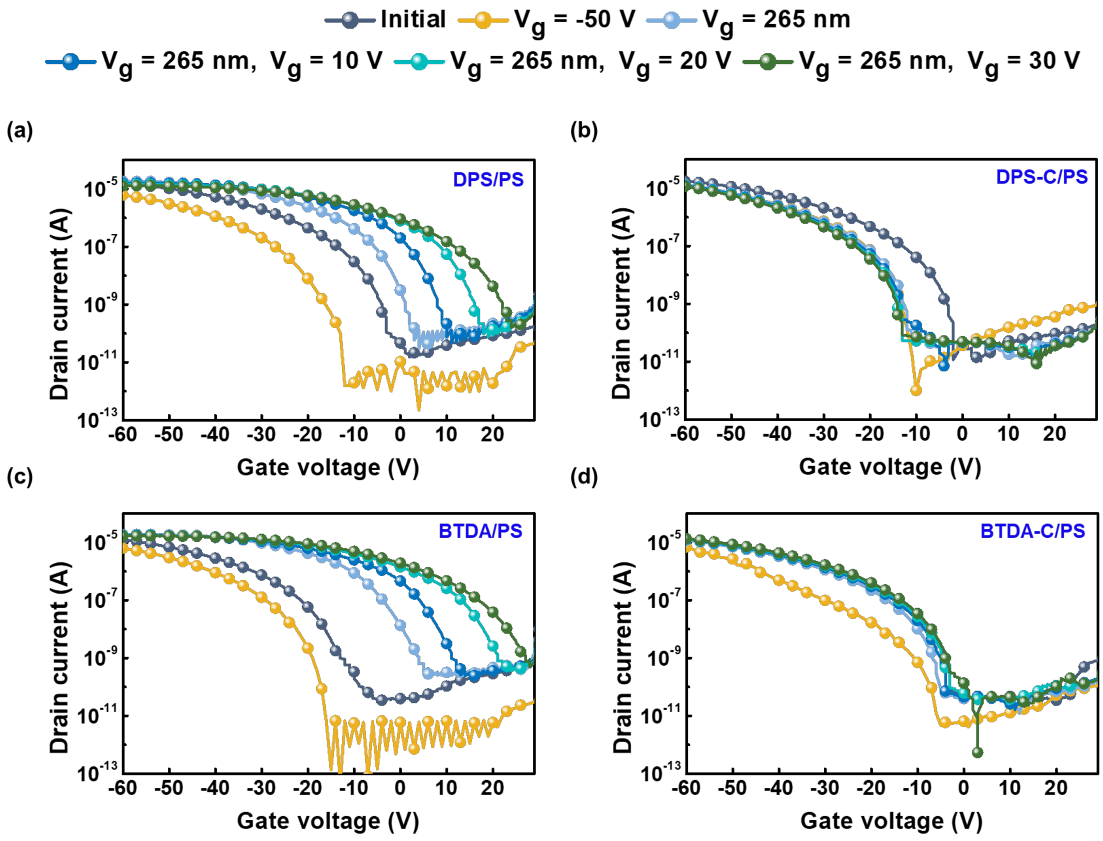

Figure 2.9 The transfer characteristics of the transistor memory device (a) DPS/PS, (b) DPS-C/PS, (c) BTDA/PS, and (d) BTDA-C/PS as the floating gate dielectrics at $V_d = -40$ V. The measurements involved photo-assisted electrical writing (265 nm, 285 mW cm^{-2}; $V_g = 0$, 10, 20, and 30 V) for 10 s or electrical erasing at $V_g = -50$ V for 1 s. The devices were measured at 25 °C and in a nitrogen environment.

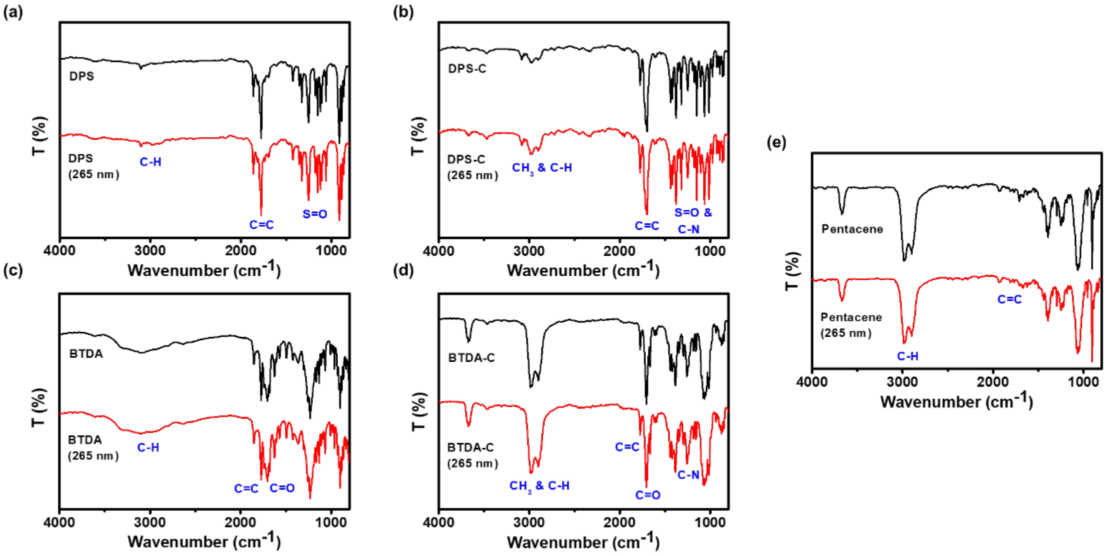

Figure 2.10 FTIR spectra of the organic materials (a) DPS, (b) DPS-C, (c) BTDA, (d) BTDA-C/PS, and (e) pentacene, showing both the original samples and those exposed to 265-nm light (285 mW cm^{-2}) for 60 seconds under air.

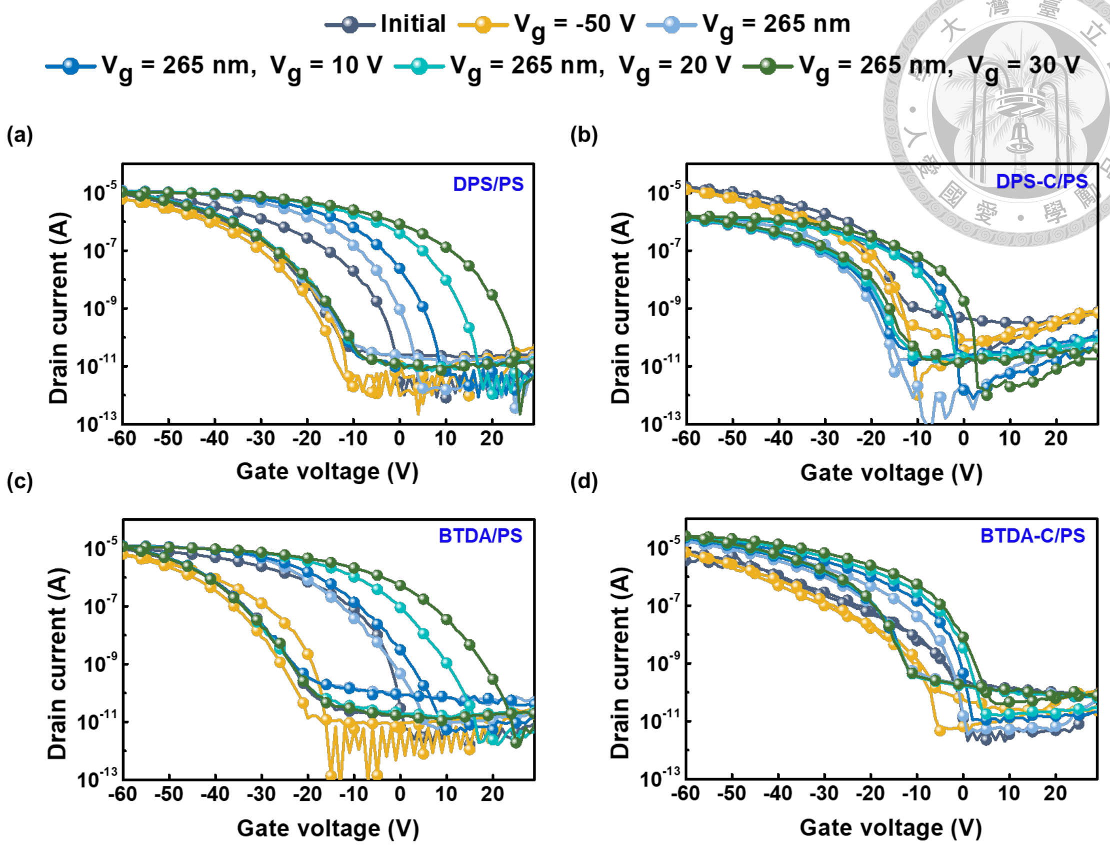

Figure 2.11 The hysteresis characteristics of the transistor memory device (a) DPS/PS, (b) DPS-C/PS, (c) BTDA/PS, and (d) BTDA-C/PS as the floating gate dielectrics at V_d = −40 V. The measurements involved photo-assisted electrical writing (265 nm, 285 mW cm^{-2}; V_g = 0, 10, 20, and 30 V) for 10 s or electrical erasing at V_g = −50 V for 1 s. The devices were measured at 25 °C and in a nitrogen environment.

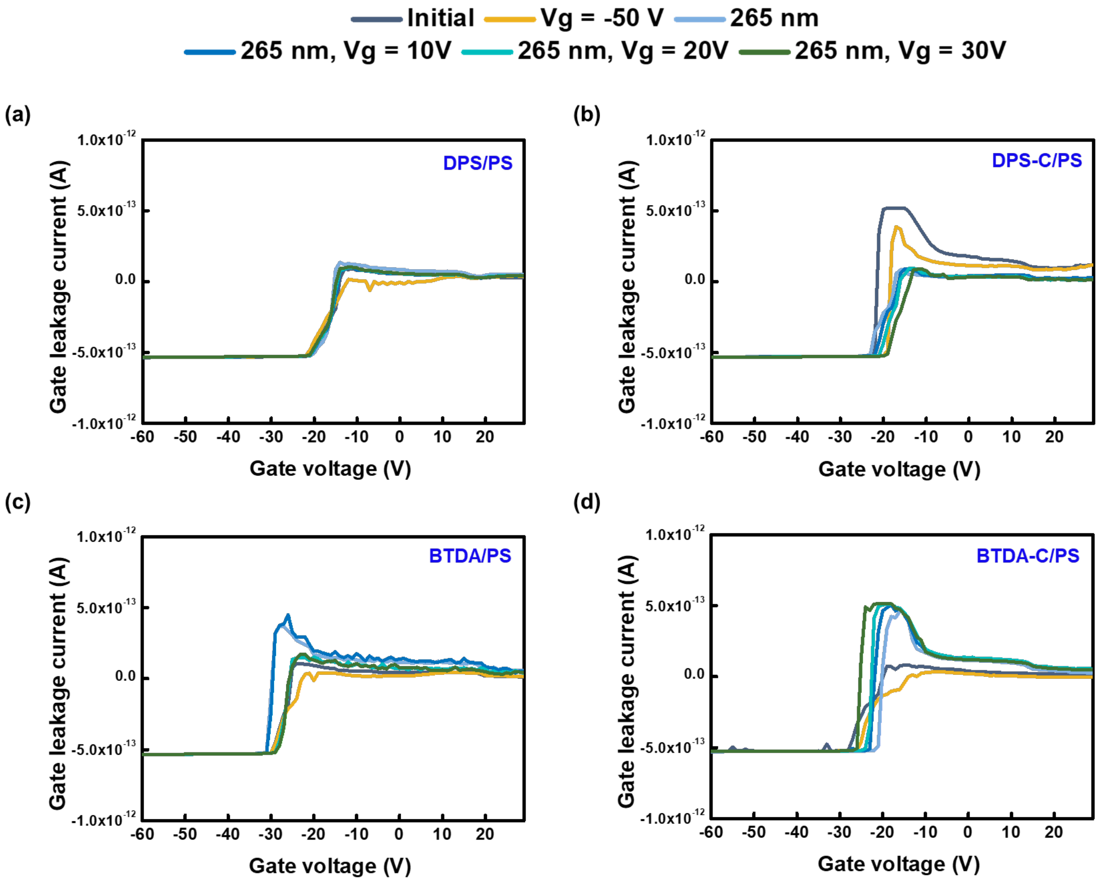

Figure 2.12 The gate leakage current of the transistor memory device (a) DPS/PS, (b) DPS-C/PS, (c) BTDA/PS, and (d) BTDA-C/PS as the floating gate dielectrics are characterized by sweeping the gate voltage (V_g) from 30 to −60 V under a fixed drain voltage at $V_d = -40$ V. The measurements involved photo-assisted electrical writing (265 nm, 285 mW cm^{-2}; $V_g = 0$, 10, 20, and 30 V) for 10 s or electrical erasing at $V_g = -50$ V for 1 s. The devices were measured at 25 °C and in a nitrogen environment.

doi:10.6342/NTU202503178

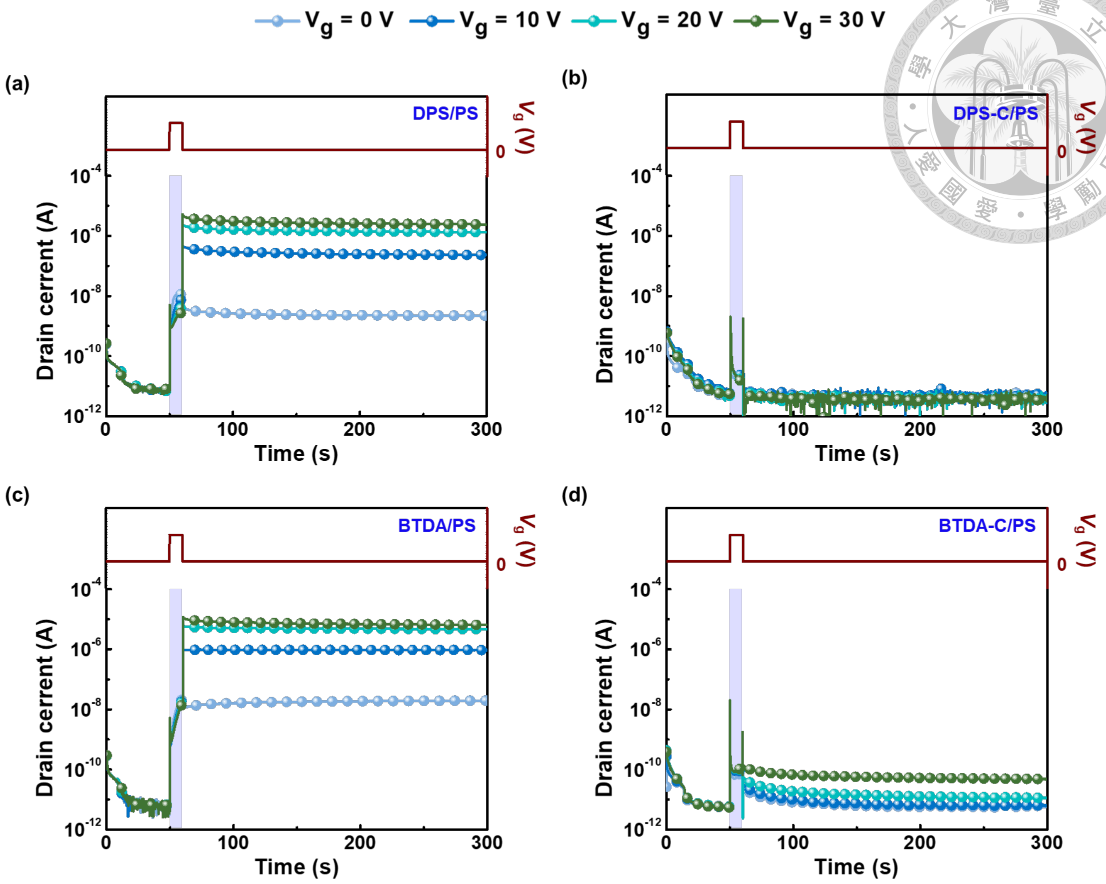

Figure 2.13 Transient characteristics of the transistor memory device were measured with (a) DPS/PS, (b) DPS-C/PS, (c) BTDA/PS, and (d) BTDA-C/PS as the floating gate dielectrics. The measurements were conducted at V_d = −40 V under photo-assisted electrical writing (265 nm, 285 mW cm^{-2}; V_g = 0–30 V) for 10 s.

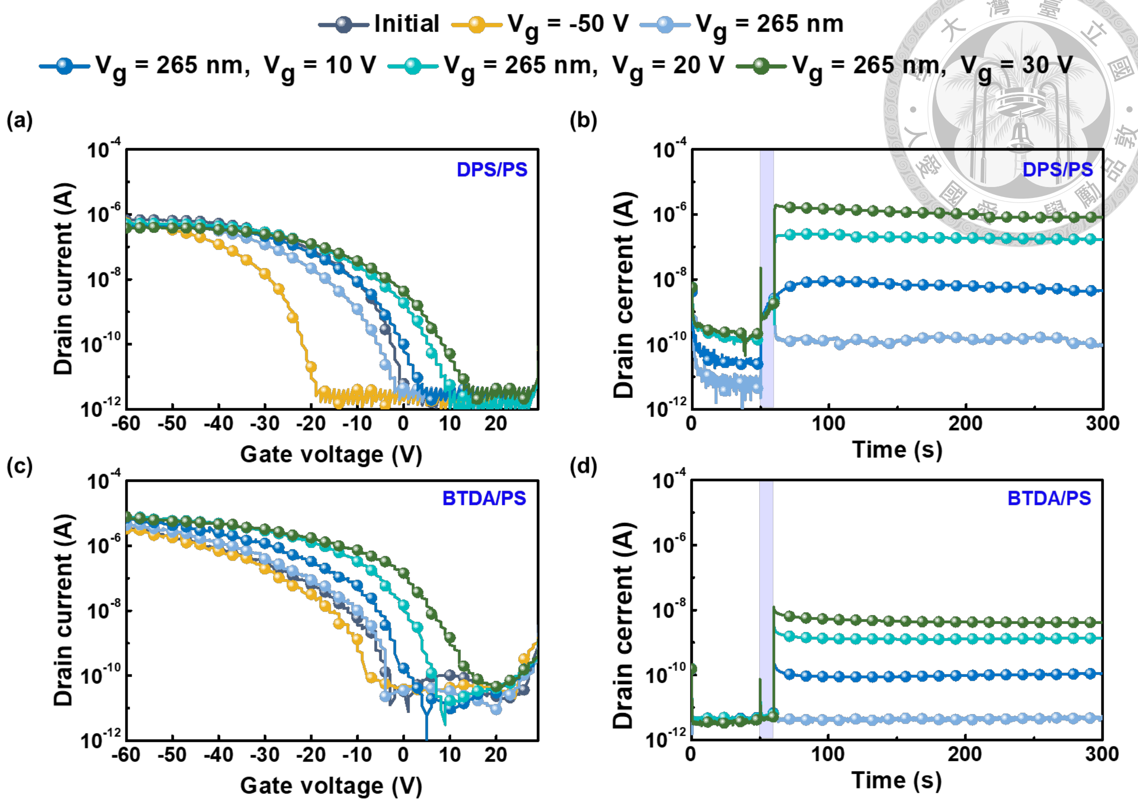

Figure 2.14 The transfer (a, c) and transient (b, d) characteristics of the transistor memory device measured at 70 °C with (a, b) DPS/PS and (c, d) BTDA/PS as the floating gate electrets at $V_d = -40$ V. The measurements involved photo-assisted electrical writing (265 nm, 285 mW cm^{-2}; $V_g = 0$, 10, 20, and 30 V) for 10 s or electrical erasing at $V_g = -50$ V for 1 s.

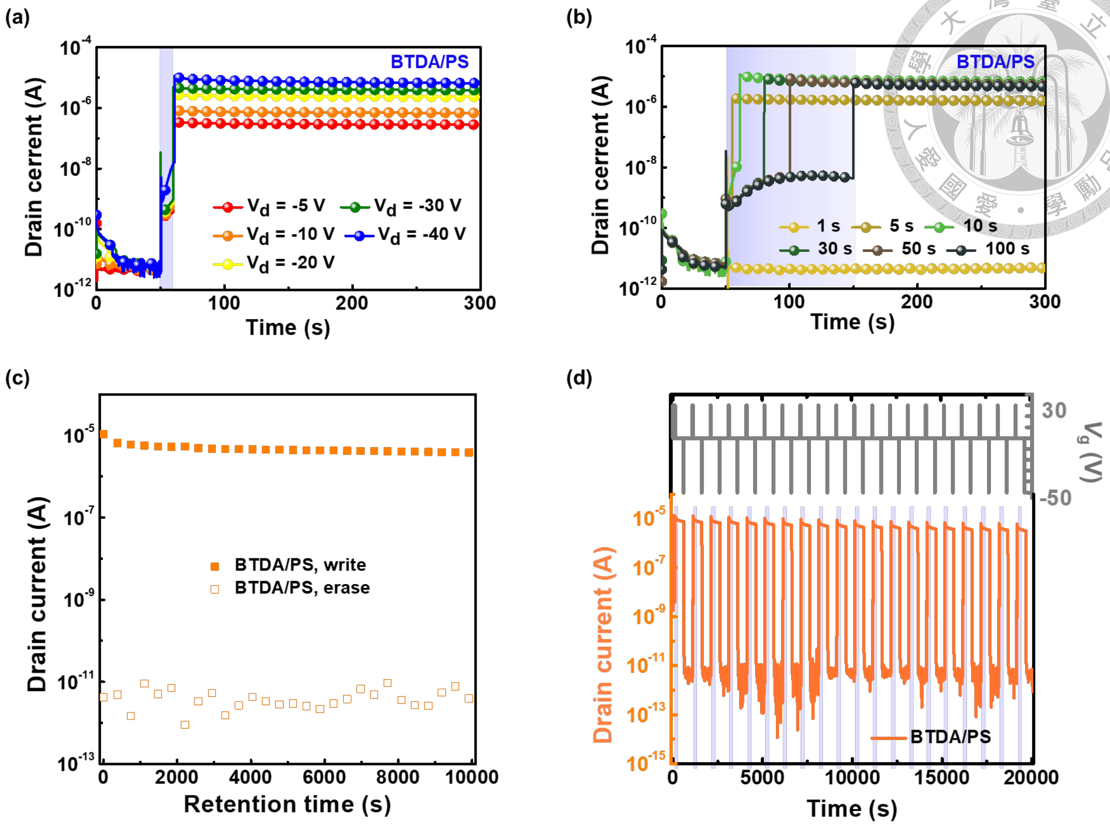

Figure 2.15 Transient characteristics of the transistor memory device were measured with BTDA/PS as the floating gate dielectrics under (a) different V_d from −5 to −40 V (265 nm, 285 mW cm^{-2}; 10 s; V_g = 30 V), and (b) different illumination times from 1 to 100 s (265 nm, 285 mW cm^{-2}; V_d = −40 V; V_g = 30 V). (c) Long-term stability of the transistor memory device BTDA/PS with V_d = −40 V at V_g = 0 V; the ON-state was measured after photo-assisted electrical writing (265 nm, 285 mW cm^{-2}; V_g = 30 V) for 10 s, and the OFF-state was measured after electrical erasing at V_g = −50 V for 1 s. (d) WRER switching test of the transistor memory device with BTDA/PS for 20 cycles measured with V_d = −40 V at V_g = 0 V under photo-assisted electrical writing (265 nm, 285 mW cm^{-2}; V_g = 30 V) for 10 s and electrical erasing at V_g = −50 V for 5 s.

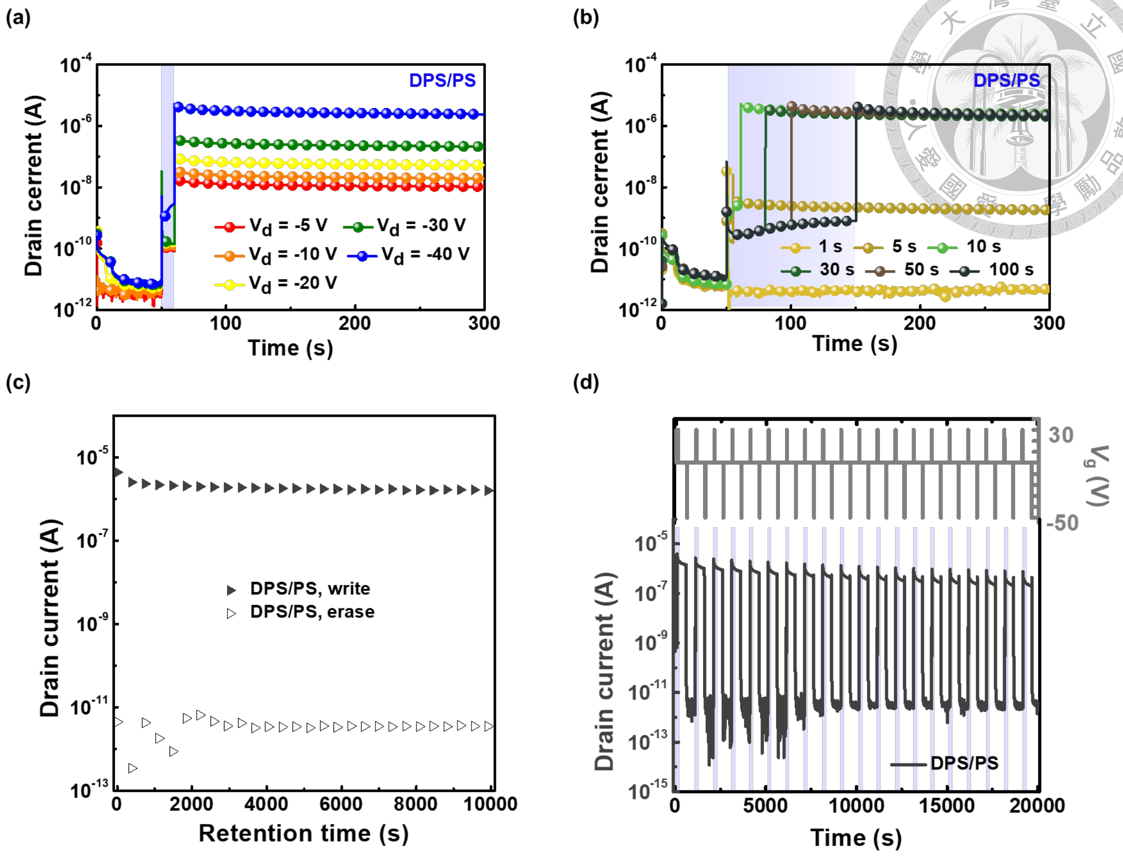

Figure 2.16 Transient characteristics of the transistor memory device were measured with DPS/PS as the floating gate dielectrics under (a) different V_d from −5 to −40 V (265 nm, 285 mW cm^{-2}; 10 s; $V_g = 30$ V), and (b) different illumination times from 1 to 100 s (265 nm, 285 mW cm^{-2}; $V_d = -40$ V; $V_g = 30$ V). (c) Long-term stability of the transistor memory device DPS/PS with $V_d = -40$ V at $V_g = 0$ V; the ON-state was measured after photo-assisted electrical writing (265 nm, 285 mW cm^{-2}; $V_g = 30$ V) for 10 s, and the OFF-state was measured after electrical erasing at $V_g = -50$ V for 1 s. (d) WRER switching test of the transistor memory device with DPS/PS for 20 cycles measured with $V_d = -40$ V at $V_g = 0$ V under photo-assisted electrical writing (265 nm, 285 mW cm^{-2}; $V_g = 30$ V) for 10 s and electrical erasing at $V_g = -50$ V for 1 s.

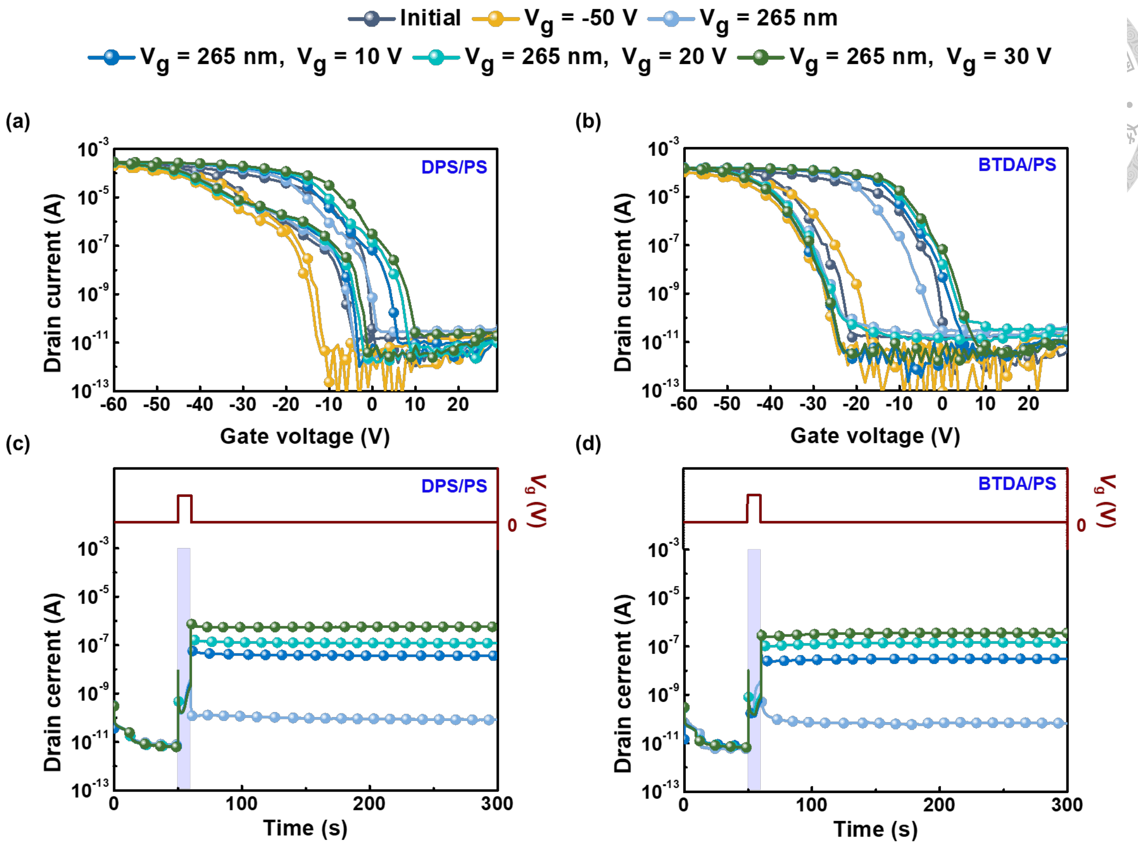

Figure 2.17 The transfer (a, b) and transient (c, d) characteristics of the transistor memory (a, c) DPS/PS and (b, d) BTDA/PS as the floating gate dielectrics at $V_d = -40$ V. The measurements involved photo-assisted electrical writing (265 nm, 285 mW cm^{-2}; $V_g = 0$, 10, 20, and 30 V) for 10 s or electrical erasing at $V_g = -50$ V for 1 s. Additionally, the semiconductor layer was changed from pentacene to DNTT, and the corresponding device characteristics were measured at 25 °C in a nitrogen environment.

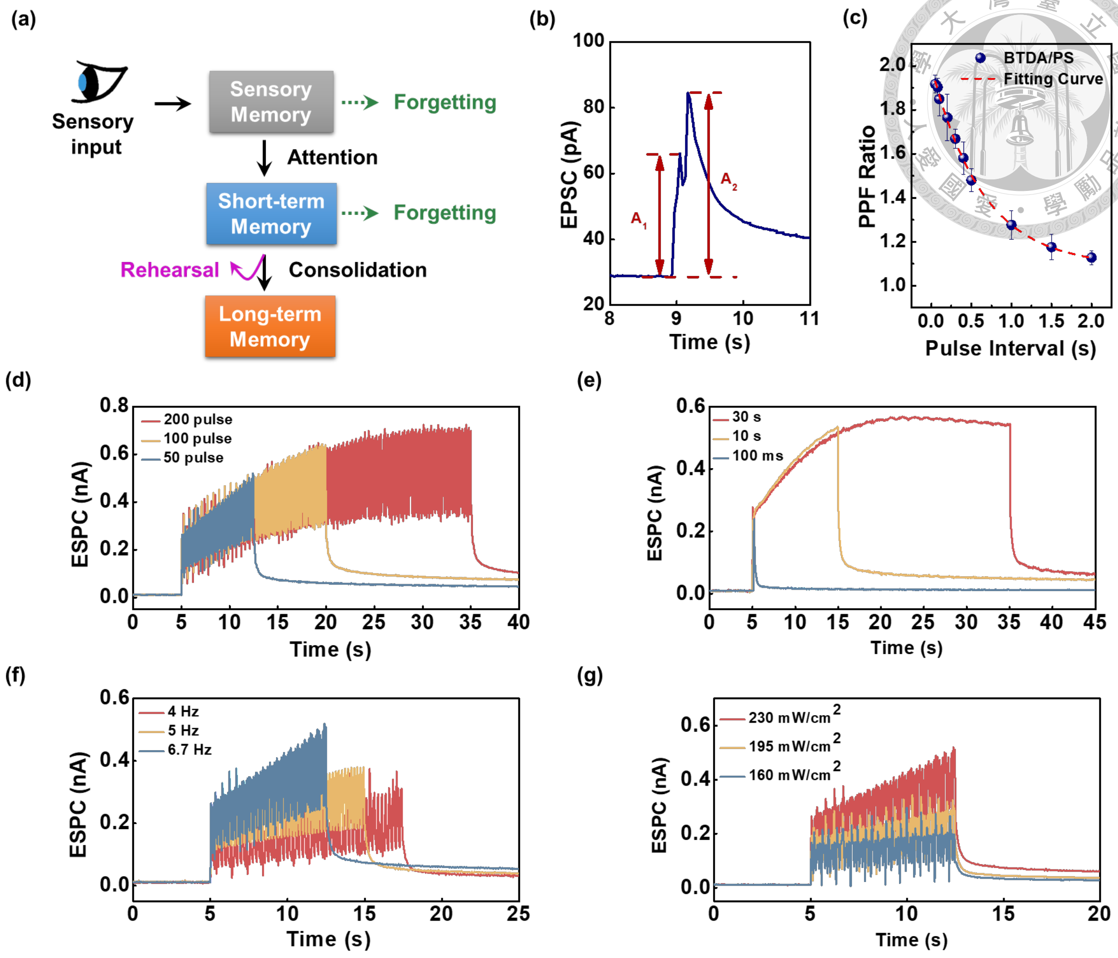

Figure 2.18 (a) Illustration of the staged human memory system. (b) The EPSC of the BTDA/PS photosynaptic transistor emulates PPF behavior under two 265 nm (1.7 mW cm^{-2}) light pulses. (c) The PPF ratio of the BTDA/PS photosynaptic transistor was measured at pulse intervals ranging from 50 ms to 2 s under 265 nm (1.7 mW cm^{-2}) light illumination, with $V_d = -10$ V and $V_g = 0$ V. (d) SNDP, (e) STDP, (f) SRDP, and (g) SIDP of the BTDA/PS-based photosynaptic transistor under 265 nm (1.7 mW cm^{-2}) light illumination, with $V_d = -10$ V and $V_g = 0$ V.

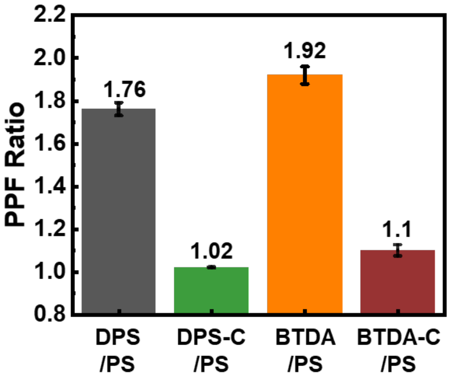

Figure 2.19 The PPF ratio of the DPS/PS, DPS-C/PS, BTDA/PS, and BTDA-C/PS photosynaptic transistors were measured at Δt = 50 ms under 265 nm (1.7 mW cm^{-2}) light illumination, with $V_\mathrm{d} = -10$ V and $V_\mathrm{g} = 0$ V.

doi:10.6342/NTU202503178

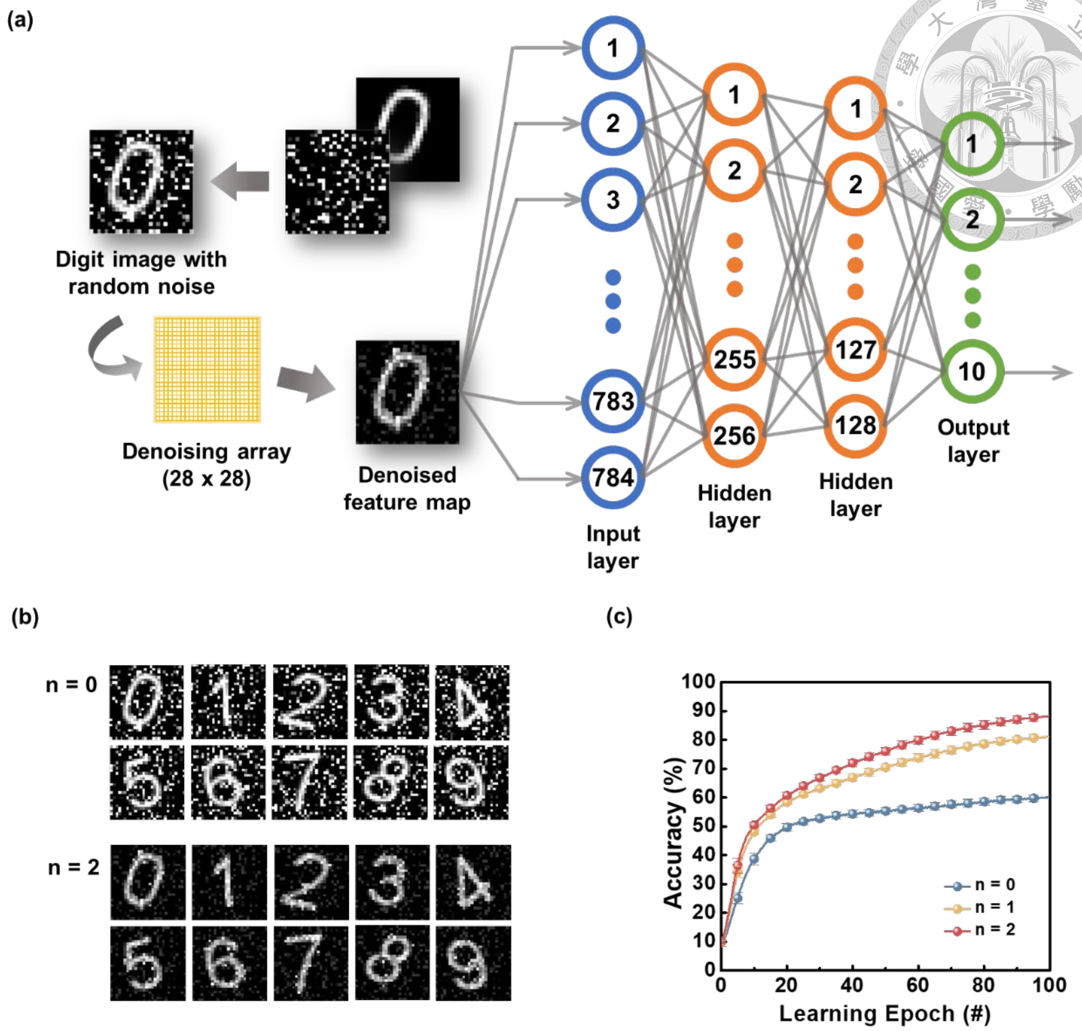

Figure 2.20 (a) Schematic illustration of the simulated ANN for recognizing MNIST handwritten digits. (b) Appearance of the digits before denoising (n = 0) and after two denoising arrays (n = 2). (c) The relationship between recognition accuracy and the number of denoising arrays (n = 0, 1, 2) over 100 learning epochs. The results were conducted based on the synaptic parameters of the BTDA/PS photosynaptic transistors.

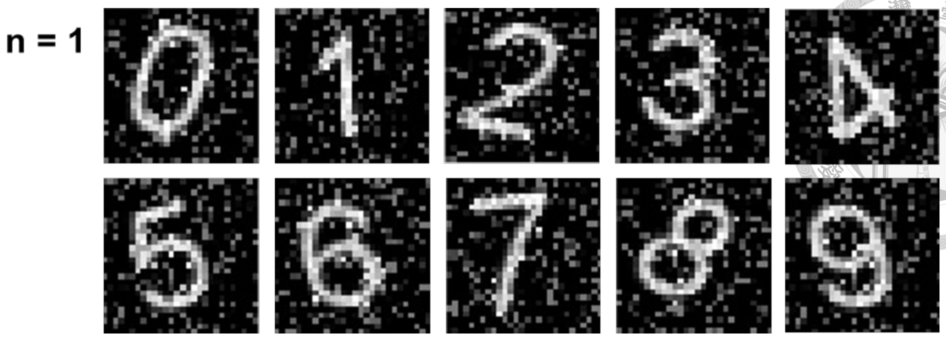

Figure 2.21 Appearance of the MNIST hand-written digits after one denoising array (n = 1).

doi:10.6342/NTU202503178

Chapter 3 Organic Long Persistent Luminescence Materials Based on Host–Guest Systems for Phototransistor Memory

3.1 Introduction

OFETs have emerged as promising components in flexible and low-cost electronics due to their structural tunability and compatibility with solution-based processing.[113] In an OFET, the gate voltage modulates the charge carrier flow in the organic semiconductor channel, enabling key functions such as amplification and switching.[114] These advantages have made OFETs increasingly attractive for next-generation transparent and wearable technologies. By incorporating charge-trapping layers at the gate dielectric interface, OFETs can be extended into nonvolatile memory devices. These OFET memories retain data without a continuous power supply, and benefit from properties such as mechanical flexibility, material diversity, and transparency—attributes difficult to achieve with conventional inorganic memory technologies. [113,115] Strategies such as using metal nanoparticle arrays[115], polymer/ZnO nanocomposites[113], or self-doped polymer wells[114] enhance charge retention and stability, further improving memory performance.

More recently, photomemory based on OFET structures has attracted attention for its ability to utilize light as an additional stimulus to modulate memory states. In such devices, light-responsive layers enable photo-induced charge trapping or release, allowing optical control of memory functions. This approach expands OFET applications to fields like image sensing and neuromorphic computation.[116,117]

doi:10.6342/NTU202503178

Despite the progress in OFET-based photomemory technologies, the choice of light-responsive materials remains a critical bottleneck that limits both performance and integration versatility. Most reported systems rely on conventional photochromic or exciton-based semiconductors, which often suffer from limited retention time, oxygen sensitivity, or complex device architectures. To address these challenges, recent attention has turned toward organic emitters with intrinsically long-lived excited states, particularly OLPL systems. These materials offer unique advantages in photophysical behavior, stability, and compatibility with solution processing—making them highly attractive for light-activated memory applications.

Organic materials with long-lived excited states—including TADF, RTP, and OLPL have attracted significant attention in optoelectronics for their unique exciton dynamics. TADF materials achieve microsecond-scale emission through efficient RISC between singlet and triplet states, whereas RTP materials rely on spin-forbidden radiative transitions from the triplet state, with emission lifetimes extending to seconds.[118] By contrast, OLPL systems exhibit minute to hour-scale luminescence by forming long-lived CS states that slowly recombine to emit light, often in the absence of continuous excitation.[119-121]

OLPL materials have been widely explored for applications in data encryption, optical storage, and time-resolved bioimaging.[120,122] Unlike RTP, which displays a exponential decay, OLPL exhibits power-law decay kinetics, reflecting the gradual recombination of spatially separated charges.[121] Additionally, OLPL does not require heavy-metal-based phosphors and can circumvent oxygen quenching under proper molecular design, making it more suitable for practical and biological applications compared to RTP.[120,123] Historically, LPL has been dominated by inorganic phosphors such as $SrAl_2O_4:Eu^{2+},Dy^{3+}$, which provide glow durations over 10 hours.[124] However,

doi:10.6342/NTU202503178

these materials require high-temperature solid-state synthesis, involve rare earth dopants, and often suffer from processability and toxicity concerns. In contrast, purely organic OLPL materials offer low cost, facile solution processing, mechanical flexibility, and biocompatibility—desirable attributes for next-generation sustainable optoelectronics.[119, 123-125]

Despite their great potential, OLPL materials have not yet been applied in OFET photomemory devices. Considering their light-activated memory potential, long-persistent luminescence, and mechanical flexibility[120, 123], we propose the introduction of host–guest structured OLPL systems into photomemory architectures. This approach is expected to enable the development of metal-free memory devices with long retention time. It offers a novel direction for the design of organic photomemory devices and expands the application potential of OLPL materials in memory functionality.

In this study, an OLPL system with a host–guest structure was developed, employing PMMA as the host matrix, TPB, NPB, and DMFL-NPB as molecules, and C8-NDI as the organic semiconductor channel material. By designing the energy level between host and guest, and optimizing the guest concentration, the system aims to achieve persistent afterglow emission. We systematically investigated how different host–guest combinations influence the luminescent behavior, memory ratio, memory window, and device stability. AFM was used to examine the film morphology, while UV–vis absorption and PL spectroscopy were employed to characterize the optical properties. The results show that the PMMA/DMFL-NPB system containing 5 wt% DMFL-NPB exhibited the most pronounced memory performance.

3.2 Experimental Section

3.2.1 Materials

N,N, N′,N′-tetraphenylbenzidine (TPB, >99.0%) and 2,7-bis(N-(1-naphthyl)aniline)-9,9-dimethylfluorene [DMFLNPB, >98.0%] were purchased from Tokyo Chemical Industry. N, N′-bis(naphthalen-1-yl)-N, N'-bis(phenyl)-benzidine [NPB, >99.5%] and C8-NDI were purchased from Luminescence Technology Corp. Poly(methyl methacrylate) [PMMA, M_w = 350,000 g/mol] and Anisole (anhydrous, 99.7%) were purchased from Sigma-Aldrich.

3.2.2 Fabrication of the Devices

TPB, NPB, DMFLNPB were dissolved in anisole at 5 mg mL^{-1}, respectively, while PMMA was dissolved in anisole at 50 mg mL^{-1}. The solutions were stirred overnight at 60 °C and subsequently filtered using a 0.22 μm polytetrafluoroethylene syringe filter. Subsequently, the guest solutions of TPB, NPB, and DMFLNPB were individually mixed with the PMMA host solution at various weight ratios to prepare formulations containing 2 wt%, 5 wt%, 10 wt%, and 15 wt% of the guest materials (corresponding to 98 wt%, 95 wt%, 90 wt%, and 85 wt% of PMMA, respectively). The resulting mixtures were stirred overnight at 60 °C to ensure thorough homogenization. Highly n-doped silicon wafers with a 100 nm $\mathrm{SiO_2}$ layer were first treated using UV–ozone irradiation for 30 minutes to eliminate surface contaminants and enhance surface wettability. Subsequently, the prepared solutions were spin-coated onto the wafers at 2000 rpm for 60 seconds under a nitrogen environment, forming uniform thin films. A 50 nm-thick C8-NDI semiconductor layer was thermally deposited onto the dielectric layer at a deposition rate of 0.2–0.3 Å s^{-1}. Finally, a 70 nm Au layer was deposited through a patterned shallow mask to define the source and drain electrodes, with channel dimensions of 1000 μm in width (W) and 50 μm in length (L). All thermal evaporation steps were performed in a vacuum chamber maintained at a base pressure of 10^{-7} Torr.

3.2.3 Characterization

The UV–vis absorption spectra were acquired using a Hitachi U-4100 spectrophotometer. The film morphologies were analyzed using Bruker MutiMode 8 atomic force microscope (AFM). The PL and OLPL emission spectra were measured using a Jobin Yvon Fluorolog-3 spectrofluorometer. The electrical performance of the transistor memory devices was characterized using a Keithley 4200-SCS semiconductor parameter analyzer under a nitrogen atmosphere in a glove box. The devices' transfer curves were analyzed by sweeping the V_g from −30 to 60 V with the V_d fixed at 50 V. The electrical erasing process was achieved by applying V_g = 60 V for 2 s. In contrast, a photo writing process was carried out using 365 nm light (18 mW cm^{-2}) and for 10 s, respectively. The devices' retention and WRER were measured using a Keithley 2634B (Keithley Instruments Inc.) inside a nitrogen-filled glovebox.

3.3 Results and Discussions

3.3.1 Device Structure and Morphology Characterization

The device structure used in this study is shown in **Figure 3.1a**. The OLPL electret layer is composed of a host–guest system, where PMMA serves as the host, and TPB, NPB, and DMFL-NPB are used as guest organic luminescent molecules to construct different host–guest combinations. PMMA is an insulating polymer with good film-forming ability and deep energy levels, which provides good dispersion for the guest

doi:10.6342/NTU202503178

molecules in the system. At the same time, the guest molecules TPB, NPB, and DMFL-NPB are aromatic amine derivatives with different degrees of π-conjugation. The nitrogen atoms in their structures help stabilize the radical cations formed after photoexcitation through electronic delocalization. C8-NDI is selected as the semiconductor channel material, and the devices are fabricated in a bottom-gate/top-contact OFET configuration. To further understand the energy level of the materials used in this study, the HOMO/LUMO values were compiled based on previously reported literature[126-130], as illustrated in **Figure 3.1b**. Specifically, the HOMO/LUMO values for C8-NDI, TPB, NPB, DMFL-NPB, and PMMA are (−5.54/−2.48) eV, (−5.52/−2.27) eV, (−5.01/−1.91) eV, (−4.90/−1.90) eV, and (−7.30/−1.80) eV, respectively. As shown in **Figures 3.1c–e**, the UV–vis absorption spectra of NPB, TPB, and DMFL-NPB blended into the PMMA matrix at concentrations of 2, 5, and 15 wt% exhibit absorption bands within the 200 to 400 nm range. Notably, a pronounced absorption peak appears near 365 nm, which was selected as the excitation wavelength for memory operation in this study. It is important to note that, despite variations in concentration, the shape of the absorption peaks remains largely unchanged. Finally, the surface morphology of the host–guest blend films with different guest concentrations was examined using AFM, as shown in **Figure 3.2**. All films exhibited the roughness values around 0.2 nm, indicating a uniform and smooth surface. Such morphology provides a favorable interface for the growth of the C8-NDI semiconductor layer.

3.3.2 Optical Properties

After confirming the film morphology at different guest concentrations, we further investigated the concentration-dependent OLPL emission characteristics. **Figures 3.3a–c** show the fluorescence and OLPL emission spectra of NPB/PMMA, TPB/PMMA, and

DMFL-NPB/PMMA at various concentrations. The results indicate that for guest concentrations of 2 wt%, 5 wt%, and 15 wt%, the fluorescence emission wavelengths of NPB, TPB, and DMFL-NPB are primarily distributed between 400 and 550 nm. Notably, the 2 wt% and 5 wt% samples exhibited strong and distinct OLPL signals, with emission wavelengths ranging from 500 to 650 nm, suggesting that these concentrations effectively promote the formation and stabilization of charge-separated states. However, under the high-concentration condition of 15 wt%, the emission intensity decreased significantly. This confirms that excessive guest content reduces intermolecular spacing, increases the probability of electron–hole recombination, and suppresses delayed luminescence. These findings also suggest the existence of a concentration threshold for achieving OLPL. **Figures 3.3d–f** present the visual OLPL behavior of the same systems at different concentrations. It can be observed that the 2 wt% and 5 wt% samples still exhibit visible afterglow at 0.4 seconds after the light is turned off.

Figures 3.4a–c present the time-resolved OLPL decay profiles of TPB/PMMA, NPB/PMMA, and DMFL-NPB/PMMA films under 365 nm UV excitation. When plotted on logarithmic x- and y-axes, all samples exhibit a clear linear trend, indicating that their emission decay follows a power-law behavior consistent with the Debye–Edwards law. This empirical model describes a class of dispersive recombination kinetics in which photoexcited electrons become trapped within local trap states in an amorphous or rigid dielectric matrix and gradually recombine with spatially separated holes over an extended time scale. The photoluminescence intensity is described by the relation $I\ (\ t\ ) \propto t^{-m}$, where the exponent mm characterizes the carrier recombination rate; a smaller mm value corresponds to slower recombination and a longer afterglow duration.[120, 131] A consistent trend is observed across all three systems: samples with a 5 wt% guest concentration exhibit the highest initial OLPL intensity and the slowest decay rate. This suggests that this concentration facilitates efficient photoinduced charge separation and long-lived charge carrier stabilization, leading to the formation of persistent charge-separated states. In contrast, although the 2 wt% samples still display observable OLPL signals, the lower guest molecule density limits the energy transfer efficiency and the number of charge-separated pairs formed, resulting in weaker emission intensity and reduced afterglow duration. On the other hand, the 15 wt% samples exhibit a faster decay and significantly reduced emission intensity, likely due to shortened intermolecular distances that increase carrier recombination rates. These conditions collectively enhance non-radiative decay pathways and suppress the formation of long-lived charge-separated states, thereby diminishing the OLPL intensity and shortening its persistence.

Overall, these results confirm that guest concentration plays a critical role in determining OLPL performance. A guest concentration of 5 wt% was confirmed to be the optimal condition, as it effectively balances intermolecular spacing and dispersion, enhances exciton management and charge storage efficiency, and thereby enables stable and long-persistent luminescence. This provides a clear strategic guideline for the design of high-performance organic photomemory materials.

3.3.3 Characterization of Phototransistor Memory

After completing the analysis of OLPL optical characteristics, bottom-gate/top-contact OFET memory devices were fabricated using C8-NDI as the semiconductor layer to evaluate their memory behavior, as illustrated in **Figure 3.1a**. **Figure 3.5**, **Figure 3.6**, and **Figure 3.7** show the transfer characteristics of devices using TPB, NPB, and DMFL-NPB as the guest molecules at different concentrations. All devices were measured under a fixed drain voltage (V_d = 50 V), with V_g swept from −30 V to +60 V. For the erase operation, a gate voltage of V_g = 60 V was applied for 2 s, resulting in a negative shift in

doi:10.6342/NTU202503178

the V_{th}, indicating that the device turned to the OFF state. Subsequently, photowriting was performed by irradiating the devices with 365 nm light (18 mW cm^{-2}) for 10 s, during which a positive shift in V_{th} was observed, suggesting successful carrier trapping and storage. The ΔV_{th} is defined as the difference between the erase and write states: $\Delta V_{th} = V_{th,\, erase} - V_{th,\, write}$. As shown in **Figure 3.5**, for the TPB/PMMA system, the values of ($V_{th,\, erase}$, $V_{th,\, write}$, ΔV_{th}) for guest concentrations of 2 wt%, 5 wt%, 10 wt%, and 15 wt% were (5, −7, 12) V, (9, −9, 18) V, (6, −5, 11) V, and (5, −5, 10) V, respectively. In **Figure 3.6**, for NPB/PMMA devices, the corresponding values were (5, −15, 20) V, (9, −18, 27) V, (7, −3, 10) V, and (4, −2, 6) V. In **Figure 3.7**, for the DMFL-NPB/PMMA system, the values were (8, −14, 22) V, (7, −20, 27) V, (3, −7, 10) V, and (6, −4, 10) V. A summary of ΔV_{th} values for all samples is provided in **Table 3.1**. From the results, it is evident that among all three guest systems, the devices with 5 wt% guest concentration consistently exhibited the largest threshold voltage shifts. This indicates a significantly expanded memory window, reflecting superior charge trapping capability and retention stability, which together enhance the overall memory performance of the devices.

After evaluating the typical n-type transfer characteristics, the photoresponse and memory stability of the devices were further investigated using transient current measurements, as shown in **Figures 3.8a–c**. Under photowriting conditions with 365 nm light (18 mW cm^{-2}) for 10 s, all three systems—TPB/PMMA, NPB/PMMA, and DMFL-NPB/PMMA—demonstrated optimal I_{ON}/I_{OFF} performance at a guest concentration of 5 wt%, reaching approximately 1.1×10^5, 1.7×10^5, and 4.9×10^5, respectively. These transient responses are summarized in **Table 3.1**, which clearly shows that for each guest system, the 5 wt% sample consistently achieved both the largest ΔV_{th} and the highest I_{ON}/I_{OFF}, followed by the 2 wt% samples. This behavior can be attributed to enhanced OLPL effects that support longer carrier lifetimes and more stable charge trapping. As a

doi:10.6342/NTU202503178

result, the written state can be maintained even without continuous light exposure or gate bias, demonstrating non-volatile memory characteristics. Among all the samples, the device with 5 wt% DMFL-NPB exhibited the most outstanding performance, showing the highest Vth shift and the greatest I_{ON}/I_{OFF}. This can be further explained by the highly conjugated molecular structure of DMFL-NPB, which effectively stabilizes the photo-generated radical cations and extends hole lifetimes. In addition, the relatively high HOMO level of DMFL-NPB facilitates the formation of deeper hole trapping, suppressing recombination with electrons. This favorable energy level configuration not only stabilizes the spatially separated charge pairs but also prolongs the OLPL lifetime and improves both memory performance and electrical stability. [76, 132-134] These findings indicate that DMFL-NPB is the most promising guest molecule among the systems studied. Furthermore, previous studies have shown that compared to NPB, DMFL-NPB exhibits better π-conjugation extension and higher molecular rigidity due to the incorporation of a rigid fluorene core and multiple aryl side groups.[135] This structural design enhances the stability of radical cations and improves charge injection efficiency, ultimately contributing to higher hole mobility and extended charge storage lifetime.

Since the 5 wt% TPB/PMMA, NPB/PMMA, and DMFL-NPB/PMMA devices exhibited the best memory stability, we further investigated their long-term retention performance. As shown in **Figures 3.9a–c**, after photowriting (365 nm, 18 mW cm^{-2}, 10 s) and electrical erasing (V_g = 60 V, 2 s), all three devices maintained a stable I_{ON}/I_{OFF} approximately 10^3 over a duration of 10,000 seconds, indicating excellent data retention capability. We further examined the influence of erase duration on memory erasure performance for the 5 wt% samples, as shown in **Figures 3.10a–c**. In the TPB and NPB systems, although partial erasure was achieved within 2 to 5 seconds, the minimum OFF current only dropped to around 10^{-11} A, failing to return to the initial pre-written level of

10^{-12} A. Prolonging the erase time did not significantly improve the erasure efficiency, as shown in **Figure 3.10a** and **Figure 3.10b**. For the DMFL-NPB system, **Figure 3.10c** shows that erasure was largely ineffective, indicating more stable and persistent charge trapping. This behavior is closely related to the strong OLPL properties of these systems. Enhanced OLPL is associated with highly stabilized radical states and prolonged charge separation lifetimes, which are beneficial for long-term data retention. However, such stability also hinders the release of trapped charges during the erase process, as the applied electric field cannot easily overcome the deep trap potential and localization energy. As a result, the OFF current cannot fully recover, and the erasure becomes incomplete. This outcome highlights a trade-off between memory stability and electrical rewritability in OLPL-based devices, which must be carefully considered in future memory design. **Figure 3.11a** presents the WRER test results for the 5 wt% TPB/PMMA and NPB/PMMA devices. After 20 write–read–erase–read cycles, both devices maintained stable performance with no significant degradation, demonstrating excellent endurance and operational reliability. However, the minimum OFF current remained around 10^{-11} A, consistent with the limited erasure efficiency observed earlier.

3.3.4 Operating Mechanism of the OLPL Phototransistor Memory Device

As illustrated in **Figure 3.12**, the working mechanism of the OLPL-based phototransistor memory can be understood by correlating the observed optical behavior with the underlying charge trapping dynamics during device operation. The measurements were performed at $V_d = 50$ V, photowriting used 365 nm light (18 mW cm^{-2}) for 10 s, and erasing was done by applying $V_g = 60$ V for 2 s.

Upon photoexcitation, electrons are promoted from the HOMO to the LUMO of the guest molecules. Some of these electrons remain in the guest LUMO, while others transfer to energetically favorable acceptor levels such as the LUMO of C8-NDI or the LUMO of PMMA. Meanwhile, the corresponding holes are trapped in the HOMO levels of the guest molecules. Due to the extremely deep HOMO level of PMMA (−7.30 eV), significantly lower than that of the guest materials (−4.9 to −5.5 eV), it cannot provide sufficient electrons to neutralize the holes. This energy level design stabilizes the charge-separated state, prolongs its lifetime, and results in delayed radiative recombination known as OLPL.

During the electrical erasing operation, a positive gate bias induces an electric field that facilitates the tunneling of electrons from the source electrode into the active layer. These injected electrons recombine with the trapped holes in the guest HOMO, enabling partial neutralization of the previously stored charges. The electrons are selectively captured by positively charged traps located near the interface of the electret layer, which corresponds to the experimentally observed positive shift in threshold voltage. Since only the interfacial holes can be effectively neutralized, the erasing process cannot fully restore the initial state, resulting in partial reversibility of the system.

3.4 Summary

This study successfully developed an OLPL-based memory devices with a host–guest structure, where PMMA was used as the high-energy-barrier host matrix, and three aromatic amine small molecules with different degrees of conjugation (TPB, NPB, and DMFL-NPB) were selected as guest materials. These were integrated with a C8-NDI semiconductor channel in a bottom-gate/top-contact OFET architecture. The effects of guest concentration on both luminescence properties and memory performance were systematically investigated. The results confirmed that 5 wt% was the optimal guest concentration, enabling efficient generation of stable charge-separated states under photoexcitation, along with the strongest OLPL emission and best memory performance. Among the systems studied, the DMFL-NPB/PMMA device showed the most outstanding performance, achieving the highest Ion/Ioff ratio, the largest ΔVth, and retention stability exceeding 10,000 seconds. This superior behavior is attributed to its highly conjugated molecular structure and higher HOMO level, which help stabilize radical cations and facilitate the formation of deep hole traps. However, this high stability also leads to limited charge release during the erase process, indicating that the balance between memory retention and erasability still requires further optimization. Overall, this work demonstrates the promising application of OLPL materials in non-volatile memory devices and provides useful design strategies for host–guest energy level alignment and composition optimization, offering clear guidance for the development of next-generation organic, metal-free memory systems.

3.5 Tables and Figures

Table 3.1 The phototransistor memory characteristics are summarized, highlighting the memory window and memory ratio.

Item	Guest (wt%)	$V_{\text{th, erase}}$ (V)	$V_{\text{th, write}}$ (V)	ΔV_{th} (V)	$I_{\text{ON}}/I_{\text{OFF}}$
TPB/PMMA	2	5	-7	12	1.8×10^4
	5	9	-9	18	1.1×10^5
	10	6	-5	11	5.0×10^3
	15	5	-5	10	2.0×10^3
NPB/PMMA	2	5	-15	20	1.5×10^5
	5	9	-18	27	1.7×10^5
	10	7	-3	10	4.8×10^4
	15	4	-2	6	1.4×10^4
DMFL-NPB/PMMA	2	8	-14	22	4.9×10^4
	5	7	-20	27	4.9×10^5
	10	3	-7	10	4.1×10^4
	15	6	-4	10	1.3×10^4

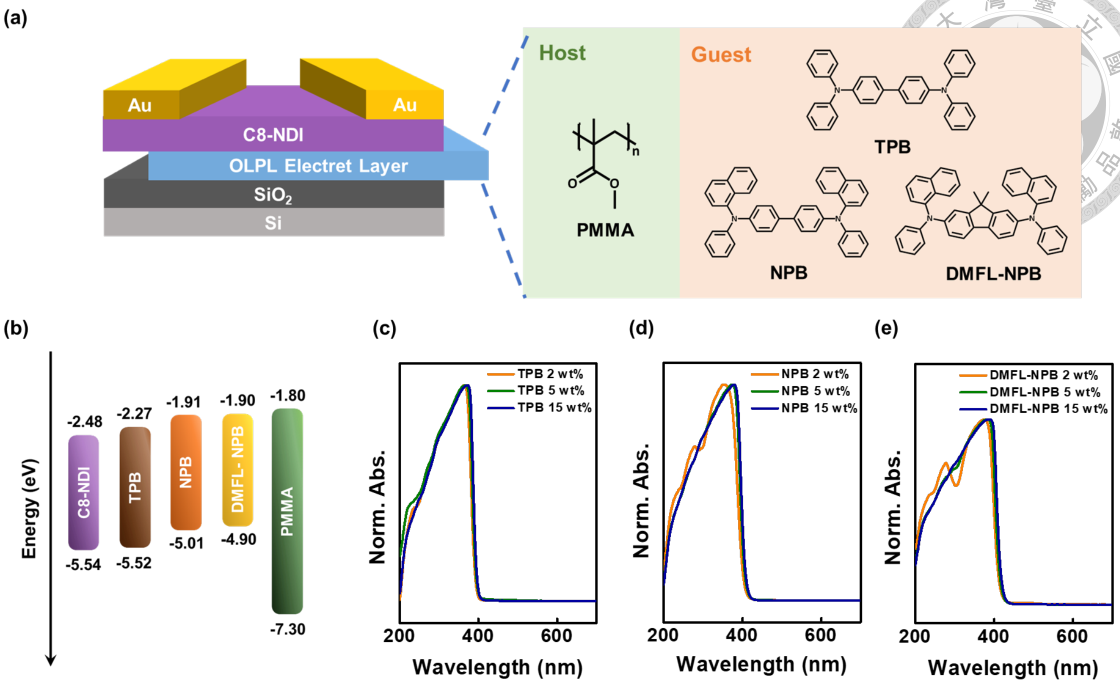

Figure 3.1 (a) Schematic illustration of the phototransistor memory structure and the molecular structures of the host–guest systems. (b) Energy levels diagram of the materials investigated in this study. UV-vis absorption spectra of (c) TPB/PMMA, (d) NPB/PMMA, and (e) DMFL-NPB/PMMA films.

doi:10.6342/NTU202503178

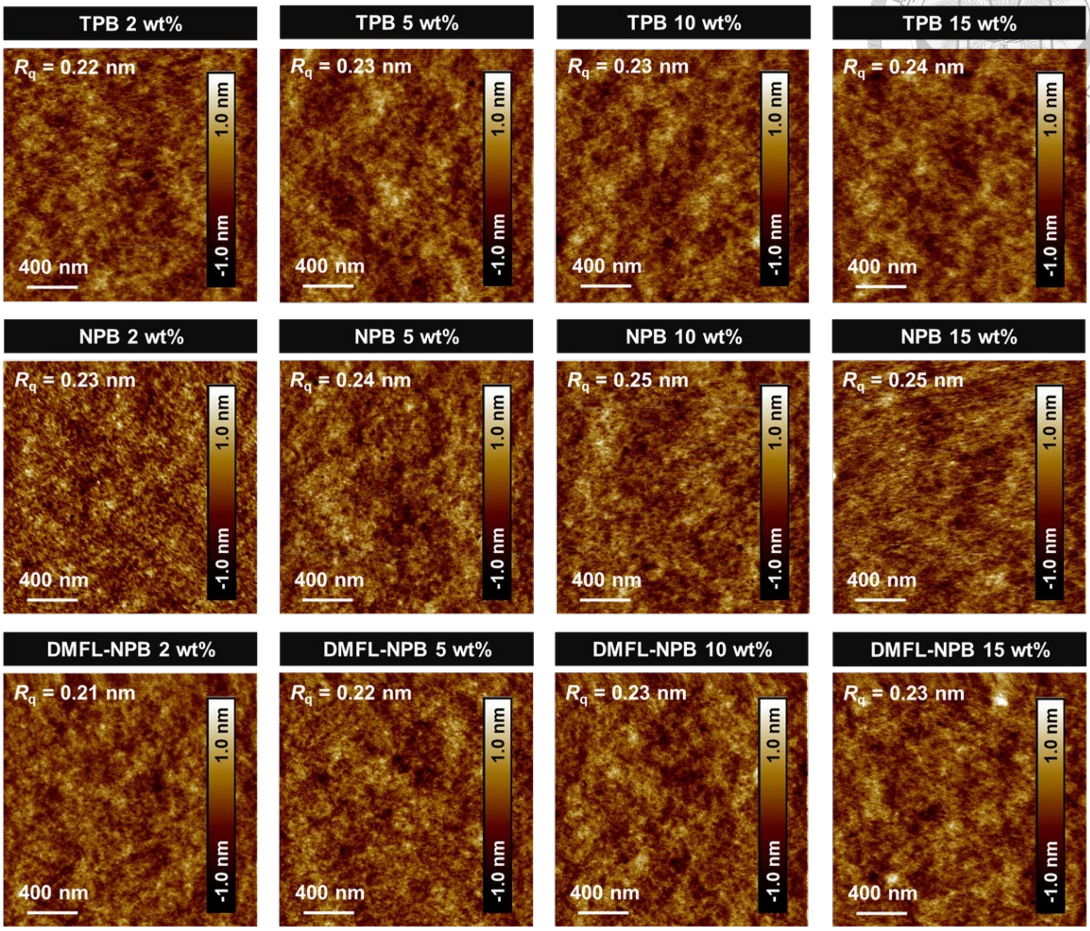

Figure 3.2 AFM height profiles of TPB/PMMA, NPB/PMMA, and DMFL-NPB/PMMA thin films.

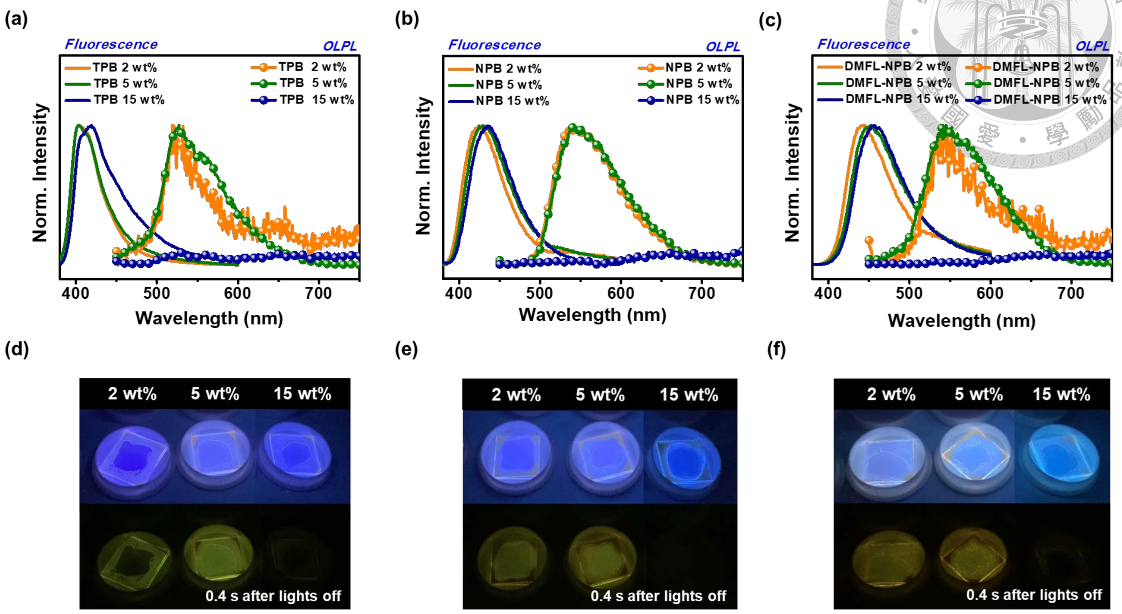

Figure 3.3 (a–c) The fluorescence and OLPL emission spectra of (a) NPB/PMMA, (b) TPB/PMMA, and (c) DMFL-NPB/PMMA films at different guest concentrations, excited under 365 nm. (d–f) Photographs of (d) NPB/PMMA, (e) TPB/PMMA, and (f) DMFL-NPB/PMMA films under 365 nm (top) and 0.4 s after the light was turned off (bottom), illustrating the concentration-dependent OLPL behavior.

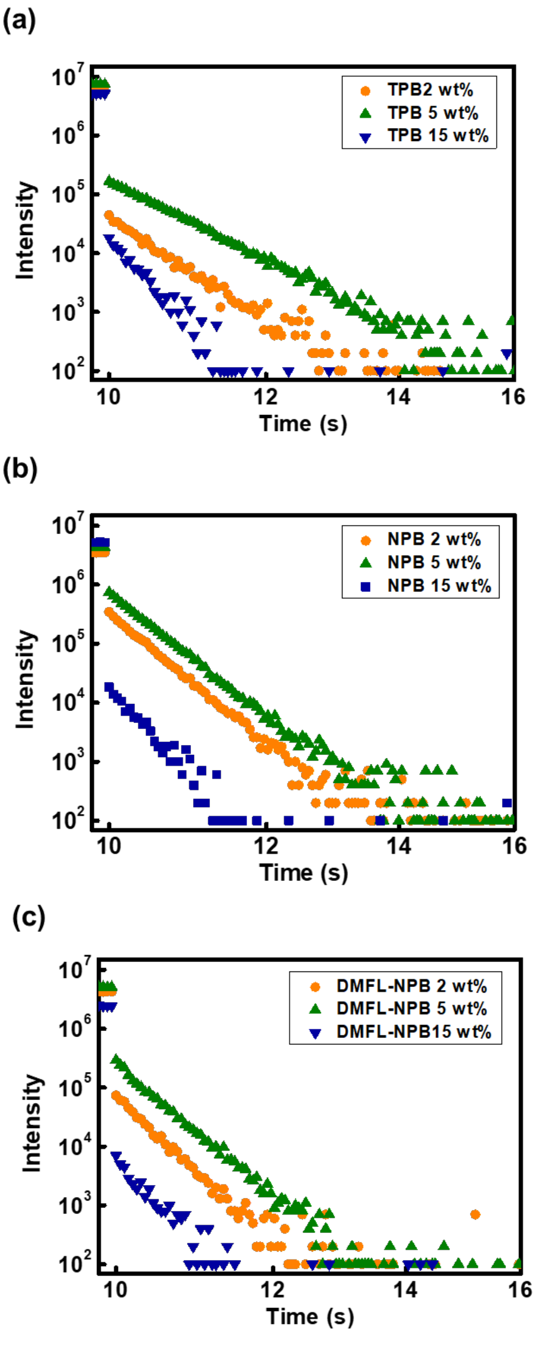

Figure 3.4 OLPL decay profiles of (a) TPB/PMMA, (b) NPB/PMMA, and (c) DMFL-NPB/PMMA films with different guest concentrations after 365 nm excitation. The decay profiles exhibit a power-law behavior that fits the Debye–Edwards law.

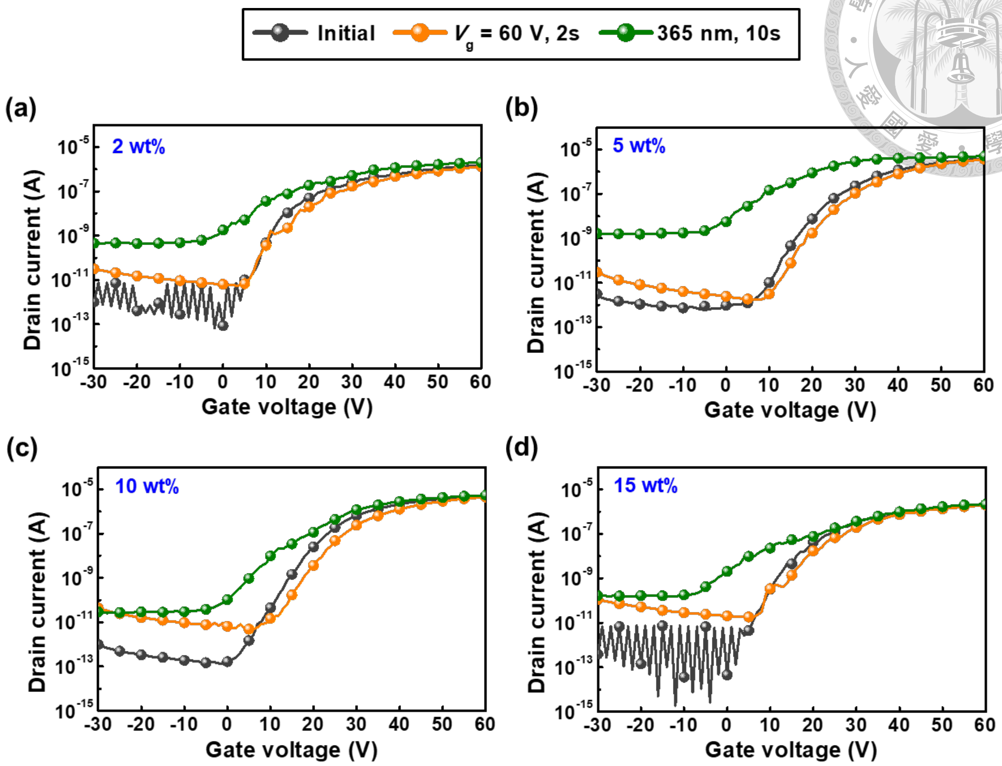

Figure 3.5 Transfer characteristics of the TPB/PMMA phototransistor memory device with varying guest concentrations—(a) 2 wt%, (b) 5 wt%, (c) 10 wt%, and (d) 15 wt%—measured at V_d = 50 V. The measurements were performed after photowriting using 365 nm light (18 mW cm^{-2}) for 10 s and electrical erasing at V_g = 60 V for 2 s.

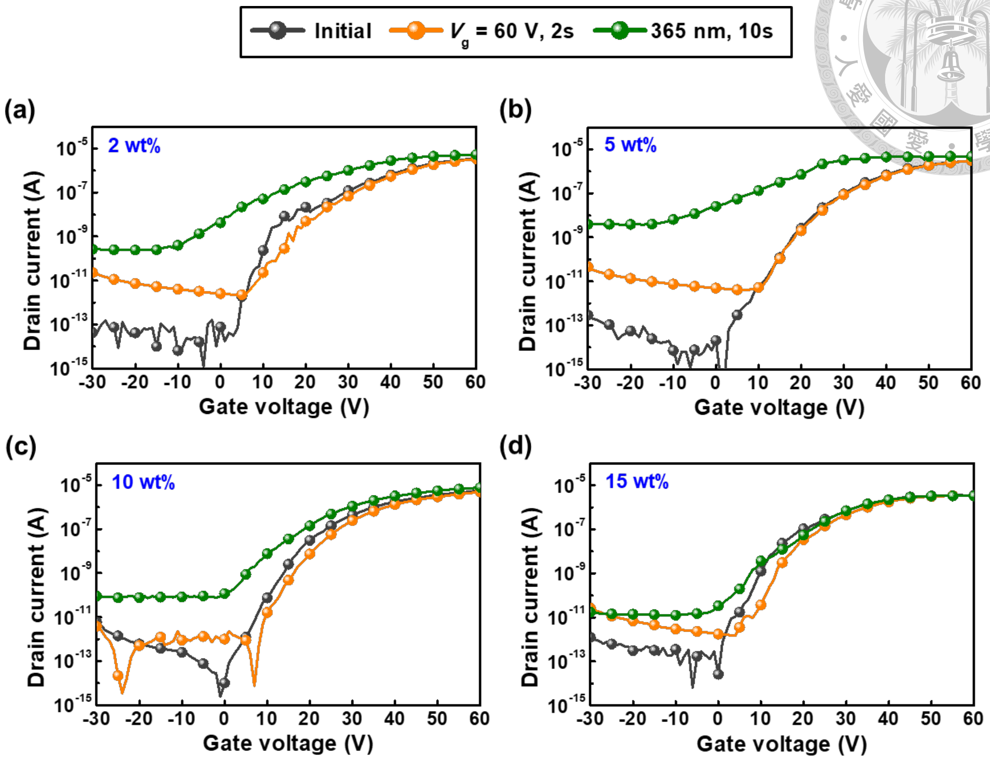

Figure 3.6 Transfer characteristics of the NPB/PMMA phototransistor memory device with varying guest concentrations—(a) 2 wt%, (b) 5 wt%, (c) 10 wt%, and (d) 15 wt%—measured at V_d = 50 V. The measurements were performed after photowriting using 365 nm light (18 mW cm^{-2}) for 10 s and electrical erasing at V_g = 60 V for 2 s.

doi:10.6342/NTU202503178

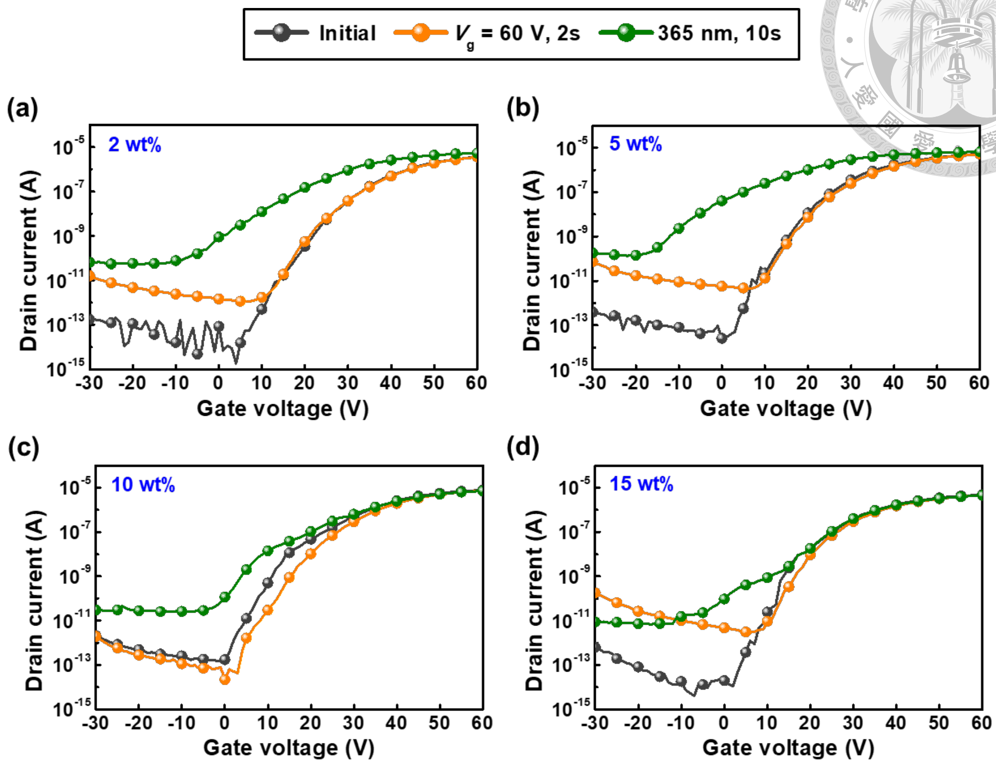

Figure 3.7 Transfer characteristics of the DMFL-NPB/PMMA phototransistor memory device with varying guest concentrations—(a) 2 wt%, (b) 5 wt%, (c) 10 wt%, and (d) 15 wt%—measured at V_d = 50 V. The measurements were performed after photowriting using 365 nm light (18 mW cm^{-2}) for 10 s and electrical erasing at V_g = 60 V for 2 s.

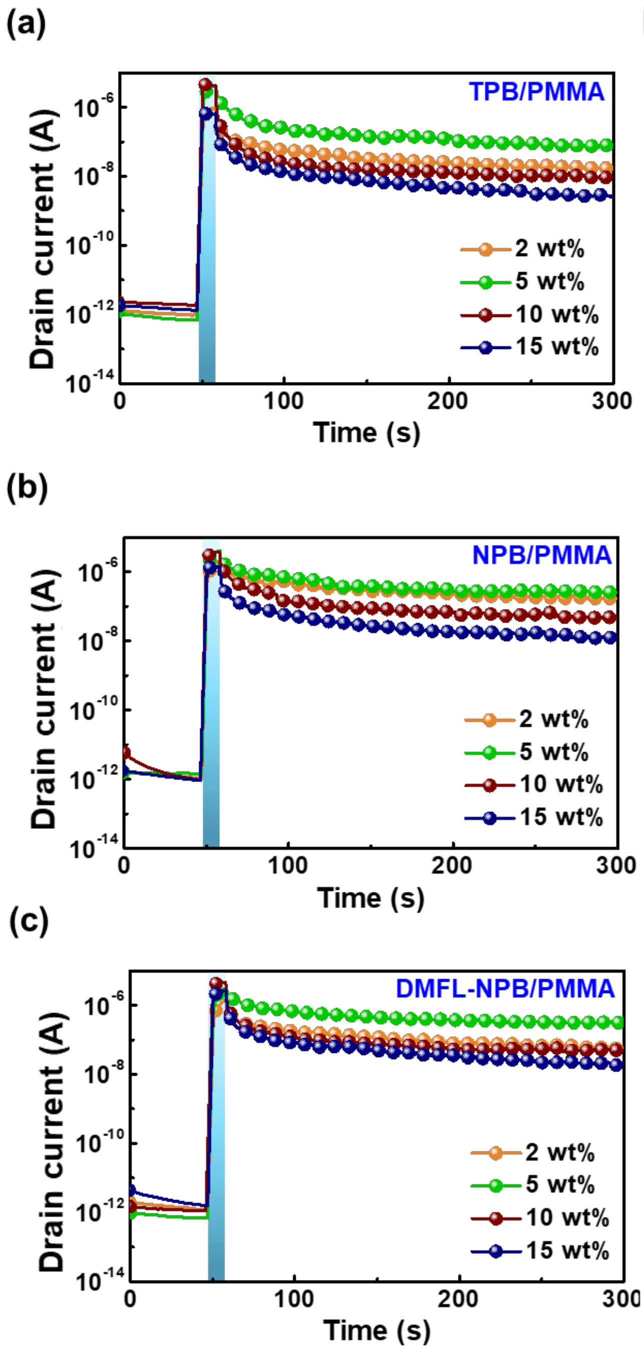

Figure 3.8 Transient characteristics of the phototransistor memory devices with varying guest concentrations were measured using (a) TPB/PMMA, (b) NPB/PMMA, and (c) DMFL-NPB/PMMA as the electret layer. The measurements were conducted at $V_d = 50$ V under photowriting with 365 nm light (18 mW cm^{-2}) for 10 s.

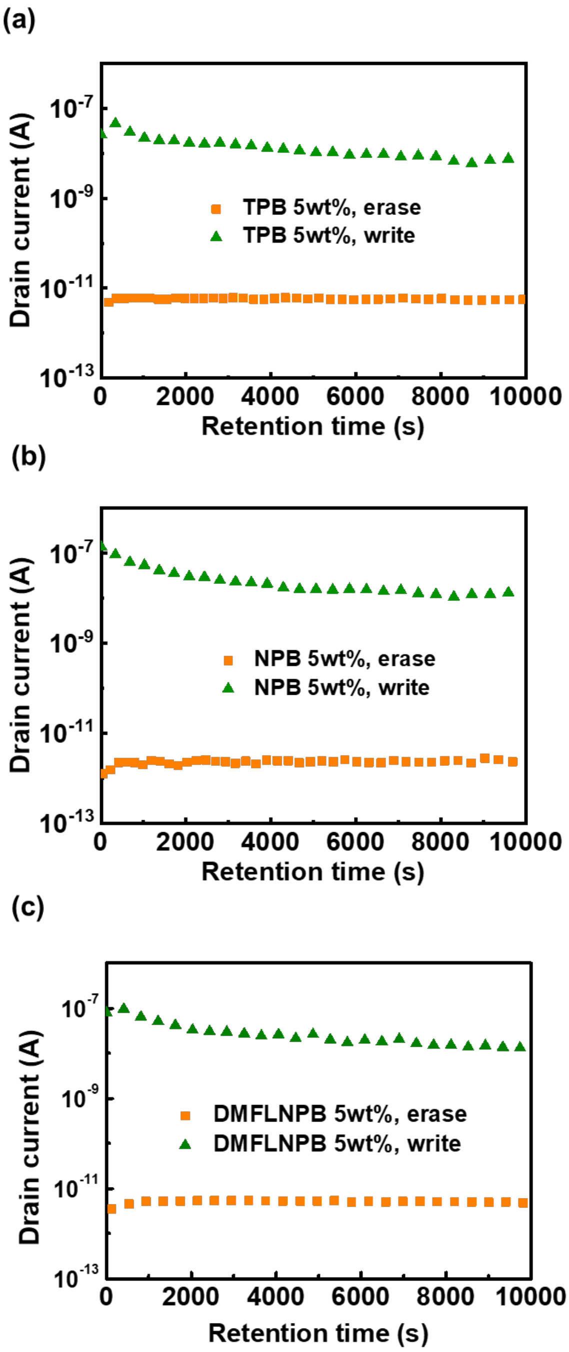

Figure 3.9 Long-term stability of the phototransistor memory devices with 5 wt% guest concentration was evaluated using (a) TPB/PMMA, (b) NPB/PMMA, and (c) DMFL-NPB/PMMA as the electret layers at V_d = 50 V. The ON-state was measured after photowriting with 365 nm light (18 mW cm^{-2}) for 10 s, and the OFF-state was measured after electrical erasing at V_g = 60 V for 2 s.

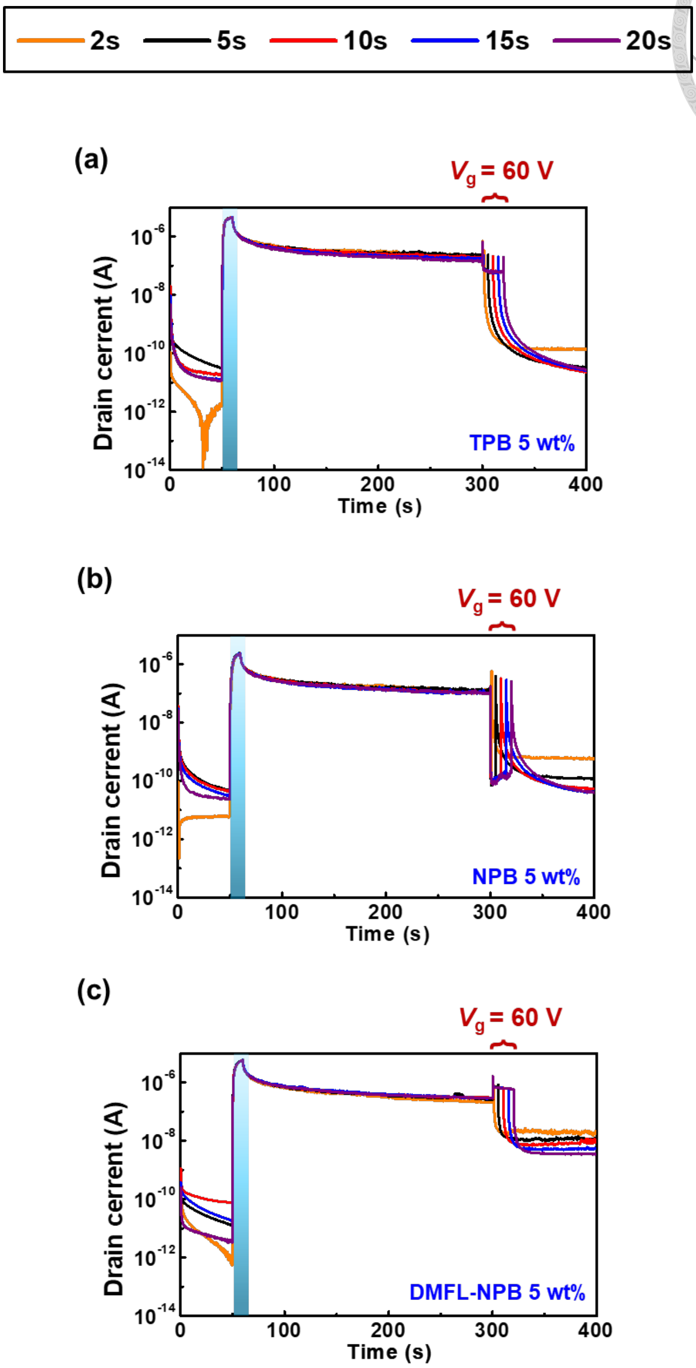

Figure 3.10 Transient response of phototransistor memory devices with 5 wt% guest loading, using (a) TPB, (b) NPB, and (c) DMFL-NPB as the electret layer, showing the effect of varying erase durations at V_g = 60 V after photowriting with 365 nm light (18 mW cm^{-2}, 10 s).

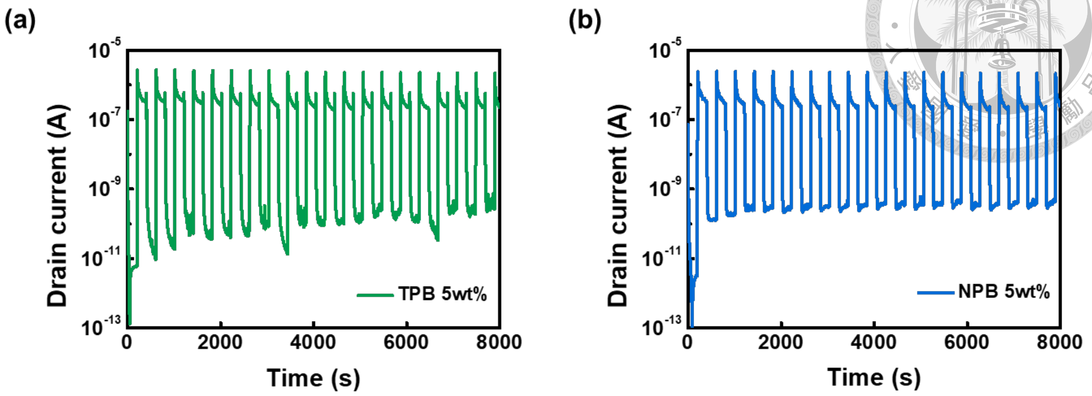

Figure 3.11 WRER switching test of the phototransistor memory devices with 5 wt% guest concentration using (a) TPB/PMMA and (b) NPB/PMMA as the electret layers, measured over 20 cycles at V_d = 50 V. Photowriting was performed with 365 nm (18 mW cm^{-2}) for 10 s and electrical erasing at V_g = 60 V for 5 s.

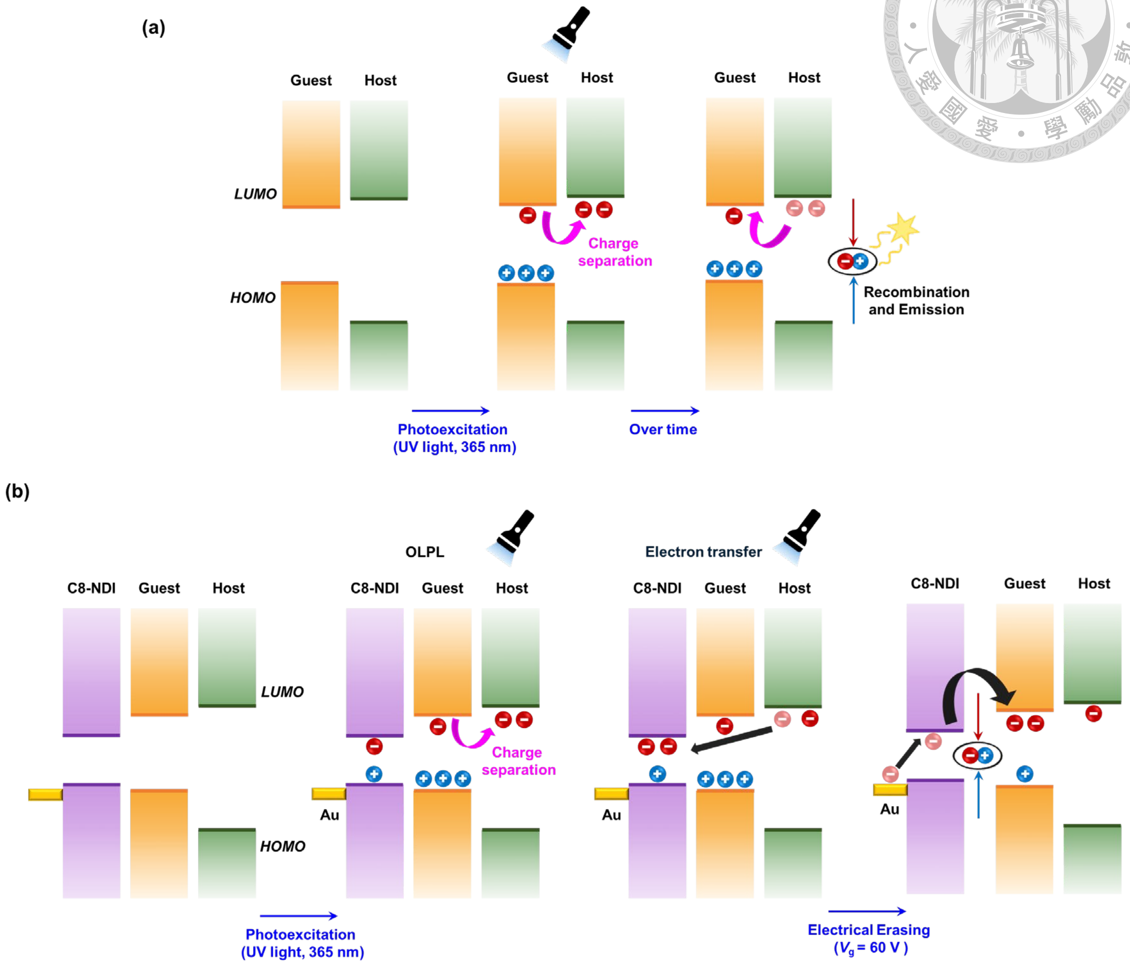

Figure 3.12 Schematic illustration of (a) the mechanism of OLPL in host–guest systems, and (b) the operating mechanism of OLPL-based host–guest systems in phototransistor memory devices.

Chapter 4 Conclusion and Future work

This study presents the first systematic integration of purely organic RTP and OLPL materials as floating-gate layers in OFETs, aiming to explore their potential in non-volatile photomemory and synaptic devices. In the RTP system, DPS and BTDA exhibited long-lived triplet excitons, with the BTDA/PS-based device achieving a high memory on/off ratio of up to 10^6 under photo-assisted electrical writing and maintaining stable retention over 10,000 seconds. The rigid molecular structures and strong intermolecular interactions of these materials effectively suppressed nonradiative decay, making them ideal candidates for floating-gate light-emitting dielectrics. In addition, the device demonstrated excellent photo-synaptic behavior, showing both short-term and long-term plasticity under repeated light pulses. It was further applied in neural network simulations, where it exhibited strong recognition performance, confirming its feasibility in artificial intelligence systems.

On the other hand, the OLPL system used PMMA as a host matrix, mixed with various aromatic amine molecules including TPB, NPB, and DMFL-NPB. By adjusting the energy level alignment and optimizing the guest concentration, especially at 5 wt%, the devices showed strong OLPL emission and stable charge storage behavior. Among these, DMFL-NPB, due to its extended conjugated structure and relatively high HOMO level, helped generate stable radical cations and deep hole trapping, leading to the best memory window and charge retention. However, the strong charge stability also reduced the erasing efficiency, showing a trade-off between long-term storage and reversibility that should be addressed in future designs.

Overall, this work offers a novel approach by combining delayed-excited-state materials with organic memory devices, and proves that purely organic RTP and OLPL materials can effectively enhance the performance and lifetime of OFET-based memory. Moreover, the long-lived excitons and stable charge-separated states generated by these materials enable data retention without continuous power supply, which meets the needs of modern memory technologies. The use of metal-free, solution-processable organic molecules also ensures environmental friendliness, material simplicity, and lower manufacturing costs. Furthermore, the demonstrated photo-synaptic behavior and tunable memory properties suggest strong potential for applications in neural networks and intelligent sensing systems. This research lays a solid foundation for the future development of flexible electronics, sensory memory devices, and multilevel memory systems, contributing to the advancement of next-generation sustainable and intelligent memory technologies.

References

[1] C. a. Di, F. Zhang, D. Zhu, *Advanced Materials* **2013**, 25, 313.

[2] A. Salehi, X. Fu, D. H. Shin, F. So, *Advanced Functional Materials* **2019**, 29, 1808803.

[3] G. Hong, X. Gan, C. Leonhardt, Z. Zhang, J. Seibert, J. M. Busch, S. Bräse, *Advanced Materials* **2021**, 33, 2005630.

[4] L. Duan, A. Uddin, *Advanced Science* **2020**, 7, 1903259.

[5] Z. A. Lamport, H. F. Haneef, S. Anand, M. Waldrip, O. D. Jurchescu, *Journal of Applied Physics* **2018**, 124.

[6] Y. Yu, Q. Ma, H. Ling, W. Li, R. Ju, L. Bian, N. Shi, Y. Qian, M. Yi, L. Xie, *Advanced Functional Materials* **2019**, 29, 1904602.

[7] J. Tao, W. Sun, L. Lu, *Biosensors and Bioelectronics* **2022**, 216, 114667.

[8] J. Zaumseil, H. Sirringhaus, *Chemical Reviews* **2007**, 107, 1296.

[9] C. R. Newman, C. D. Frisbie, D. A. da Silva Filho, J.-L. Brédas, P. C. Ewbank, K. R. Mann, *Chemistry of Materials* **2004**, 16, 4436.

[10] S. Riera-Galindo, F. Leonardi, R. Pfattner, M. Mas-Torrent, *Advanced Materials Technologies* **2019**, 4, 1900104.

[11] P. W. Blom, *Advanced Materials Technologies* **2020**, 5, 2000144.

[12] Y.-H. Chou, H.-C. Chang, C.-L. Liu, W.-C. Chen, *Polymer Chemistry* **2015**, 6, 341.

[13] C.-C. Shih, W.-Y. Lee, W.-C. Chen, *Materials Horizons* **2016**, 3, 294.

[14] L. Shao, Y. Zhao, Y. Liu, *Advanced Functional Materials* **2021**, 31, 2101951.

[15] E. Restuccia, A. Ghobadi, S. Guha, *Advanced Materials Interfaces* **2025**, 2401035.

[16] C. Zheng, Y. Liao, S. T. Han, Y. Zhou, *Advanced Electronic Materials* **2020**, 6,

2000641.

[17] S. Dai, Y. Zhao, Y. Wang, J. Zhang, L. Fang, S. Jin, Y. Shao, J. Huang, *Advanced Functional Materials* **2019**, 29, 1903700.

[18] Y. Guo, G. Yu, Y. Liu, *Advanced Materials* **2010**, 22, 4427.

[19] S. Lee, S. Kim, H. Yoo, *Polymers* **2021**, 13, 3774.

[20] K. J. Baeg, Y. Y. Noh, J. Ghim, B. Lim, D. Y. Kim, *Advanced Functional Materials* **2008**, 18, 3678.

[21] Z. Zhu, Y. Guo, Y. Liu, *Materials Chemistry Frontiers* **2020**, 4, 2845.

[22] R. C. Naber, K. Asadi, P. W. Blom, D. M. De Leeuw, B. De Boer, *Advanced Materials* **2010**, 22, 933.

[23] A. I. Khan, A. Keshavarzi, S. Datta, *Nature Electronics* **2020**, 3, 588.

[24] M. Xu, X. Zhang, S. Li, T. Xu, W. Xie, W. Wang, *Journal of Materials Chemistry C* **2019**, 7, 13477.

[25] Y.-C. Lin, W.-C. Yang, Y.-C. Chiang, W.-C. Chen, *Small Science* **2022**, 2, 2100109.

[26] Y. J. Jeong, D.-J. Yun, S. H. Noh, C. E. Park, J. Jang, *ACS nano* **2018**, 12, 7701.

[27] J. Chang, C. H. Shin, Y. J. Park, S. J. Kang, H. J. Jeong, K. J. Kim, C. J. Hawker, T. P. Russell, D. Y. Ryu, C. Park, *Organic Electronics* **2009**, 10, 849.

[28] H. Uoyama, K. Goushi, K. Shizu, H. Nomura, C. Adachi, *Nature* **2012**, 492, 234.

[29] Y. Chen, H. Wang, Y. Yao, Y. Wang, C. Ma, P. Samorì, *Advanced Materials* **2021**, 33, 2103369.

[30] X. Wang, X. Zhang, Z. Cheng, J. Zhao, Y. Liu, X. Wu, H. Tian, T. G. Chulkova, S. A. Miltsov, A. V. Yakimansky, *The Journal of Physical Chemistry C* **2024**, 128, 10742.

[31] T. J. Penfold, E. Gindensperger, C. Daniel, C. M. Marian, *Chemical Reviews* **2018**, 118, 6975.

[32] Y. Pan, J. Li, X. Wang, Y. Sun, J. Li, B. Wang, K. Zhang, *Advanced Functional Materials* **2022**, 32, 2110207.

[33] X.-K. Chen, D. Kim, J.-L. Brédas, *Accounts of Chemical Research* **2018**, 51, 2215.

[34] Z. Qin, H. Gao, H. Dong, W. Hu, *Advanced Materials* **2021**, 33, 2007149.

[35] J. Li, H. Gong, J. Zhang, S. Zhou, L. Tao, L. Jiang, Q. Guo, *Frontiers in Chemistry* **2021**, 9, 693813.

[36] L. G. Franca, D. G. Bossanyi, J. Clark, P. L. Dos Santos, *ACS Applied Optical Materials* **2024**, 2, 2476.

[37] B. Li, M. Liu, L. Sang, Z. Li, X. Wan, Y. Zhang, *Advanced Optical Materials* **2023**, 11, 2202610.

[38] C. Gao, W. W. Wong, Z. Qin, S. C. Lo, E. B. Namdas, H. Dong, W. Hu, *Advanced Materials* **2021**, 33, 2100704.

[39] S. E. Seo, H.-S. Choe, H. Cho, H.-i. Kim, J.-H. Kim, O. S. Kwon, *Journal of Materials Chemistry C* **2022**, 10, 4483.

[40] B. Zhang, K. D. Richards, B. E. Jones, A. R. Collins, R. Sanders, S. R. Needham, P. Qian, A. Mahadevegowda, C. Ducati, S. W. Botchway, *Angewandte Chemie International Edition* **2023**, 62, e202308602.

[41] Z.-Y. Huang, Y.-H. Weng, Y.-C. Lin, W.-C. Chen, *ACS Applied Optical Materials* **2025**, 3, 861.

[42] Z.-Y. Huang, Y.-H. Weng, Y.-F. Yang, B.-H. Lin, Y.-C. Lin, W.-C. Chen, *ACS Photonics* **2023**, 10, 4509.

[43] M. Uji, T. J. Zähringer, C. Kerzig, N. Yanai, *Angewandte Chemie International Edition* **2023**, 62, e202301506.

[44] H. Yang, S. Guo, B. Jin, Y. Luo, X. Li, *Polymer Chemistry* **2022**, 13, 4887.

[45] P. Bi, T. Zhang, Y. Guo, J. Wang, X. W. Chua, Z. Chen, W. P. Goh, C. Jiang, E. E.

Chia, J. Hou, *Nature Communications* **2024**, 15, 5719.

[46] N. Gan, H. Shi, Z. An, W. Huang, *Advanced Functional Materials* **2018**, 28, 1802657.

[47] Y. Zhang, L. Gao, X. Zheng, Z. Wang, C. Yang, H. Tang, L. Qu, Y. Li, Y. Zhao, *Nature Communications* **2021**, 12, 2297.

[48] J. Ren, Y. Wang, Y. Tian, Z. Liu, X. Xiao, J. Yang, M. Fang, Z. Li, *Angewandte Chemie* **2021**, 133, 12443.

[49] L. Ma, Q. Xu, S. Sun, B. Ding, Z. Huang, X. Ma, H. Tian, *Angewandte Chemie International Edition* **2022**, 61, e202115748.

[50] J. Xu, S. Tanabe, *Journal of Luminescence* **2019**, 205, 581.

[51] Z. Lin, J. Ye, S. Shinohara, Y. Tanaka, R. Yoshioka, C.-Y. Chan, Y.-T. Lee, X. Tang, K. Mitrofanov, K. Wang, *Nature Communications* **2025**, 16, 2686.

[52] Z. Lin, R. Kabe, K. Wang, C. Adachi, *Nature Communications* **2020**, 11, 191.

[53] Z. Lin, R. Kabe, N. Nishimura, K. Jinnai, C. Adachi, *Advanced Materials* **2018**, 30, 1803713.

[54] J. Zhang, W. Wang, Y. Bian, Y. Wang, X. Lu, Z. Guo, C. Sun, Z. Li, X. Zhang, J. Yuan, *Advanced Materials* **2024**, 36, 2404769.

[55] D. Liu, Y. Song, H. Wang, T. Wang, Z. Zhou, Z. Liu, W. Lu, T. Wang, *Journal of Materials Chemistry C* **2024**, 12, 10942.

[56] S. Zhang, Y. Zhao, Q. Chen, Y. Wang, J. Jiang, Y. Wang, Y. Fu, Q. Liu, Q. Wang, D. He, *Microelectron. Eng.* **2023**, 274, 111982.

[57] G.-T. Go, Y. Lee, D.-G. Seo, M. Pei, W. Lee, H. Yang, T.-W. Lee, *Adv. Intell. Syst.* **2020**, 2, 2000012.

[58] S. Furber, *J. Neural Eng.* **2016**, 13, 051001.

[59] R. Yang, H. M. Huang, X. Guo, *Adv. Electron. Mater.* **2019**, 5, 1900287.

doi:10.6342/NTU202503178

[60] F. Sun, Q. Lu, S. Feng, T. Zhang, *ACS Nano* **2021**, 15, 3875.

[61] K. Chen, H. Hu, I. Song, H. B. Gobeze, W.-J. Lee, A. Abtahi, K. S. Schanze, J. Mei, *Nat. Photonics* **2023**, 17, 629.

[62] H. Han, Z. Xu, K. Guo, Y. Ni, M. Ma, H. Yu, H. Wei, J. Gong, S. Zhang, W. Xu, *Adv. Intell. Syst.* **2020**, 2, 1900176.

[63] Y. Yang, Y. He, S. Nie, Y. Shi, Q. Wan, *IEEE Electron Device Lett.* **2018**, 39, 897.

[64] C. Wan, P. Cai, M. Wang, Y. Qian, W. Huang, X. Chen, *Adv. Mater.* **2020**, 32, 1902434.

[65] F. Zhang, C. Li, Z. Li, L. Dong, J. Zhao, *Microsyst. Nanoeng.* **2023**, 9, 16.

[66] R. Khan, N. U. Rehman, S. Iqbal, S. Abdullaev, H. M. Aldosari, *ACS Appl. Electron. Mater.* **2023**, 6, 73.

[67] B. H. Mun, B. K. You, S. R. Yang, H. G. Yoo, J. M. Kim, W. I. Park, Y. Yin, M. Byun, Y. S. Jung, K. J. Lee, *ACS nano* **2015**, 9, 4120.

[68] H. Han, H. Yu, H. Wei, J. Gong, W. Xu, *Small* **2019**, 15, 1900695.

[69] J. Pyo, J.-H. Bae, S. Kim, S. Cho, *Materials* **2023**, 16, 1249.

[70] S. Dai *et al.*, *Adv. Funct. Mater.* **2019**, 29, 1903700.

[71] C.-H. Cheng, F.-S. Yeh, and A. Chin, *Adv. Mater.* **2011**, 23, 902.

[72] S. Dugu, S. P. Pavunny, T. B. Limbu, B. R. Weiner, G. Morell, R. S. Katiyar, *APL Mater.* **2018**, 6.

[73] H. Yoo, I. S. Lee, S. Jung, S. M. Rho, B. H. Kang, H. J. Kim, *Adv. Mater.* **2021**, 33, 2006091.

[74] S. T. Han, Y. Zhou, V. Roy, *Adv. Mater.* **2013**, 25, 5425.

[75] Y. Yang, J. Ouyang, L. Ma, R. H. Tseng, C. W. Chu, *Adv. Funct. Mater.***2006**, 16, 1001.

[76] F. H. Abd Nasir, K. L. Woon, *Synth. Met.* **2024**, 117661.

[77] J. Ouyang, *J. Mater. Chem. C* **2015**, 3, 7243.

[78] L. Yuan, S. Liu, W. Chen, F. Fan, G. Liu, *Adv. Electron. Mater.* **2021**, 7, 2100432.

[79] Q. Ling, Y. Song, S. J. Ding, C. Zhu, D. S. Chan, D.-L. Kwong, E.-T. Kang, K.-G. Neoh, **2005**.

[80] F. Laquai, Y. S. Park, J. J. Kim, and T. Basché, *Macromol. Rapid Commun.* **2009**, 30, 1203.

[81] T. Förster, *New Compr. Biochem.* **1967**, 22, 61.

[82] S. Xu, R. Chen, C. Zheng, and W. Huang, *Adv. Mater.* **2016**, 28, 9920.

[83] X. Yang, G. I. Waterhouse, S. Lu, and J. Yu, *Chem. Soc. Rev.* **2023**, *52*, 8005.

[84] S. Sem, S. Jenatsch, K. Stavrou, A. Danos, A. P. Monkman, and B. Ruhstaller, *J. Mater. Chem. C* **2022**, 10, 4878.

[85] K K. Zhang, T. Zhou, Q. Cao, F. Ge, H. Xu, J. Chu, J. Wang, M. Pei, X. Ban, T. Zhang, *Org. Electron.* **2023**, 112, 106687.

[86] Q. Zhou, C. Yang, and Y. Zhao, *Chem.* **2023**, 9, 2446.

[87] Y. Liu, G. Zhan, Z.-W. Liu, Z.-Q. Bian, and C.-H. Huang, *Chin. Chem. Lett.* **2016**, 27, 1231.

[88] T. Zhang, X. Ma, H. Wu, L. Zhu, Y. Zhao, and H. Tian, *Angew. Chem. Int. Ed.* **2020**, 59, 11206.

[89] J. Yang, M. Fang, and Z. Li, *Acc. Mater. Res.* **2021**, 2, 644.

[90] B. Ding, X. Ma, and H. Tian, *Acc. Mater. Res.* **2023**, 4, 827.

[91] Y. Zhang, Q. Sun, L. Yue, Y. Wang, S. Cui, H. Zhang, S. Xue, W. Yang, *Adv. Sci.* **2022**, 9, 2103402.

[92] J. C. Chen, Y. D. Lu, and J. Y. Chen, *Adv. Sci.* **2023**, 10, 2301028.

[93] L. D. Wiyanto, B. J. You, L. J. Chiang, D. L. Yang, J. Y. Chen, *Adv. Funct. Mater.* **2022**, 32, 2206040.

doi:10.6342/NTU202503178

[94] H. Jin, T. Wang, Z.-R. Gong, C. Long, Y. Dai, *Nanoscale* **2018**, 10, 19310.

[95] Z. Yin, Q. Sun, L. Chen, M. Du, Y. Y. Huang, Q. Peng, G. Zhang, D. Zhang, *Adv. Opt. Mater.* **2023**, 11, 2202224.

[96] A.-C. Chang, Y.-C. Lin, H.-C. Yen, W.-C. Yang, Y.-F. Yang, and W.-C. Chen, *ACS Appl. Electron. Mater.* **2022**, 4, 1266.

[97] Z. Mao, Z. Yang, Z. Fan, E. Ubba, W. Li, Y. Li, J. Zhao, Z. Yang, M. P. Aldred, Z. Chi, *Chem. Sci.* **2019**, 10, 179.

[98] A. B. Pun, A. Asadpoordarvish, E. Kumarasamy, M. J. Tayebjee, D. Niesner, D. R. McCamey, S. N. Sanders, L. M. Campos, M. Y. Sfeir, *Nat. Chem.* **2019**, 11, 821.

[99] S. N. Sanders, E. Kumarasamy, K. J. Fallon, M. Y. Sfeir, and L. M. Campos, *Chem. Sci.* **2020**, 11, 1079.

[100] O. V. Mikhnenko, P. W. Blom, and T.-Q. Nguyen, *Energy Environ. Sci.* **2015**, 8, 1867.

[101] R. Malatong, T. Loythaworn, S. Arunlimsawat, P. Chasing, P. Therdkatanyuphong, W. Waengdongbung, T. Sudyoadsuk, V. Promarak, *J. Mater. Chem. C* **2024**, 12, 16025.

[102] J. Bai, P. Chen, Y. Lei, Y. Zhang, Q. Zhang, Z. Xiong, F. Li, *Org. Electron.* **2014**, 15, 169.

[103] L.-Y. Su, H.-Y. Lin, H.-K. Lin, S.-L. Wang, L.-H. Peng, J. Huang, *IEEE Electron Device Lett.* **2011**, 32, 1245.

[104] C.-W. Tseng, D.-C. Huang, Y.-T. Tao, *ACS Appl. Mater. Interfaces* **2015**, 7, 9767.

[105] C. C. Hung, Y. C. Chiu, H. C. Wu, C. Lu, C. Bouilhac, I. Otsuka, S. Halila, R. Borsali, S. H. Tung, W. C. Chen, *Adv. Funct. Mater.* **2017**, 27, 1606161.

[106] Y. Ran, W. Lu, X. Wang, Z. Qin, X. Qin, G. Lu, Z. Hu, Y. Zhu, L. Bu, G. Lu,

Mater. Horiz. **2023**, 10, 4438.

[107] L. Jiang, C. Xu, X. Wu, X. Zhao, L. Zhang, G. Zhang, X. Wang, L. Qiu, *ACS Appl. Mater. Interfaces* **2022**, 14, 11718.

[108] C. Han, X. Han, J. Han, M. He, S. Peng, C. Zhang, X. Liu, J. Gou, J. Wang, *Adv. Funct. Mater.* **2022**, 32, 2113053.

[109] S. Zhang, R. Chen, D. Kong, Y. Chen, W. Liu, D. Jiang, W. Zhao, C. Chang, Y. Yang, Y. Liu, D. Wei. *Nature Nanotechnol.* **2024**, *19*, 1323.

[110] S. Bai, K. Haase, M. Hambsch, S. C. B. Mannsfeld. *Adv. Electron. Mater.* **2024**, 11, 2400307.

[111] R. S. Yadav, P. Gupta, A. Holla, K. I. Ali Khan, P. K. Muduli, and D. Bhowmik, *ACS Appl. Electron. Mater.* **2023**, 5, 484.

[112] Y. Choi, J.-H. Kim, C. Qian, J. Kang, M. C. Hersam, J.-H. Park, J. H. Cho, *ACS Appl. Mater. Interfaces* **2019**, 12, 4707.

[113] C.-C. Shih, W.-Y. Lee, Y.-C. Chiu, H.-W. Hsu, H.-C. Chang, C.-L. Liu, W.-C. Chen, *Scientific Reports* **2016**, 6, 20129.

[114] S. Nam, Y.-G. Ko, S. Gyu Hahm, S. Park, J. Seo, H. Lee, H. Kim, M. Ree, Y. Kim, *NPG Asia Materials* **2013**, 5, e33.

[115] I. Cho, B. J. Kim, S. W. Ryu, J. H. Cho, J. Cho, *Nanotechnology* **2014**, 25, 505604.

[116] S. P. Prakoso, M.-N. Chen, Y.-C. Chiu, *Journal of Materials Chemistry C* **2022**, 10, 13462.

[117] J. Zhuang, W.-S. Lo, L. Zhou, Q.-J. Sun, C.-F. Chan, Y. Zhou, S.-T. Han, Y. Yan, W.-T. Wong, K.-L. Wong, *Scientific Reports* **2015**, 5, 14998.

[118] S. Xu, L.-L. Wu, X. Wang, H.-Y. Hu, *TrAC Trends in Analytical Chemistry* **2023**, 169, 117356.

[119] J. Yang, Z. Chen, M. Fang, Z. Li, *Smart Molecules* **2024**, 2, e20240034.

doi:10.6342/NTU202503178

[120] K. Jinnai, R. Kabe, Z. Lin, C. Adachi, *Nature Materials* **2022**, 21, 338.

[121] Y. Zhao, B. Ding, Z. Huang, X. Ma, *Chemical Science* **2022**, 13, 8412.

[122] G. Huang, Z. Deng, J. Pang, J. Li, S. Ni, J. A. Li, C. Zhou, H. Li, B. Xu, L. Dang, *Advanced Optical Materials* **2021**, 9, 2101337.

[123] L. Xiao, Z. Wang, C. Zhang, X. Xie, H. Ma, Q. Peng, Z. An, X. Wang, Z. Shuai, M. Xiao, *The Journal of Physical Chemistry Letters* **2020**, 11, 3582.

[124] S. Wu, Z. Pan, R. Chen, X. Liu, *Springer*, **2017**.

[125] Y. Li, M. Gecevicius, J. Qiu, *Chemical Society Reviews* **2016**, 45, 2090.

[126] Y. S. Lin, Y. C. Lin, W. C. Yang, G. S. Li, E. Ercan, C. C. Hung, W. C. Chien, W. C. Chen, *Advanced Electronic Materials* **2022**, 8, 2100798.

[127] Y. Song, S. Lv, X. Liu, X. Li, S. Wang, H. Wei, D. Li, Y. Xiao, Q. Meng, *Chemical Communications* **2014**, 50, 15239.

[128] W. Qiu, X. Cai, M. Li, Z. Chen, L. Wang, W. Xie, K. Liu, M. Liu, S.-J. Su, *The Journal of Physical Chemistry Letters* **2021**, 12, 4600.

[129] Y. Nishikitani, H. Takeuchi, H. Nishide, S. Uchida, S. Yazaki, S. Nishimura, *Journal of Applied Physics* **2015**, 118.

[130] W. Li, Z. Li, C. Si, M. Y. Wong, K. Jinnai, A. K. Gupta, R. Kabe, C. Adachi, W. Huang, E. Zysman-Colman, *Advanced Materials* **2020**, 32, 2003911.

[131] P. Alam, N. L. Leung, J. Liu, T. S. Cheung, X. Zhang, Z. He, R. T. Kwok, J. W. Lam, H. H. Sung, I. D. Williams, *Advanced Materials* **2020**, 32, 2001026.

[132] B. Tang, J. Zhao, J.-F. Xu, X. Zhang, *Chemical Science* **2020**, 11, 1192.

[133] H. Gao, G. Wang, T. Wang, Z. Ye, Q. Yan, Q. Chong, C. Y. Chan, B. Wang, K. Zhang, *Advanced Science* **2025**, 12, 2416853.

[134] C. Zheng, Y. Liao, S. T. Han, Y. Zhou, *Advanced Electronic Materials* **2020**, 6, 2000641.

[135] J. Yang, Y. Li, S. Duhm, J. Tang, S. Kera, N. Ueno, *Advanced Materials Interfaces* **2014**, 1, 1300128.